Phonon Effects on Ultrafast Dynamics in Photosynthesis and Optoelectronic Materials: Forays with Two-Dimensional Electronic Spectroscopy

by

Daniele Michele Monahan

A dissertation submitted in partial satisfaction

of the requirements for the degree of

Doctor of Philosophy

in

Chemistry

in the

Graduate Division

of the

University of California, Berkeley

Committee in charge:

Professor Graham R. Fleming, Chair
Professor Phillip L. Geissler
Professor Ali Javey

Fall 2017

Phonon Effects on Ultrafast Dynamics in Photosynthesis and Optoelectronic Materials: Forays with Two-Dimensional Electronic Spectroscopy

Abstract

Phonon Effects on Ultrafast Dynamics in Photosynthesis and Optoelectronic Materials: Forays with Two-Dimensional Electronic Spectroscopy

by

Daniele Michele Monahan

Doctor of Philosophy in Chemistry

University of California, Berkeley

Professor Graham R. Fleming, Chair

This dissertation describes the use of two-dimensional electronic spectroscopy to explore the impact of phonons and vibrations on the ultrafast electronic processes in photosynthetic light harvesting, hot carrier persistence in perovskite photovoltaics, and efficient photoluminescence in a 2D semiconductor. Each example represents a case where a unified picture of nuclear and electronic response is needed to understand the mechanism. In the introduction, we summarize the electron-phonon interactions that affect optoelectronic processes, and we introduce ultrafast two-dimensional spectroscopy (2D-ES) and the physical information accessed through this experiment. Coherences and wavepackets are introduced, and a time-dependent picture of quantum mechanics is emphasized throughout. The concept of an open system and the impact of environmental fluctuations on dynamics and measurements is equally important. In Chapter 2 these are explored using numerically exact open-system simulations to show the effect of vibrations in the chlorophyll molecule on coherent energy transfer in a photosynthetic complex and on our ability to measure it using two-dimensional spectroscopy. We show that even weak coupling to vibrations generates vibrational wavepacket signatures, and that resonances between vibrations and electronic energy gaps produce vibronic energy transfer effects that are sensitive to environmental fluctuations.

The experimental portion follows with a discussion of strategies for applying two-dimensional spectroscopy techniques to samples with weak signals and/or strong scatterinng. These include signal processing methods and a new scheme we have devised for rapid scatter subtraction using a cheap, easily programmed microprocessor. We also discuss extensive modifications that allow fluorescence-detected 2D-ES. In Chapter 4, 2D-ES is used to study methylammonium lead iodide perovskite, a hybrid organic-inorganic photovoltaic. We find a vibrational wavepacket that is a good candidate mode for a phonon bottleneck effect thought to slow hot carrier cooling in this material. Chapter 5 presents preliminary results from a 2D-ES study of another semiconductor, single-layer MoS_2. We identify from the temperature-dependent 2D lineshape an optical phonon mode principally responsible for early-time charge carrier scattering. We also observe a coupling between two opposite-spin excitons, in agreement with calculations that predict significant exchange interactions.

Contents

Acknowledgments

I'd like to thank my labmates, my advisor Graham Fleming, and especially those whose effort helped me to learn the sometimes arcane art of doing experiments: Liang Guo, Arijit De, and Tom Oliver.

Thanks to Sophie for her constant support and belief in me
to Marissa, David, Daniel, Laura, Esther, Nate, Mark, and Max
(whose friendship has long helped me find my way)
to Eric, Arielle, and the cycling community
and to my family.

The things most worth doing are too big to finish alone.

1 Introduction

1.1 Photosynthesis and Optoelectronics

The Sun provides 120,000 terawatts (TW) of energy to the Earth's surface, making it far more abundant than any other energy source available. Of that, 100 TW is captured through photosynthesis by organisms around the world [1]; in 2014 humans harvested about 1/20 TW through solar power [2]. As Lewis and Nocera argued [3], with no viable fusion power expected in coming decades, solar power is the *only* source capable of satisfying projected growth in global energy demand (up to 30 TW), without incurring exponential increases in atmospheric carbon and severe consequences to global climate.

The success of solar power technology depends on lowering its cost without sacrificing reliability and efficiency. Doing so requires understanding the physics that enable efficient light harvesting and energy transport. These processes, whether in an optoelectronic material (such as photovoltaics and LEDs) or in photosynthetic pigment-protein complexes, are efficient in part because they are extremely fast. On femto- to picosecond timescales, excitation and charge transport processes can only be tracked by using short, precisely timed laser pulses: ultrafast spectroscopy. Using ultrafast techniques to study both natural light harvesting and optoelectronics provides an opportunity to use lessons from biology to engineer the function of materials.

There is a striking contrast between silicon-based solar cells and the machinery used so effectively by nature. First, while the band structure of silicon can be tuned using dopant atoms chosen for their electronic configuration, the molecular machinery of photosynthesis is composed using only a small part of the periodic table. Within this composition constraint light-harvesting function must be optimized and regulated using the pigment separation, orientation, and electron-nuclear interactions. Second, excitation energy moves through a photosynthetic antenna as bound electron-hole pairs (excitons). In an inorganic photovoltaic material, weakly bound excitons dissociate into free carriers that move to oppositely charged electrodes. The free carriers exist with a continuum of energies above a semiconductor's band edge, while the more strongly bound photosynthetic exciton states are quantized in energy. This means that while a semiconductor absorbs any photon with energy above its band gap, the absorption spectrum of a photosynthetic antenna must be broadened through pigment-protein interactions. Third, while the solar panel industry relies on high quality processing to create materials with few defects and high charge carrier mobility, nature collects solar energy using pigments embedded in soft, self-organized and disordered proteins. The strong electrostatic fluctuations in such a protein environment tend to decrease the size of excitons, localizing them on a few pigment molecules in what is an example of the effect that Maximilian Schlosshauer named einselection ("environmental selection") [4]. The contrast between excitations in a semiconductor and photosynthetic complex is illustrated in Figure 1.1.

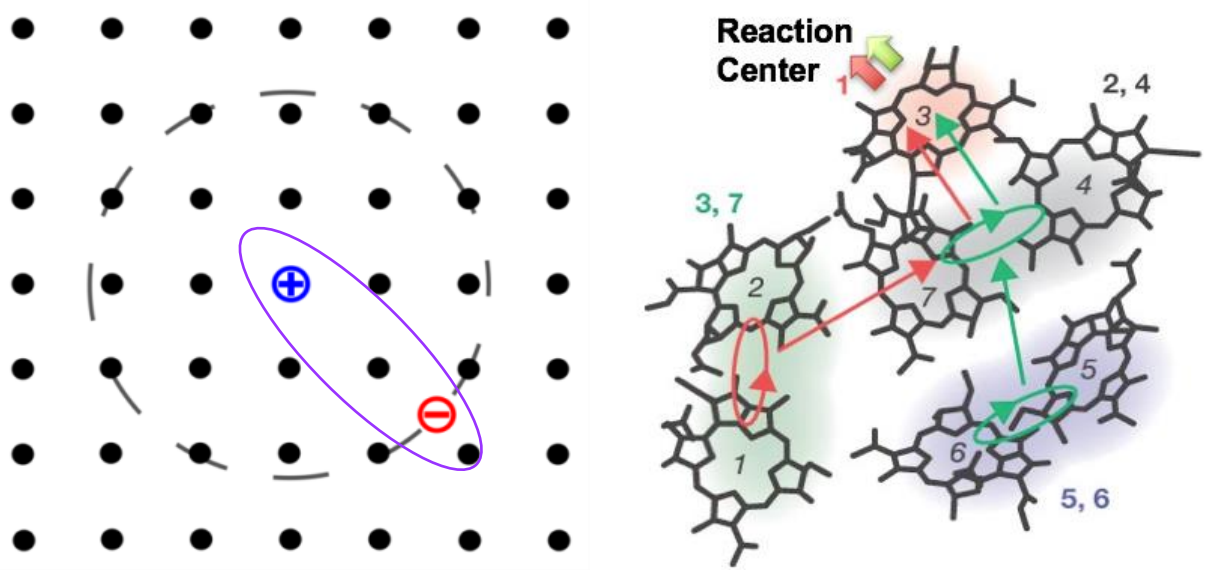

Figure 1.1 Left – Sketch of an exciton in a semiconductor lattice, which can dissociate to make free carriers. If (as shown) the exciton binding is weak enough that the electron and hole are separated by multiple unit cells of a crystalline lattice, it is called a Wannier-Mott exciton. Right – Scheme of photosynthetic excitons delocalized over a few closely packed pigments in the Fenna Matthews Olson complex from green algae (adapted from Reference [5]). Here, a stronger exciton binding energy creates much smaller Frenkel excitons.

Several recent semiconductor innovations begin to bridge this difference in paradigm between optoelectronics and biological light harvesting. Organic photovoltaics (OPVs) made of conductive polymers are inexpensive, lightweight, and easily tuned. As with photosynthetic complexes, OPVs rely on exciton transport to move energy from a light harvesting region to a region for charge separation. However, lacking long-range order, they suffer from small exciton diffusion lengths, and their efficiency is limited to 10-12%.[6] Hybrid organic-inorganic perovskite photovoltaics (HOIPs), on the other hand, achieve efficient exciton dissociation, and high carrier mobility, slow charge recombination, and consequently efficiencies of over 20% [7]. With solution dip-coating and printing processes, HOIP solar modules are expected to be produced at 1/3 the cost of the comparable silicon-based devices.[8] A better understanding of how the structure and composition of these materials leads to their remarkable function is still needed to fully optimize their properties.

By generating charge carriers with a short laser pulse, waiting a precise time interval, and then probing the system with another pulse, charge carrier relaxation can be measured with femtosecond resolution. As hot electrons quickly lose energy and cool to the band edge states, the pump-induced bleaches measured by the probe are red-shifted. As electrons recombine with holes over time, the bleaches disappear. Similarly, red shifting signals in pump-probe transient absorption spectroscopy can be used to track energy transfer between photosynthetic excitons. However, the information provided in a pump-probe spectrum is limited by its lack of pump frequency resolution. As discussed later in Section 1.2, 2D Electronic Spectroscopy (2D-ES) is a more detailed method for measuring both ultrafast energy transfer processes and the influence of environmental fluctuations on electronic states. During my PhD, I have focused on using 2D-ES

to understand light-harvesting and especially the role that electron-phonon coupling plays in photosynthetic complexes and optoelectronic materials.

In Chapter 2 of this thesis, I will discuss the difficulty in distinguishing vibrational, vibronic, and electronic coherence beats in 2D spectra, and the role of environmental fluctuations in determining the impact of small vibrational-electronic couplings on energy transfer processes in photosynthetic complexes. The numerical simulations presented in this chapter were designed to be most relevant to understanding previous 2D-ES studies of the Fenna-Matthews-Olsen complex (FMO) from green photosynthetic algae. Chapter 3 describes the strategies developed and implemented to enable new measurements on very dilute, thin, or highly scattering samples. These include an improved method of scatter elimination and fluorescence detection. Chapter 4 chronicles my observations of 2D-ES spectral beating from coherent phonons in a perovskite photovoltaic, methylammonium lead iodide, and discusses how a "phonon bottleneck" effect might slow the cooling of hot carriers. In contrast to the perovskites and photosynthetic complexes, the reduced dimensionality of single-layer MoS_2 semiconductors leads to strong electronic many-body interactions and a reduced impact of environmental fluctuations. Chapter 5 describes my work alongside Liang Guo to apply 2D-ES to study excitons and the exchange interaction in single layer MoS_2.

1.2 Electron-Phonon Interactions

Each of these studies in this dissertation demonstrates that a physical understanding that primarily focuses on electronic states and their interaction, without carefully considering the impact of phonons and environmental fluctuations, will fail to capture the physics that allow for the fine control and optimization of energy and charge transport processes. It will be useful to consider three different facets of the electron-phonon interaction:

a) **Coupling to overdamped vibrational "bath" modes:** The fluctuations and reorganization of nuclear structure around a newly generated excitation are responsible for the dynamical localization of excitons, line shape broadening, solvation effects in liquids, and polaron formation in semiconductors. As Ishizaki et al. showed, [9] the most efficient energy transfer in PPCs occurs when the electronic coupling (initial delocalization) is balanced by environmental reorganization (localization at a destination minimum energy site). Furthermore, as will be seen in Chapter 3, the bath fluctuations at physiological temperatures play an important role in weakening the effect of vibronic resonances on energy transfer. In semiconductors, these memory-less fluctuations feature in models of dielectric screening, which controls exciton binding energies, carrier-carrier scattering, and carrier recombination. Smooth exponential dynamics without any oscillations are characteristic of overdamped vibrations.
b) **Coupling to underdamped (non-Markovian) vibrational modes:** Underdamped vibrations oscillate more rapidly than they decay. Coupling to these modes can lead to enhanced energy transfer through vibronic resonances (e.g. in pigment protein complexes, Chapter 3). They can also be populated upon electronic excitation in violation of the Born-Oppenheimer approximation, and observed as evidence that a non-equilibrium phonon bottleneck could impede hot carrier cooling (in perovskite, Chapter 4).
c) **Indirect effects of local nuclear structure and dynamics:** Nuclear structure controls variations in the shape and overlap of electronic states, as well as the dielectric properties of

the material. For example, in light harvesting complexes, the protein structure is optimized to hold chlorophyll molecules much closer together than would be possible in solution, resulting in stronger electronic coupling and the strong exchange interactions that make charge transfer possible. In methylammonium lead iodide perovskite, recent theoretical studies suggest that the organic cation does not couple directly to charge carriers. Instead, the cation's rotational dynamics play an important role in determining the inorganic lattice octahedral tilting and unit cell volume. This structural effect then determines the electronic band structure, so that the optoelectronic properties to depend significantly on the cation motion. Dielectric screening also decreases below 160 K, when methylammonium cations become ordered, and bound excitons can be observed. In MoS2, dielectric screening is similarly reduced when the material is mechanically exfoliated to form single layers, and the monolayer contains strongly bound excitons and strong carrier-carrier interactions (see Chapter 5).

1.3 Two-Dimensional Electronic Spectroscopy (2D-ES)

2D-ES is a four-wave mixing experiment that yields a time-resolved correlation map of excitation and emission frequencies. In contrast to 1-dimensional spectroscopy, 2D spectra have two frequency axes. Distributing spectral information along two axes allows decongestion of complicated spectra, and separates the intrinsic homogeneous linewidth from inhomogeneous ensemble broadening. This makes 2D spectroscopy especially useful when studying energy transfer processes in inhomogeneous systems. As sketched in Figure 1.2, each transition in the linear absorption spectrum has corresponding diagonal peaks in a 2D spectrum. Cross-peaks in the 2D spectrum show correlations between excitation at one frequency and the absorption measured at the other frequency. Positive signals can be caused by a stimulated emission or a ground state bleach, while transitions to a higher excited state cause negative signals.

2D spectra can be obtained with different waiting time delays between excitation and detection. Figure 1.3 is a sketch of such a waiting time series. While the relative amplitude and peak shapes in a 2D spectrum can be distorted by the uneven spectral content of the laser pulses, the waiting time dynamics can provide reliable information on a number of physical processes. The amplitude decay of the diagonal peaks, for instance, represents the decay of the excited states. Cross-peaks at $T = 0$ indicate electronic coupling, which causes photo-induced frequency and line shape changes [10]. The growth of cross-peaks represents energy transfer between excited states. Changes in peak shape, namely a progressive broadening along the anti-diagonal direction, show the timescale for spectral diffusion and sub-ensemble memory loss. Finally, as will be discussed below, oscillatory amplitude beating over the waiting time affords valuable information on the coherent evolution of vibrational wavepackets and nonstationary electronic superposition states.

It is important to note that many of the dynamics measured in 2D spectra may also be accessible in pump-probe transient absorption measurements, in which only the probe axis is frequency resolved. However, without pump frequency resolution, overlapping features can be a problem. Measuring weak coherence oscillations in a pump-probe or transient absorption spectrum can be especially difficult because different pump frequencies may excite different frequency coherences, which are washed out in the sum. Therefore two-dimensional spectroscopy is a more sensitive method.

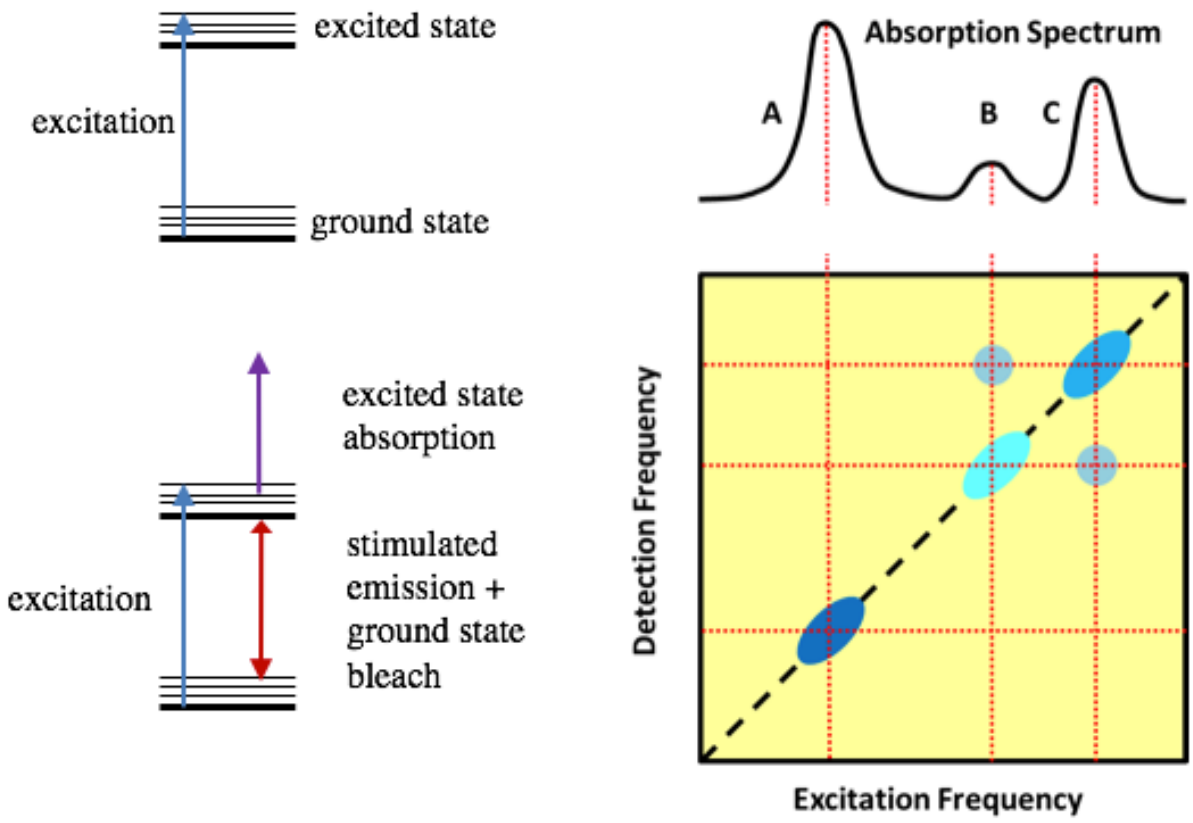

Figure 1.2 Top – Linear absorption level diagram and resulting spectrum. Linear absorption spectra have a single width determined by a combination of the transition's intrinsic lifetime and the ensemble inhomogeneity. Bottom – 2D electronic spectroscopy level diagram and resulting spectrum. 2D spectra are a correlation map between excitation and detection frequencies. The anti-diagonal width of a peak is determined by the intrinsic lifetime, while the diagonal width gives the inhomogeneous broadening.

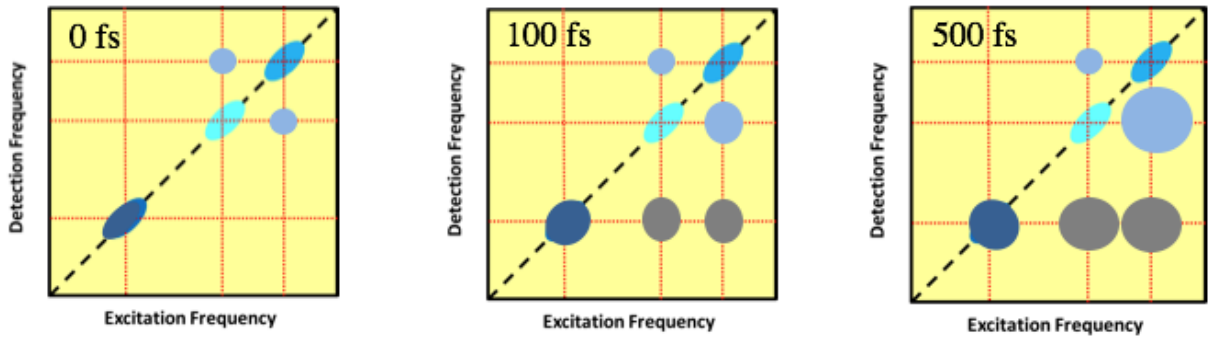

Figure 1.3: Sketch showing 2D spectra at different waiting times, T. The appearance of a cross-peak at T=0 indicates the presence of electronic coupling. Cross-peaks grow in as a consequence of population relaxation. Spectral diffusion causes anti-diagonal broadening in all peaks.

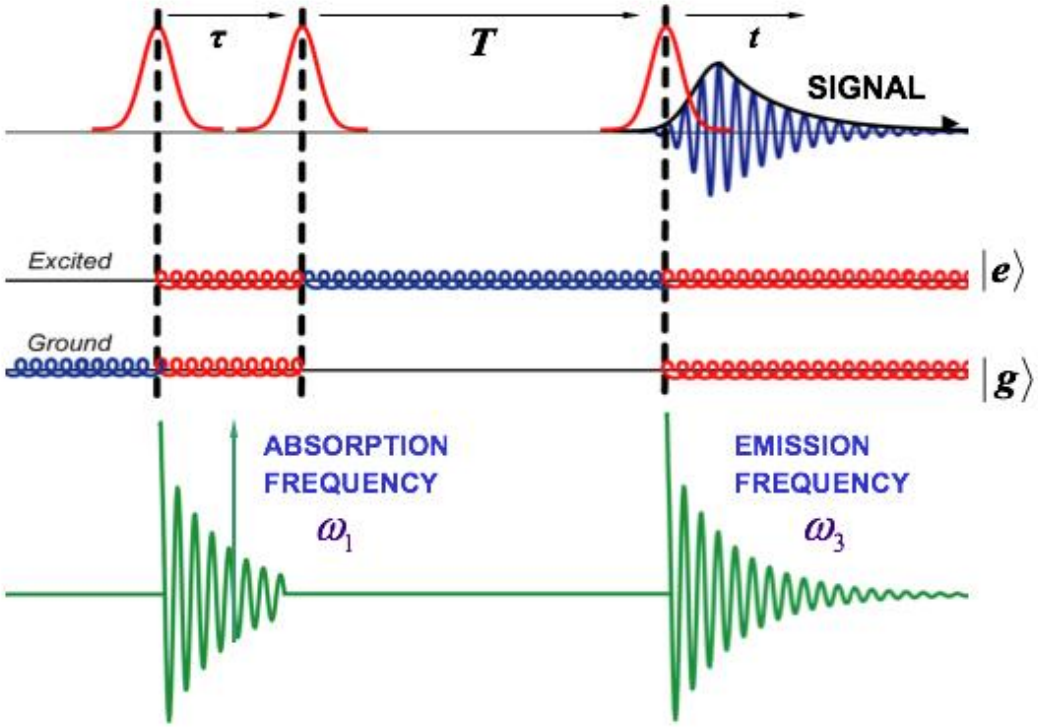

Figure 1.4 Sequence of pulses and time delays used in 2D spectroscopy (figure adapted from Ref. [10]).

Figure 1.4 shows the sequence of laser pulses and delays used to obtain a 2D spectrum. Two interferometrically phase-stable pump pulses are used to generate excitation. By placing a detector in a specific phase-matched direction, as shown in Figure 1.5, the signal corresponding to a linear electric field interaction with each pulse can be isolated.

The first field interaction creates a polarization, or a superposition of the ground and excited states. This nonstationary state evolves in a free induction decay, with frequency matching the energy separation between ground and excited state. A second pump pulse interaction converts any remaining polarization into ground or excited state populations. By scanning the delay τ between pump pulses, this free induction decay is measured in the signal. A Fourier transform over τ then gives the frequencies of the electronic transitions. This excitation frequency is plotted on the horizontal axis of a 2D spectrum.

After a given waiting time T, a third pulse is used to probe the system. The linear field interaction with this pulse creates another ground-excited state superposition. As this polarization oscillates and decays, it emits radiation in the phase-matched direction. A weak reference beam called a local oscillator (Pulse 4 in Figure 1.5) can trace the path of this signal, and the spectral interference between the two is imaged using a spectrometer and CCD camera. An inverse Fourier transform gives the signal as a function of time *t* (which is not controlled in the experiment). The signal is filtered in the time domain to remove the scatter and local oscillator contributions, and then Fourier transformed back into the frequency domain. This detection frequency is plotted on the vertical axis of a 2D spectrum.

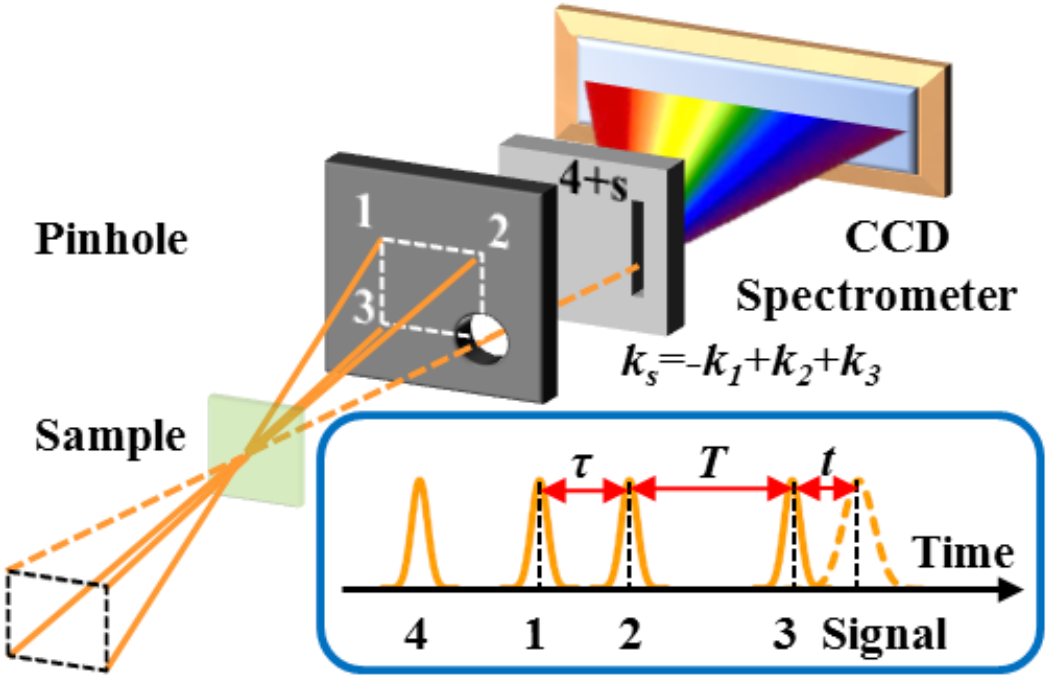

Figure 1.5 Detection setup for 2D-ES in the boxcar geometry. Four beams, denoted as 1, 2, 3, and 4, are focused into the sample forming a square pyramid. The fields with wave vectors $\mathbf{k_1}$, $\mathbf{k_2}$, and $\mathbf{k_3}$ interact with the sample generating a signal field in the phase matching direction with wave vector $\mathbf{k_s} = -\mathbf{k_1}+\mathbf{k_2}+\mathbf{k_3}$. The signal travels collinearly with beam 4 (the local oscillator) and is measured in heterodyne.

Groups around the world have implemented variations on 2D electronic spectroscopies, each with their own advantages and disadvantages. While a complete review of these arrangements is beyond the scope of this thesis, the three different 2D setups currently available in the Fleming lab provide an interesting cross-section of strategies. The original Brixner "boxcar" geometry pictured in Figure 1.5 divides beams using a diffractive optic and generates the delay τ using glass wedges. This setup's main advantage is that the signal is emitted in a background-free direction, but it is also relatively inexpensive. In contrast, 2D-ES in the pump-probe geometry is easy to set up but requires a costly pulse shaper to generate delays between collinear pump pulses, and the signal is emitted in the direction of the probe beam. The setup currently used for 2D electronic vibrational spectroscopy in our lab uses the pump-probe geometry. Finally, the setup for fluorescence-detected 2D-ES also generates delays using a pulse shaper, but it does not use phase matching to isolate the desired signal. Instead, the pulse shaper must be used to implement phase cycling (described in Chapter 2). In summary, all successful 2D-ES setups require both a method for generating phase-stable time delays between pulses and a method for isolating the third order nonlinear signal.

1.4 Coupling and Cross-Peaks

Resolving the ultrafast dynamics of cross-peaks is a unique capability of 2D electronic spectroscopy. Cross-peaks at $T = 0$ are particularly interesting because they provide a measure of correlations between electronic transitions, which are caused by interactions in the excited state. For example, in a semiconductor with low excitation density, charge carriers are far enough apart that their interactions are negligible. Similarly, in a dilute solution, electronic transitions on different molecules are not correlated. With independent electronic transitions, the probe absorption signal from a second excitation is exactly canceled by the ground state depletion from the first excitation, and no cross-peak appears at $T = 0$ [10].

The interactions between free carriers in a semiconductor are given by the Coulomb potential,

$$V(r) = kq_1q_2/r$$

Equation 1.1

for charges q_1 and q_2 separated by distance r. As the excitation density increases, the average distance between charge carriers decreases, and the coulomb interaction becomes significant. In a neutral molecule or bound electron-hole pair, the dipole-dipole interaction is instead responsible for electronic coupling:

$$V(r) = \frac{ku_1u_2}{r^3}(\cos\theta_{12} - 3\cos\theta_1\cos\theta_2)$$

Equation 1.2

where θ_{12} is the angle between electric dipoles u_i (not to be confused with the transition dipole moment). Because the dipole-dipole interaction decreases as r^3, strongly coupled molecular chromophores must be closely packed with a face-to-face orientation that minimizes θ_{12}.

Because they are interactions between molecules in the excited state, the coulomb and dipole-dipole couplings cause the frequency and lineshape of a transition to depend on whether another transition came before. When electronic transitions are thus correlated, the excited state absorption signal is no longer exactly canceled by a ground state bleach (see Figure 5.7 for an illustration in the case of MoS_2 semiconductor), and a cross-peak appears even at $T = 0$. This correlation cross-peak does not indicate any population transfer. Correlation cross-peaks should initially appear symmetric above and below the 2D diagonal, and decay on a timescale with the population excited by the same pump frequency. The dynamics of cross-peaks in 2D spectra will be discussed further in the context of experiments on the semiconductor MoS_2 in Chapter 5.

1.5 Spectral Beats, Wavepackets, and the Evolution of Coherent States

Because 2D-ES provides a correlation map between absorption and emission frequencies, representing the eigenstates of the electronic Hamiltonian, it might be tempting to assume that waiting time dynamics describe a trajectory starting from populations in these eigenstates. Because eigenstates are stationary in time, one would only observe population relaxation to thermal equilibrium as induced by the system-environment interactions. However, the starting conditions for dynamics observed in a series of 2D spectra are not the eigenstates. The impulsive pump generates a coherent superposition of all accessible electronic and vibrational states, with

contributions weighted according to the strength of the transition dipole moment. More explicitly, the coupling between ground and singly excited states induced by an optical field *E(t)* may be written as

$$\mathrm{V}(t) = \sum_{\mathrm{i}} -\mu_{\mathrm{i}}\mathrm{E}(\mathrm{t})(|\mathrm{i}\rangle\langle\mathrm{g}| + |\mathrm{g}\rangle\langle\mathrm{i}|)$$

Equation 1.3

where $\mu_i = \langle i|q\boldsymbol{r}|g\rangle$ is the transition dipole moment between the ground state and $|i\rangle$. For simplicity in this illustration, transitions between excited states have been neglected. We can also use the interaction picture to account for time evolution due to the system Hamiltonian:

$$\mathrm{V_I}(t) = \mathrm{e}^{\frac{-\mathrm{iHt}}{\hbar}}\mathrm{V(t)e}^{\frac{\mathrm{iHt}}{\hbar}}$$

Equation 1.4

where $H = \sum_i \epsilon_i |i\rangle\langle i|$. With weak excitation, the effect of the transition can be estimated using a second-order perturbation series solution to the Liouville equation:

$$\rho_{\mathrm{I}}(\mathrm{t}) = \rho_0 - \left(\frac{\mathrm{i}}{\hbar}\right)\int_0^{\mathrm{t}} \mathrm{dt}_1[\mathrm{V_I}(\mathrm{t}_1), \rho_0] + \left(\frac{-\mathrm{i}}{\hbar}\right)^2 \int_0^{\mathrm{t}} \mathrm{dt}_2 \int_0^{\mathrm{t}_2} \mathrm{dt}_1[\mathrm{V_I}(\mathrm{t}_2), [\mathrm{V_I}(\mathrm{t}_1), \rho_0]]$$

Equation 1.5

Let's further assume excitation by a single infinitely short pulse arriving at t=0,[†] and that phase matching and/or phase cycling methods have been used to isolate the signal proportional to $|E|^2$. Then the signal depends only on the second order term $\rho^{(2)}$. Evaluating the commutators with $\rho_0 = |g\rangle\langle g|$, we obtain

$$\rho^{(2)}(0) = \left(\frac{1}{\hbar}\right)^2 |\mathrm{E}|^2 \sum_{\mathrm{i}} 2\mu_{\mathrm{i}}{}^2\,(|\mathrm{i}\rangle\langle\mathrm{i}| - |\mathrm{g}\rangle\langle\mathrm{g}|) + \sum_{\mathrm{i}\neq\mathrm{j}} \mu_{\mathrm{i}}\mu_{\mathrm{j}}\,(|\mathrm{i}\rangle\langle\mathrm{j}| + |\mathrm{j}\rangle\langle\mathrm{i}|)$$

Equation 1.6

Therefore, in addition to converting ground to excited state populations, the light-matter interaction generates off-diagonal "coherence" terms between every pair of states with nonzero transition dipole moment. The existence of the coherence terms means that $\rho^{(2)}(0)$ does not commute with *H* and the prepared state is not a linear combination of the eigenstates of *H*. Therefore, the population coefficients in this superposition oscillate in time, and yield oscillating absorption cross-sections that modulate the 3rd order signal.

If the initially prepared state is primarily a mixture of different vibrational levels, it is called a vibrational wavepacket. The wavepacket's initial amplitude is determined by the Franck-Condon factor for the vibronic transition, *FC*. For a transition originating on the ground vibrational state,

[†] While a large range of τ delays might be needed to accurately measure the absorption line shape, the spectrum amplitude is determined by the data points near $\tau = 0$, when absorption is strongest.

$$\mathrm{FC} = \frac{\mathrm{S}^{\mathrm{v}}\mathrm{e}^{-\mathrm{S}}}{\mathrm{v}!}\delta(\omega - \omega_{vib}\mathrm{v})$$

Equation 1.7

where v is the vibrational quantum number and $S = D^2/2$ is the Huang-Rhys factor for a dimensionless displacement D between the vibrational equilibrium point on the ground and excited electronic states. As observed in a pump-probe measurement in iodine by Scherer, Jonas and Fleming [11], the coherent vibration evolves as a decaying sinusoid.

The decay of coherence oscillations is composed of two different effects that are easily confused: decoherence and dephasing. Decoherence involves permanent loss of information through coupling to an environment. It follows that coherences and wavepackets with longer oscillation decays are less strongly coupled to environmental degrees of freedom. Dephasing, however, is only the apparent decay of a signal originating from many different uncoupled oscillators with slightly different frequency. While every oscillation begins with the same phase (determined by the phase of the light field), the different frequencies ensure that their phases evolve at different rates, so that eventually there is destructive interference. Ensemble dephasing has sometimes been called "fake decoherence" because, in the absence of "true decoherence", the oscillators will eventually return to a position of common phase. Photon echo spectroscopies (including 2D-ES) remove the effect of ensemble broadening on the absorption spectrum by detecting a rephasing or echo signal. However, an echo spectroscopy that would eliminate ensemble dephasing from the second-order coherences described in
Equation 1.6
would require measuring a 7^{th}-order signal! Alternatively, one could detect signals from single molecules or small ensembles; this idea inspired the development of fluorescence-detected 2D-ES and will be discussed in Chapter 2.

Upon decoherence, a vibrational wavepacket spreads out and becomes a standing wave without strong time dependence. The populations in different modes and levels fluctuate without any correlation, and at no time do they interfere to localize the vibrational energy. On the other hand, electronic excitation in coupled chromophores tends to become more localized as coherent population exchanges between pigments is no longer possible. The reason these pictures are so different is that the different vibrational excitation states are all spatially overlapped (e.g. in the area of a bond), while in chromophore aggregates different singly excited electronic states tend to be spread over different pigments. Therefore, the effect of coherence between vibrational states is to enable energy localization through constructive interference; between electronic states, to allow energy delocalization through coherent energy transfer. Moreover, compared to vibrational wavepackets, pure electronic superposition states are short-lived, usually lasting only tens of femtoseconds. Lightweight, strongly charged electrons are easily perturbed by environmental fluctuations, so that spatially separated regions of a wavefunction quickly lose phase coherence. Vibrational wavepackets are more robust because nuclei are heavy and shielded from interactions by a polarizable electron cloud. Despite these differences, it is difficult to determine whether the origin of experimentally observed spectral oscillations is electronic or vibrational, or both. This problem is discussed further in Chapter 2.

2 Simulating the Impact of Vibronic Coupling on 2D Spectra and Energy Transfer

Material in this Chapter adapted with permission from Reference [12]:
"Influence of Weak Vibrational-Electronic Couplings on 2D Electronic Spectra and Inter-Site Coherence in Weakly Coupled Photosynthetic Complexes"
by Daniele M. Monahan, Lukas Whaley-Mayda, Akihito Ishizaki, and Graham R. Fleming
Journal of Chemical Physics DOI: 10.1364/OE.24.018126

Coherence oscillations measured in two-dimensional (2D) electronic spectra of pigment-protein complexes may have electronic, vibrational, or mixed-character vibronic origins, which depend on the degree of electronic-vibrational mixing. Oscillations from intra-pigment vibrations can obscure the inter-site coherence lifetime, of interest in elucidating the mechanisms of energy transfer in photosynthetic light-harvesting. Huang-Rhys factors (S) for low-frequency vibrations in Chlorophyll and Bacteriochlorophyll are quite small ($S \leq 0.05$), so it is often assumed that these vibrations influence neither 2D spectra nor inter-site coherence dynamics. In this work, we explore the influence of S within this range on the oscillatory signatures in simulated 2D spectra of a pigment heterodimer. To visualize the inter-site coherence dynamics underlying the 2D spectra, we introduce a formalism which we call the "site-probe response." By comparing the calculated 2D spectra with the site-probe response, we show that an on-resonance vibration with Huang-Rhys factor as small as $S = 0.005$ and the most strongly coupled off-resonance vibrations ($S = 0.05$) give rise to long-lived, purely vibrational coherences at 77 K. We moreover calculate the correlation between optical pump interactions and subsequent entanglement between sites, as measured by the concurrence. Long-lived inter-site coherence and site entanglement increase with S at 77 K, and this dependence all but vanishes at physiological temperature, as environmentally-induced fluctuations destroy the vibronic mixing.

2.1 Introduction

In pigment-protein complexes (PPCs) devoted to light harvesting, light absorption generates molecular excitons [13], or singly excited states delocalized over the coupled pigment molecules (sites). Two-dimensional electronic spectroscopy (2D-ES) has become the method of choice for measuring exciton dynamics on ultrafast timescales [5], [14]. The technique provides information on electronic couplings, homogeneous and inhomogeneous line shapes, and the kinetics of exciton relaxation and energy transfer from one state to another. In recent years, long-lived oscillatory signals have been measured in the 2D spectra of diverse photosynthetic complexes [15]–[20], including at physiological temperature [21], [22]. The oscillations are attributed to coherent superpositions of electronic, vibronic, and/or vibrational states. The evidence that electronic coherences may survive on sufficiently long timescales to affect the mechanism of electronic energy transfer (EET) in the photosynthetic apparatus has stimulated a

large body of work at the intersection of biophysical chemistry and quantum information [14], [23]–[25].

Understanding nature's mechanisms for energy transfer over nanoscale distances is an important milestone toward replicating the robust and efficient solar energy conversions observed in photosynthesis. Long-lived coherence allows rapid energy displacement as part of the unitary evolution of a superposition state. Further work pointed to coherence as a means for enhancing EET unidirectionality [26], [27] and robustness to energetic disorder [28]. The environment, too, plays a role in efficient energy transfer. Both by dissipating energy and by destroying superpositions before they evolve back into their initially prepared state, environmentally-induced fluctuations assist in delivering excitation to the lowest-energy pigment [29]–[31]. Ishizaki and Fleming [27] calculated that electronic coherence in the Fenna-Matthews-Olson (FMO) complex isolated from green sulfur bacteria could persist for 700 fs at 77 K and 300 fs at 300 K. At physiological temperature, the theory and experiment agree. However, oscillations measured at 77 K persist in the spectra for at least 1.5 ps [22]. It has been suggested that the long-term oscillations are due to the influence of intra-molecular vibrations [32]–[37], and that in some systems electronic-vibrational interactions enhance EET [38]–[42]. Considerable interest arose in developing analyses that distinguish between vibrational and electronic components of oscillations in 2D-ES [43]–[54], as well as time resolved measurements selective to inter-site coherence and excitation delocalization. Polarization-dependent 2D-ES experiments [17], [18], [55], [56] can be site-selective, if transition dipoles on different pigments have sufficiently different orientations. Scholes and Smyth have suggested using excited-state absorption to measure electronic delocalization that is strongly dependent on a vibrational coordinate [57], and Tempelaar *et al.* have proposed time-resolved fluorescence experiments as a means to monitor the decay of the coherence length in molecular aggregates [58].

Mechanisms that balance inter-site electronic coherence with environmentally induced decoherence on the energy transfer timescale are especially relevant if they can survive and be measured in systems that mimic the conditions of natural light-harvesting. Most photosynthetic complexes fall in the so-called intermediate coupling regime, where neither the environment nor the inter-pigment couplings are strong enough to dominate EET. A feature of the Huang-Rhys factors for the photosynthetic pigments Chlorophyll (Chl) and Bacteriochlorophyll (BChl) is that they are remarkably small ($S \leq 0.05$) [59]–[63] compared to typical values in molecular dyes, where $S \geq 0.5$ is common, and to model dimers where a clear distinction was made between vibronic and electronic coherence [52], [53]. Given the small S values in natural systems, it is tempting to conclude that intramolecular vibrations are likely to play little role in either the spectroscopy or the quantum dynamics. However, as Jonas and co-workers pointed out, [34] this may not be the case. Our goal is to clarify the role of vibrations in the small S regime in terms of their influence on two-dimensional spectra and on the underlying quantum dynamics. To this end we carried out a systematic study of the influence of for a single mode in an electronically coupled dimer. We aim to establish the phenomenology with a model that is simple enough for exact numerical calculations, incorporating the vibrational DOFs in the spectral density and not in the system Hamiltonian. This is important because the small Huang-Rhys factors make the vibronic resonance very fragile with respect to environmentally induced fluctuations, and so it is essential to treat this environmental influence to avoid overestimating the influence of near-resonant vibrations and to allow the comparison of dynamics at very different temperatures. Of course, in a real system there may be many vibrational modes that play a role. Recently Schulze

and Kühn [64] examined this issue using a zero temperature, numerically exact multilayer multiconfiguration time-dependent Hartree method on a dimer chosen from the FMO complex. Their calculation showed that a large number of weakly coupled modes participate in the dynamics, although the zero temperature assumption makes their role at physiological temperature difficult to predict.

In a recent paper [65], Ishizaki and coworkers examined the effect of environmentally induced fluctuations on the mixing between electronic and vibrational DOFs in a heterodimer inspired by BChls 3 and 4 in FMO. They included the influence of an underdamped vibration at the acceptor pigment site, with $S = 0.025$, and numerically simulated the stimulated emission, ground state bleach, and excited state absorption contributions to the 2D spectra, showing that oscillatory signals originate from dynamics on both the electronic ground and excited state. They showed that if the vibrational frequency is close to resonant with the electronic energy gap, oscillations persist in the spectra at 77 K–despite the small Huang-Rhys factor chosen. These disappear at physiological temperature, as increased fluctuations destroy the electronic-vibrational mixing. Moreover, they observed that large amplitude beating of vibrational origin emerges in the 2D spectra, but with no accompanying effect on EET dynamics. This raises the important question of the extent to which, for a given value of S, the vibration-electronic mixing in PPCs contributes to coherence between sites (correlation between the excitation state of separate pigments), or else generates only local effects such as a vibrational wavepacket. The distinction is important because only signatures of inter-site coherence indicate that coherent EET mechanisms are possible.

In this Chapter we explore the dependence of the 2D spectra on the magnitude of the Huang-Rhys factor while holding the Stokes shift constant, and we consider vibrational modes both resonant and off-resonant with the exciton energy gap. Our results are intended to be useful for interpretation of experiments on photosynthetic systems, and so we confine our calculations to the range of small S values typical of Chls and BChls in pigment-protein complexes. As Ishizaki and coworkers demonstrated [65], the observation of distinct beats in a 2D spectrum guarantees neither that electronic coherence is involved in the energy transfer, nor that intramolecular vibrations significantly enhance the energy transfer rate. In order to explore this point further, we introduce a formalism for calculating measures of inter-site coherence and entanglement dynamics. This enables a comparison of the electronic or vibronic coherence in the site basis, as a function of the Huang-Rhys factor, with the features observed in a 2D electronic spectrum.

2.2 Model

We simulate EET dynamics in a model dimer with coupling to a vibrational mode in the ground and excited states, under the influence of environmentally induced fluctuations with Gaussian statistics. Figure 2.1 shows a schematic of the excitons that result from electronic and vibronic mixing in this dimer. We use the following notation: for pigment m, $|\phi_{ma}\rangle$ with $a = g$ or $a = e$ describes the ground and first excited electronic states, respectively. $|\chi_{av}^{m}\rangle$ describes the nuclear configuration of pigment m with vibrational occupation number v on electronic state a. We consider only the ground or first excited electronic states of each pigment, although higher excited states are sometimes of consequence in nonlinear spectroscopic signals [66], [67]. As illustrated in Fig. 1, the interaction between $|\phi_{1e}\rangle|\chi_{e0}^{1}\rangle$ (the vibrational ground state on the donor

pigment) and $|\phi_{2e}\rangle|\chi_{e1}^{2}\rangle$ (a vibrationally excited state on the acceptor) creates the mixed-character vibronic excitons, $|e_1^+\rangle$ and $|e_1^-\rangle$.

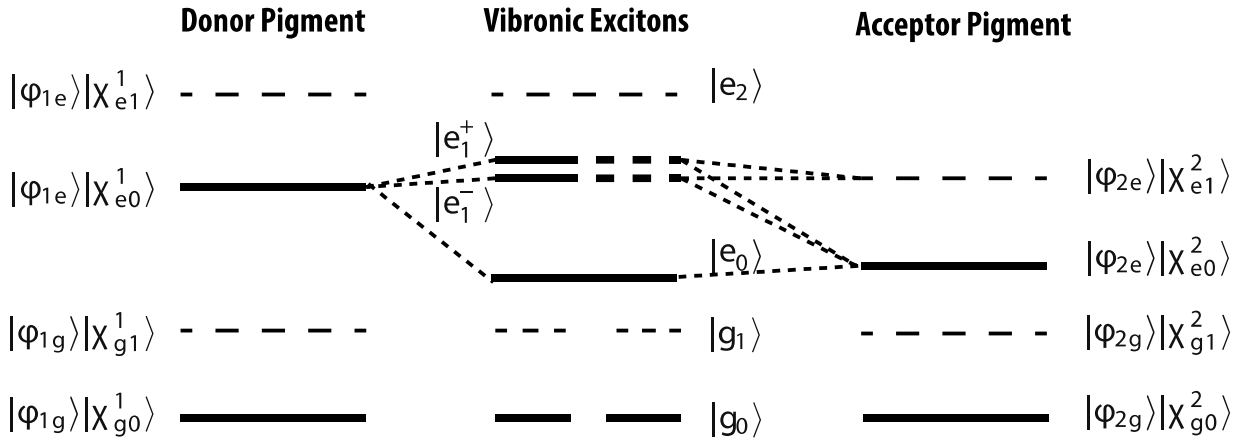

Figure 2.1 Excitons that result from vibronic mixing in a heterodimer of displaced oscillators. for pigment m, $|\phi_{ma}\rangle$ with $a = g$ or $a = e$ describes the ground and first excited electronic states, respectively. $|\chi_{av}^{m}\rangle$ describes the nuclear configuration of pigment m with vibrational occupation number v on electronic state a. Primarily vibrational energy levels are marked with dashed lines, while strongly mixed-character vibronic states are denoted with half-dashed lines. Note that the doubly excited state is included in the model but is not shown.

The details of the theoretical method used are described in Ref. [65]. The Hamiltonian for the dimer is given by

$$\hat{\mathrm{H}} = \sum_{\mathrm{m}=1}^{2} \sum^{\mathrm{a=g,e}} \hat{\mathrm{H}}_{\mathrm{ma}}\,(\mathrm{x_m})|\phi_{\mathrm{ma}}\rangle\langle\phi_{\mathrm{ma}}| + \sum_{\mathrm{m}=1}^{2}\sum_{\mathrm{n}=1}^{2} \hbar\,\mathrm{J_{mn}}|\phi_{\mathrm{me}}\rangle\langle\phi_{\mathrm{mg}}| \otimes |\phi_{\mathrm{ng}}\rangle\langle\phi_{\mathrm{ne}}|$$

Equation 2.1

where $\hat{H}_{ma}\,(x_m)$ is the diabatic Hamiltonian for the environmental and nuclear DOFs, x_m, of pigment site m in state a. The Franck-Condon transition energies are then obtained by an average over ground state environmental and nuclear DOFs,

$$\hbar\Omega_{\mathrm{m}} = \langle \hat{\mathrm{H}}_{\mathrm{me}}\,(\mathrm{x_m}) - \hat{\mathrm{H}}_{\mathrm{mg}}\,(\mathrm{x_m})\rangle_{\mathrm{mg}}$$

Equation 2.2

where $\langle \ldots \rangle_{mg}$ denotes the canonical average with respect to the environmental and nuclear DOFs associated with the $|\phi_{mg}\rangle$ ground state.

In this work, we have set the Franck-Condon transition energies to be $\Omega_1 = 400\ \mathrm{cm}^{-1}$ and $\Omega_2 = 600\ \mathrm{cm}^{-1}$, with electronic coupling $\mathrm{J} = 50\ \mathrm{cm}^{-1}$, such that $\Delta = \sqrt{(\Omega_2 - \Omega_1)^2 + 4{J_{12}}^2} = 223.6\ \mathrm{cm}^{-1}$ is the gap between the two electronic energy eigenstates. The electronic coupling, approximate energy gap, and the environment parameters (described below) are taken from values for bacteriochlorophylls 3 and 4 in the FMO complex, which were generated by simultaneous fits of measured linear absorption and 2D rephasing, nonrephasing, and polarization-dependent electronic spectra [55]. We describe the influence of the environmental and vibrational DOFs on the electronic transition of pigment m using the relaxation function [68], $\Psi_m(t)$, of the collective energy gap coordinate defined by $\hat{u}_m = \hat{H}_{me}(x_m) - \hat{H}_{mg}(x_m) - \hbar\Omega_m$. In this work, we assume that the relaxation functions for the two pigments are identical, i.e. $\Psi_1(t) = \Psi_2(t) \equiv \Psi(t)$. It should be noted that the relaxation function is independent of temperature by definition, when Gaussian fluctuations in electronic transition energies and harmonic vibrations (i.e., the linear response regime) are considered [65], [68], [69]. We take the relaxation function to have two components: an exponential decay due to the collective influence of overdamped environmental DOFs, with reorganization energy λ_{env}, and the influence of a single underdamped vibration modeled as a Brownian oscillator [70] with vibrational frequency ω_{vib} and relaxation rate γ_{vib}. The total relaxation function, including both the environmental and vibrational contributions is then

$$\Psi(t) = 2\hbar\lambda_{env}e^{-\gamma_{env}\mathrm{t}} + 2\hbar\mathrm{S}\omega_{vib}\mathrm{e}^{-\gamma_{vib}\mathrm{t}}[cos(\widetilde{\omega}_{vib}\mathrm{t}) + \frac{\gamma_{vib}}{\widetilde{\omega}_{vib}}sin(\widetilde{\omega}_{vib}\mathrm{t})]$$

Equation 2.3

where $\widetilde{\omega}_{\mathrm{vib}} = \sqrt{{\omega_{\mathrm{vib}}}^2 - {\gamma_{\mathrm{vib}}}^2}$ and S is the dimensionless Huang-Rhys factor for the underdamped vibration. Here we set the environmental reorganization timescale to ${\gamma_{\mathrm{env}}}^{-1} = 50$ fs and the vibrational dephasing time to ${\gamma_{\mathrm{vib}}}^{-1} = 2$ ps. This form of the relaxation function (Equation 2.3) yields a broad spectral density $\mathrm{J}(\omega)$ with a narrow peak in the vicinity of $\omega = \omega_{\mathrm{vib}}$, via a Kubo formula,

$$\mathrm{J}(\omega) = \omega\int_0^\infty \mathrm{d\,t}\,\Psi(\mathrm{t})\cos\omega\mathrm{t}.$$

Equation 2.4

Here, we vary S and ω_{vib} but constrain $\lambda_{\mathrm{total}} = \lambda_{\mathrm{env}} - S\omega_{\mathrm{vib}} = 35\ \mathrm{cm}^{-1}$, so that the Stokes shift $\Psi(0) = 2\hbar\lambda_{\mathrm{total}}$ is fixed in every scenario. We consider the effect of environment structure on the dynamics while holding approximately constant the dissipation associated with the response of all over- and underdamped bath modes, thus avoiding a systematic increase in the mean-squared fluctuations of the electronic transition energies. However, we note that in our approach, the effects of increasing S are not purely due to the added presence of the vibration, but also include the relative decrease in contributions from overdamped bath modes.

We compute the dynamics of observables via the reduced density matrix, for which the unobserved environmental DOFs have been traced out: $\rho_{\mathrm{exc}}(t) = \mathrm{Tr}_{\mathrm{env}}[\rho(t)]$. For ease of notation, we will write $|g\rangle = |\phi_{1g}\rangle|\phi_{2g}\rangle$ for the collective ground state, $|m\rangle = |\phi_{me}\rangle|\phi_{ng}\rangle$ for the electronic state with pigment m in its first electronic state and pigment n in its ground state,

and $|12\rangle = |\phi_{1e}\rangle|\phi_{2e}\rangle$ for the doubly excited state. In deriving the equation of motion, following Appendix A of Ref. [65], we begin from the response function and the symmetrized correlation function of the collective energy gap coordinate. The response function is simply expressed in terms of the relaxation function as $\Phi(t) = -(d/dt)\Psi(t)$. The symmetrized correlation function can be expressed in terms of the spectral density as

$$\mathrm{D(t)} = \frac{\hbar}{\pi}\int_0^\infty \mathrm{d}\,\omega \mathrm{J}(\omega)\coth\frac{\beta\hbar\omega}{2}\cos\omega\mathrm{t}.$$

Equation 2.5

For the model described by Equation 2.3, the integrand of
Equation 2.5 has four singularities $\omega = \pm\widetilde{\omega}_{vib} \pm i\gamma_{\mathrm{vib}}$, in addition to an infinite number of singularities $\omega = \pm\nu_k$ $(k = 1,2,\dots)$ where $\nu_k = \frac{2\pi k}{\beta\hbar}$ are the Matsubara frequencies. Hence
Equation 2.5 may be recast into the form of an infinite series. However, in order to reduce the computational cost of calculating 2D electronic spectra for various waiting times, we approximate
Equation 2.5 as

$$D(t) \approx k_{\mathrm{B}}T\cdot\Psi_{\mathrm{env}}(t) + \hbar^2 S\frac{\omega_{\mathrm{vib}}^3}{2\widetilde{\omega}_{vib}}\left[\coth\frac{\beta\hbar(\widetilde{\omega}_{vib}+i\gamma_{\mathrm{vib}})}{2}e^{-i(\widetilde{\omega}_{vib}+i\gamma_{\mathrm{vib}})t} + c.c.\right]$$

Equation 2.6

where $\Psi_{\mathrm{env}}(t)$ denotes the overdamped environmental component of the relaxation function given in Equation 2.3. In the first term of the right-hand side of Equation 2.6, we have assumed that the classical fluctuation-dissipation relation applies to the environmental dynamics by omitting the quantum components of the fluctuations, characterized by the Matsubara frequencies. The drawback of this assumption is that we deviate from the exact detailed balance condition and thus a breakdown of the positivity condition for the population is possible. In this work, however, we focus on coherence dynamics under the influence of the environmentally-induced fluctuations, so that this drawback is of no consequence. In the second term, on the other hand, the hyperbolic cotangent function indicates that the quantum zero-point energy of the nuclear vibration is properly taken into account. In deriving the expression, it has been assumed that the vibrational component of the spectral density does not resonate with the Matsubara frequencies. This assumption is reasonable as long as we consider slow vibrational dephasing times and correspondingly sharp peaks in the spectral density [65]. Thus, both the response function and the symmetrized correlation function are expressed in terms of exponential functions, as required in Eq. (A8) of Ref. [65].

In the simplest picture, the electronic coherence oscillations appear on the cross-peak in the rephasing spectrum and on the diagonal peaks in the nonrephasing spectrum [14]. Therefore, to better separate the oscillatory dynamics from population relaxation, we focus on the rephasing 2D spectra. Assuming infinitely broadband laser pulses, the rephasing 2D spectrum is given by

$$S_R(\omega_1, t_2, \omega_3) = \int_0^\infty dt_3 e^{i\omega_3 t_3} \int_0^\infty dt_1 e^{i\omega_1 t_1} i R_R(t_3, t_2, t_1).$$

Equation 2.7

In Equation 2.7, $R_R(t_3, t_2, t_1)$ is the third-order response function for the rephasing signal expressed as [71] ,

$$R_R(t_3, t_2, t_1) = i^3 \mathrm{Tr}[\mu_{\leftarrow} \mathcal{G}(t_3) \mu_{\rightarrow}^{\times} \mathcal{G}(t_2) \mu_{\rightarrow}^{\times} \mathcal{G}(t_1) \mu_{\leftarrow}^{\times} \rho_{\mathrm{exc}}(-\infty)]$$

Equation 2.8

where $\rho_{\mathrm{exc}}(-\infty)$ is the equilibrium reduced density operator for the electronic ground state. The operator $\mathcal{G}(t_i)$ describes the time evolution and relaxation during the intervals between pulses t_i. For simplicity, we assume parallel transition dipoles of unit magnitude for both sites. In this case, the operators that describe interaction with the identically polarized laser pulses are $\mu_{\leftarrow} = |g\rangle\langle 1| + |g\rangle\langle 2| + |1\rangle\langle 12| + |2\rangle\langle 12|$ and $\mu_{\rightarrow} = [\mu_{\leftarrow}]^{\dagger}$. We have used the superoperator notation $\mu^{\times} \hat{\mathcal{O}} = [\mu, \hat{\mathcal{O}}]$ to simplify the appearance of commutators in Equation 2.8.

2.3 Site-probe response

The excitation population on site m is given by

$$P_m(t) = \mathrm{Tr}\Big[|m\rangle\langle m| \mathcal{G}(t) \rho_{\mathrm{exc}}^{(1)}(0)\Big],$$

Equation 2.9

where the reduced density operator $\rho_{\mathrm{exc}}^{(1)}(0)$ describes the chosen initial condition for the electronic DOFs in the single excitation manifold. For example, if the initial population is localized on the donor pigment, then $\rho_{\mathrm{exc}}^{(1)}(0) = |1\rangle\langle 1|$. Ishizaki and coworkers demonstrated that for a dimer under the influence of environmentally induced fluctuations, a vibronic resonance can greatly impact the 2D-ES measurement without strongly affecting the relaxation to equilibrium of an excitation initially located on the donor pigment [65]. They called attention to the high sensitivity of nonlinear measurements to coherent dynamics that may only play a small role in the overall energy transfer process.

In this work, we examine the correspondence between the spectroscopic measurement and the coherent aspects of dynamics in the site basis. To this end, we introduce the theoretical formalism for a site-specific nonlinear measurement, which we call the "site-probe response,"

$$S_m(\omega_1, t_2) = i^2 \int_0^\infty dt_1 e^{-i\omega_1 t_1} \times \mathrm{Tr}[|m\rangle\langle m| \; \mathcal{G}(t_2) \; \mu_{\rightarrow}^{\times} \mathcal{G}(t_1) \mu_{\leftarrow}^{\times} \rho_{\mathrm{exc}}(-\infty)]$$

Equation 2.10

where $m = 1,2$ indicate projection on the donor and acceptor pigments, respectively. This quantity is analogous to the optical response in Equation 2.8. Whereas site population dynamics represent energy transfer as a given site population relaxes to equilibrium, the site-probe response represents dynamics of correlation between pump-induced optical polarizations and the site population, just as the third-order optical response represents dynamics of correlation between pump and probe optical polarizations. In terms of the "doorway-window" picture of Fried and Mukamel [70], [72], the site-probe response employs the same two-pulse "doorway function" as is used to calculate the 2D spectrum, $\mathcal{D} = \mu^{\times}_{\Rightarrow}\mathcal{G}(t_1)\mu^{\times}_{\Leftarrow}$. After time propagation with $\mathcal{G}(t_2)$, the "window function" (or measurement) is given by $\mathcal{W}_m = |m\rangle\langle m|$, the projection onto the excited state localized at site m. This site projection replaces the third pulse interaction and resulting signal field ($\mathcal{W} = \mu\mathcal{G}(t_3)\mu^{\times}_{\Leftarrow}$ in Equation 2.8), and provides a site-specific measure of the system dynamics after the pump excitation. With a Fourier transform over the "doorway" coherence time t_1, we obtain the site-probe response as a function of absorption frequency ω_1.

Just as oscillations in the 2D spectrum show coherent energy flow between excited states, oscillations in the site-probe response show coherent flow between pigment sites. The site-probe oscillations depend on the presence of coherences between excitons, as they are a direct consequence of the unitary dynamics of coherent exciton superpositions. However, not all exciton coherences produce site-probe oscillations. For instance, in a coupled dimer with a small mixing angle, the excitons are localized on the sites. Hence $[|m\rangle\langle m|, H] \approx 0$, and thus the site projection measurement is time-independent except for dissipation, even if the excitons were prepared in superposition. In this scenario, the site-probe response is just proportional to the excited state population, and hence to the contribution to the spectrum from either stimulated emission or excited state absorption. However, as J_{12} and the mixing angle increase, dynamics in the site-probe response increasingly represent a mixture of exciton population and coherence dynamics. Due to this mixing, there is no simple correspondence between the phase of the site response oscillations and oscillations at any single point in a 2D spectrum; nonetheless, the presence of site-probe oscillations reports when coherent energy transfer occurs. The site projection measurement is blind to the vibrational DOFs, so that while a localized vibrational wavepacket may give rise to long-lived oscillations in the 2D-ES, the site-probe response is insensitive to purely vibrational effects.

2.4 Results and Discussion

2.4.1 Simulated 2D-ES

We simulate the rephasing 2D electronic spectra, Equation 2.8 and site-probe response, Equation 2.10 across waiting time t_2 for an electronic heterodimer with coupling to a vibrational mode in the ground and excited electronic manifolds. The simulations are split into two cases. In the first case, the vibrational frequency matches the pure electronic energy gap $\omega_{\text{vib}} = \Delta = 223.6\ \text{cm}^{-1}$. This leads to two closely spaced vibronic excitons $|e_1^+\rangle$ and $|e_1^-\rangle$ in addition to $|e_0\rangle$ (see Figure 1.1). In the second case, the vibration is off-resonant, $\omega_{\text{vib}} = \Delta +\ \text{cm}^{-1}$. This study is limited to small Huang-Rhys factors, $0 \leq S \leq 0.05$, which correspond to the range of values measured for individual vibrational modes in BChl and Chl in low-temperature glasses [62]. In the FMO complex, several low-frequency vibrations [59], [61] have been identified with Huang-Rhys factors $0.008 \leq S \leq 0.015$; the strongest low-frequency mode measured has $S = 0.05$.

Figure 2.2a shows the simulated linear absorption spectrum of the dimer for a range of S-values and with the constraint $\lambda_{\text{total}} = \lambda_{\text{env}} - S\omega_{\text{vib}} = 35\ \text{cm}^{-1}$. Maintaining a constant Stokes shift ($2\hbar\lambda_{\text{total}}$) prevents a strong S-dependence in the linear absorption peak positions and widths, and is key to making a useful comparison of spectra across a range of vibronic couplings.

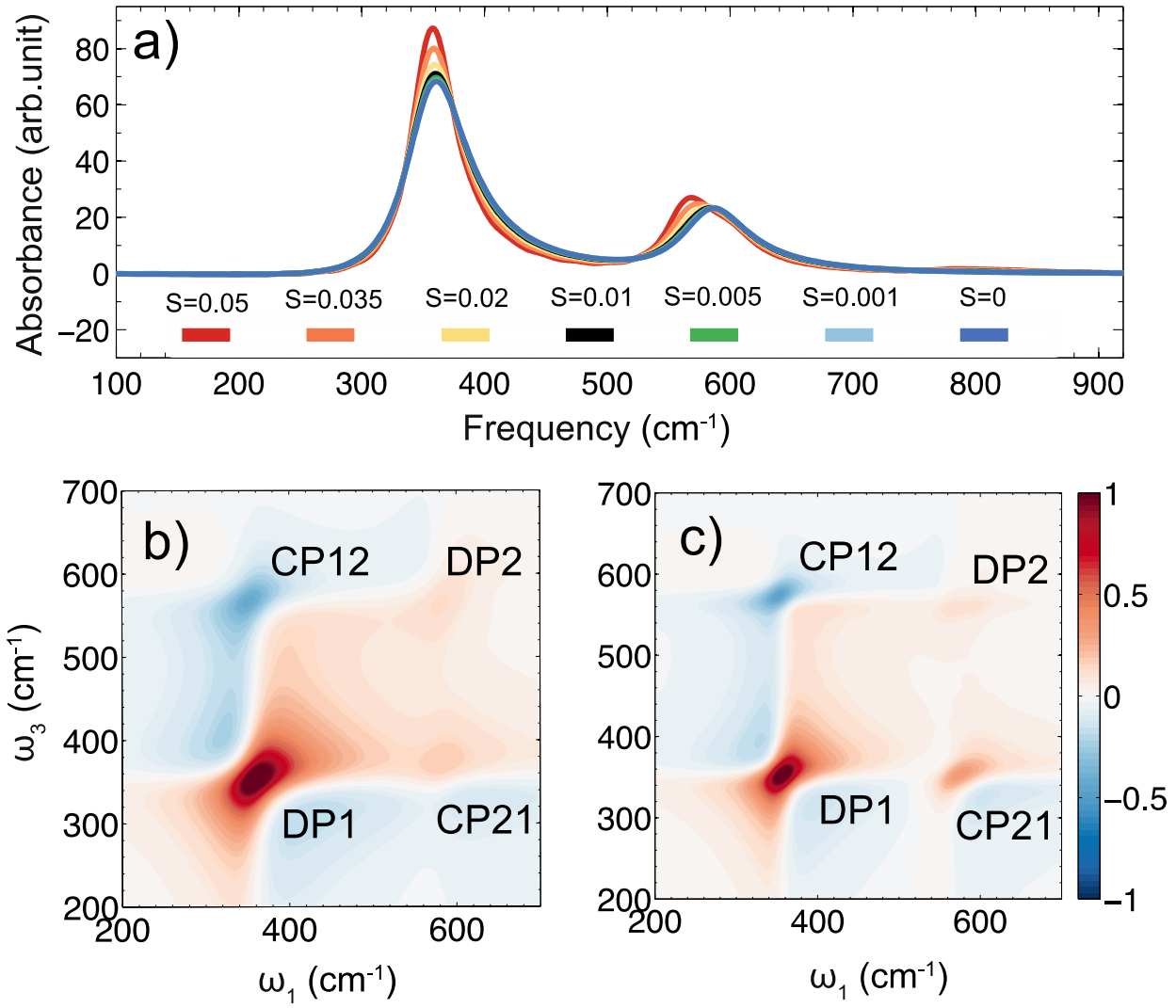

Figure 2.2 (a) Simulated linear absorption spectra for various S and constant Stokes shift, so that $\lambda_{\text{env}} - S\omega_{\text{vib}} = 35\ \text{cm}^{-1}$. The lower (higher) frequency peak shows absorption into $|e_0\rangle$ (overlapping states $|e_1^{\pm}\rangle$). The correction made to λ_{env} with increasing S prevents strong S-dependence in the linear absorption. Bottom panels: Real part of the simulated rephasing 2D spectra at t_2 = 0 fs and 77 K with (b) S = 0 and λ_{env} = 35 cm^{-1} and (c) S = 0.05, $\omega_{\text{vib}} = \Delta$= 223 cm^{-1}, and λ_{env} = 35 cm^{-1}– $S\omega_{\text{vib}}$ = 23.8 cm^{-1} . The color scales on the 2D spectra are normalized by their respective maxima.

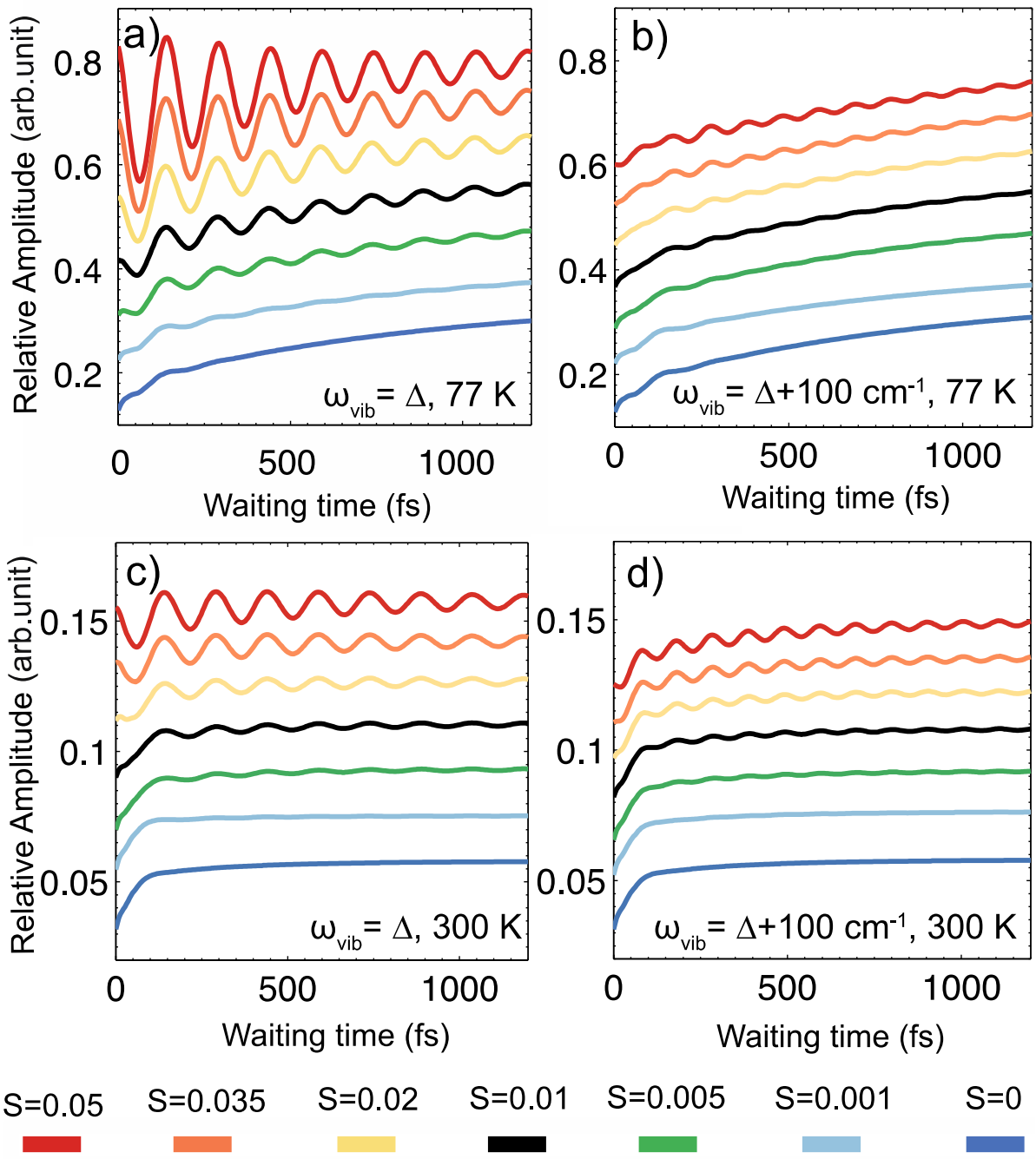

Figure 2.3 Simulated absorptive rephasing 2D-ES cross-peak amplitude (CP21) along waiting time t_2, for various S and with (a) $\omega_{vib} = \Delta$ and (b) $\omega_{vib} = \Delta + 100$ cm^{-1} at 77 K; with (c) $\omega_{vib} = \Delta$ and (d) $\omega_{vib} = \Delta + 100$ cm^{-1} at 300 K. The relative amplitude unit for each choice of S is normalized by the maximum of the respective absorptive rephasing spectrum at $t_2 = 0$ fs; the traces have been vertically offset for clarity, by a constant equal to (a) and (b) 0.1 and (c) and (d) 0.02.

Figure 2.2b and c show simulated rephasing 2D spectra at 77 K and $t_2 = 0$ fs for $S = 0$ and $S = 0.05$. Measured over t_2, the diagonal peaks DP1 and DP2 show the population dynamics in states $|e_0\rangle$ and $|e_1^{\pm}\rangle$ respectively (see Figure 1.1). Oscillations arising from electronic coherence are expected to appear in the lower cross-peak, CP21, and the growth of this cross-peak indicates the energy relaxation from upper to lower electronic excitons. While the shape of DP2 and CP21 changes with S, the peak positions remain the same. Vibrational dynamics are expected to contribute to both the diagonal and the cross-peaks. Due to the rapid environmental reorganization ($\sim$50 fs) and weak electronic coupling ($J_{12} = -50$ cm^{-1}), we expect minimal electronic coherence oscillations in the absence of electronic-vibrational coupling. We calculated the waiting time dynamics of 2D spectra for resonant and non-resonant vibration scenarios at 77 K and 300 K. Figure 2.3 displays the amplitude of CP21 as a function of t_2, with ω_1 and ω_2 taken from the maxima along a diagonal cut through DP2 and DP1 (respectively) at t_2 = 0 fs. Oscillations appear in addition to an exponential rise. For $\omega_{\text{vib}} = \Delta$ at 77 K (Figure 2.3a) and $S = 0.01$ (black line), the cross-peak oscillates by about 2% of the t_2 = 0 fs spectrum maximum even after 1 ps; oscillations of about 1% persist for $t_2 > 1$ ps when the Huang-Rhys factor is as small as $S = 0.005$ (green line). For comparison, in the case of $S = 0.05$ (red line), the oscillation remaining after 1 ps has an amplitude of about 5% of the t_2 = 0 fs spectrum maximum.

Ishizaki and coworkers showed that oscillations such as these originate from dynamics in both the ground and excited electronic manifolds [65]. They suggested that the short-term ($t_2 <$ 300 fs) oscillations are due to the electronic coherence, while the late-time oscillation is due to vibrational wavepackets, created via the vibronic states $|e_1^{\pm}\rangle$. It is the resonance between $|\phi_{1g}\rangle|\chi_{g0}^1\rangle \leftrightarrow |\phi_{1e}\rangle|\chi_{e0}^1\rangle$ and $|\phi_{2g}\rangle|\chi_{g0}^2\rangle \leftrightarrow |\phi_{2e}\rangle|\chi_{e1}^2\rangle$ that creates the $|e_1^{\pm}\rangle$ states. The transition dipoles for $|g\rangle \leftrightarrow |e_1^{\pm}\rangle$ are stronger than for $|\phi_{2g}\rangle|\chi_{g0}^2\rangle \rightarrow |\phi_{2e}\rangle|\chi_{e1}^2\rangle$, due to mixing with the pure electronic transition [73]. Therefore the amplitudes of oscillations in Figure 2.3 should depend on this resonance. Figure 2.3b shows the cross-peak dynamics when $\omega_{\text{vib}} = \Delta +$ 100 cm^{-1}. The oscillatory components of the signals are indeed significantly weaker than in the on-resonance case shown in Figure 2.3a, with amplitudes only nearing 1% of the spectrum maximum for $S = 0.05$ at 77 K.

The simulations at 77K indicate that, depending on the experimental signal-to-noise ratio, we expect that the low-frequency intra-pigment vibrations may easily impact waiting time oscillations, despite very small Huang-Rhys factors. Moreover, the very strongest intramolecular vibrations in BChl ($S = 0.05$) may influence the 77 K 2D spectrum even if the frequency is relatively far from resonant with the PPC electronic energy gap. However, as was found for the case of $S = 0.025$ examined in Ref. [65], the contribution of electronic-vibrational mixing to waiting time oscillations in 2D-ES is extremely sensitive to temperature. Figure 2.3c and d show cross-peak dynamics simulated at 300 K. Noting the changes in the vertical scale, oscillations at 300 K remain long-lived but have much smaller amplitudes. In the case of $\omega_{\text{vib}} = \Delta$ and $S =$ 0.05, oscillations of about 0.5% of the t_2 = 0 fs spectrum maximum persist after 1 ps at at 300 K. This calculation supports the claim that, owing to the small Huang-Rhys factors and the influence of the environment, oscillations due to intramolecular vibrational coherence are small, and unlikely to be detected in weakly coupled Chl and BChl complexes at physiological temperature.

Kreisbeck *et al.* [47] used a short-time Fourier transform to analyze 2D spectra simulated with a spectral density extracted from experiments studying FMO [61]. They found that the

oscillation frequency shifted from the electronic energy gap to vibrational frequencies over the waiting time, and used this to distinguish between the different origins of oscillation. To further clarify our analysis, we also examine the differences between oscillations appearing at early (t_2 = 0 to 400 fs) and late (t_2 = 400 to 800 fs) waiting times. Figure 2.4 shows time-windowed Fourier transforms of cross-peak traces in Figure 2.3b and c, where $\omega_{vib} = \Delta + 100$ cm^{-1}. We have used a moving-average filter to partially remove the slow exponential rise and then transformed 400 fs segments of the waiting time oscillations.

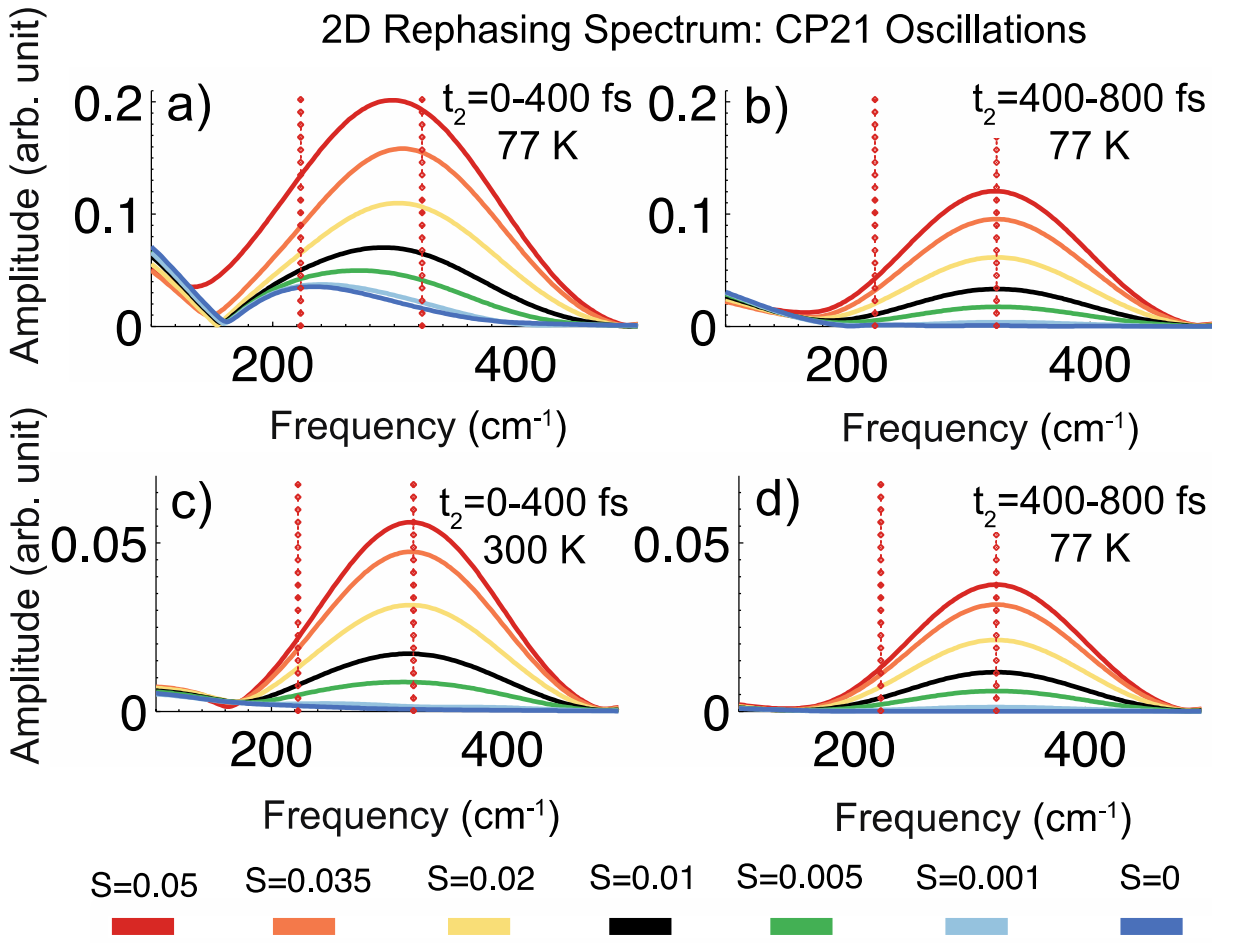

Figure 2.4 Time-windowed Fourier transforms of the 2D-ES cross-peak amplitudes, shown in Figure 2.3c and d, along t_2, for various S and with $\omega_{vib} = \Delta + 100$ cm^{-1}, for waiting times (a) 0 fs $\leq t_2 \leq$ 400 fs and (b) 400 fs $\leq t_2 \leq$ 800 fs at 77 K, and for waiting times (c) 0 fs $\leq t_2 \leq$ 400 fs and (d) 400 fs $\leq t_2 \leq$ 800 fs at 300 K. The dotted lines indicate the electronic energy gap frequency, Δ = 223.6 cm^{-1}, and the vibrational frequency, ω_{vib} = 323.6 cm^{-1}. Note the changes in scale between panels. A moving-average filter was used to partially remove the exponential rise in the time-domain data, and a tapered cosine window was applied to 400 fs segments of the resulting waiting time oscillations.

The resulting frequency-domain peak is especially broad due to the short t_2 window, and the pure electronic oscillations ($S = 0$, dark blue line) are broad due to the rapid environmental reorganization ($\gamma_{\text{env}} = 50$ fs). Nonetheless, the 100 cm^{-1} detuning of the vibration from the electronic energy gap is enough to distinguish the two frequencies in the t_2 oscillations (red dashed lines). Late-time oscillations appear at the vibrational frequency, for any $S > 0$ and at both 77 K (Figure 2.4b) and 300 K (Figure 2.4d); this supports ascribing them to vibrational wavepackets. The 300 K late-time oscillations are $\sim 70\%$ weaker than at 77 K, which again demonstrates the reduced electronic-vibrational mixing in the presence of strong fluctuations. Early-time oscillations at 300 K (Figure 2.4c) also match the vibrational frequency. These physiological-temperature vibrational oscillations are likely too weak to be observed experimentally. Nonetheless, we can observe from the simulations that in this weakly coupled dimer, with rapid environmental reorganization even the weakest of vibrations have more influence than electronic coherence at 300 K. It is only at 77 K (Fig. 4a) and $S = 0$ (dark blue line) that the frequency of the early-time oscillation matches the electronic energy gap Δ, and the frequency tends strongly toward ω_{vib} as S increases.Given that in the FMO complex many low-frequency vibrations have been measured with $S \sim 0.01$, we take note that in Figure 2.4 the simulation with $S = 0.01$ (black line) yielded a waiting time oscillation frequency midway between Δ and ω_{vib}. This suggests that, for BChls 3 and 4 in FMO, the influence of the numerous low-frequency vibrations may be of a similar magnitude to the purely electronic oscillations observable at 77 K, even at early waiting times.

The purely vibrational effects in complexes with weak electronic coupling and small Huang-Rhys factors are extremely difficult to identify using 2D spectra alone. Although 2D Fourier maps of the waiting time oscillations have recently been used to assign a mixed character to coherences in the PSII reaction center [19] (where the electronic coupling is large), in the case of weak electronic coupling and small Huang-Rhys factor, vibrational and electronic Fourier map patterns were not distinguishable [43]. Polarization-controlled 2D-ES is a promising experimental solution, and has already been applied to distinguish vibrational and electronic coherences in the bacterial reaction center [18]. However, the polarization-control method is limited by its critical dependence on relative electronic transition dipole orientations.

2.4.2 Comparison to the Site-Probe Response

When the vibrational and electronic character coherences are not distinguishable, the correspondence between oscillations in 2D spectra and inter-site coherence becomes unclear. A better measure of inter-site coherence would probe the correlation between absorptions and later excitation population at a specific pigment, as in Equation 2.10. This "site-probe response" is intended as a useful benchmark for evaluating the correspondence between 2D-ES oscillations and underlying inter-site coherence in different model dimers. The site-probe response is insensitive to purely vibrational dynamics, because the nuclear DOFs are traced over at the end of the waiting time. The only DOF measured is the single excitation localized on pigment m, ensuring that the site-probe response manifests oscillations due to excited-state coherence between pigment sites. By comparing the oscillations in the simulated 2D spectra (Equation 2.7) with the site-probe response measurement, we can definitively distinguish between localized vibrational wavepackets and inter-site electronic or vibronic coherences in our simulations.

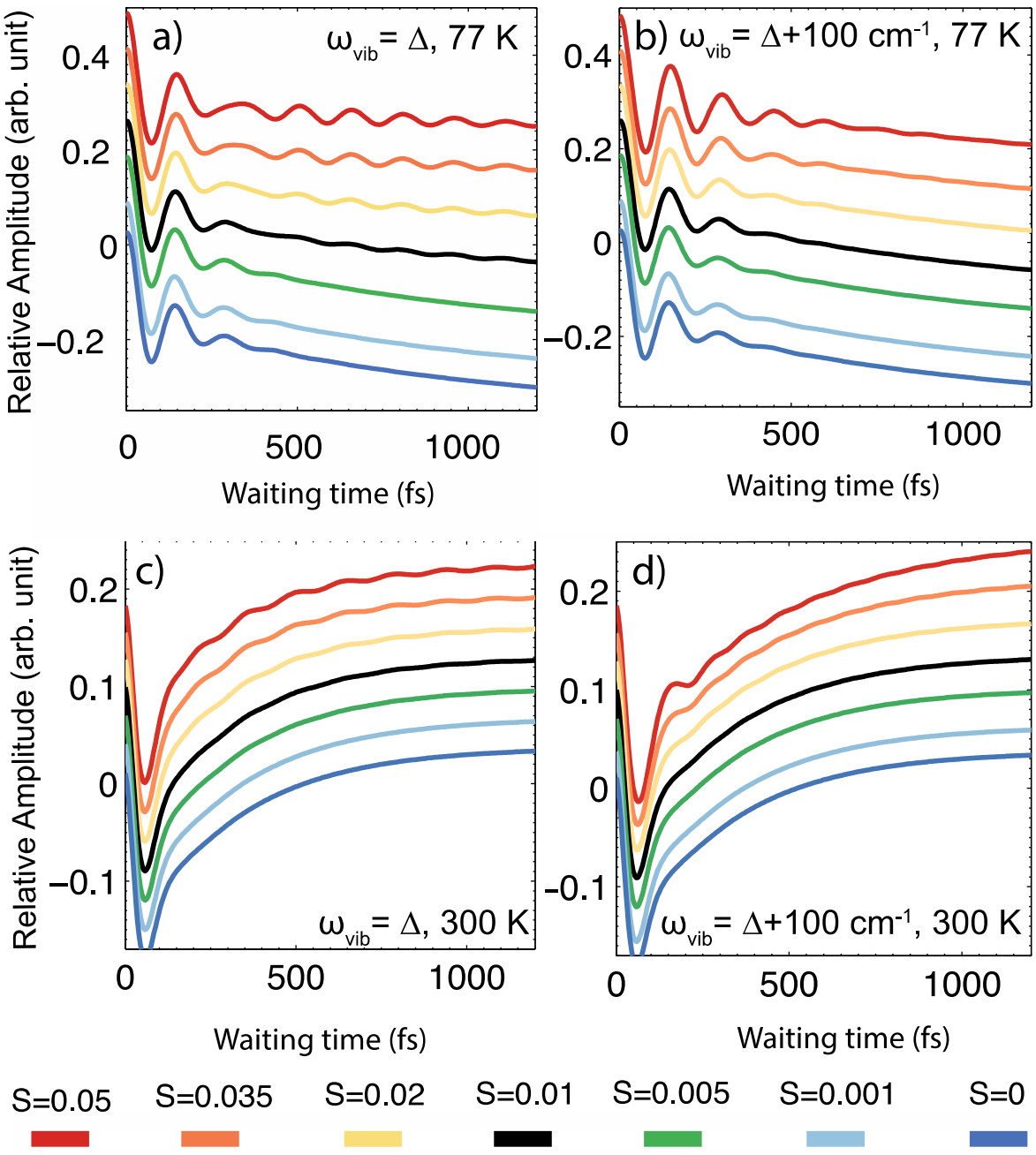

Figure 2.5 Real portion of the donor site-probe response to excitation at the upper exciton (see Equation 2.10), along waiting time t_2, for various S and with (a) $\omega_{vib} = \Delta$ and (b) $\omega_{vib} = \Delta + 100$ cm^{-1} at 77 K; with (c) $\omega_{vib} = \Delta$ and (d) $\omega_{vib} = \Delta + 100$ cm^{-1} at 300 K. The relative amplitude unit for each choice of S is normalized by the maximum of the respective Re$[S_1(\omega_1, t_2)]$ at $t_2 = 0$ fs. Traces are at a constant pump frequency ω_1, chosen from the DP2 feature in the simulated 2D-ES; they have been vertically offset for clarity, by a constant equal to (a) and (b) 0.06 and (c) and (d) 0.03.

In Figure 2.5 we display the results of the site-probe response calculation for $\omega_{\text{vib}} = \Delta$ and $\omega_{\text{vib}} = \Delta + 100$ cm^{-1} at 77 K and also at 300 K. The optical pump frequency ω_1 was selected to match the DP2 feature in the 2D-ES, and the probe is at the donor site ($m = 1$ in Equation 2.10). Initially, the donor site-probe response becomes increasingly negative with t_2, because pumping $|e_1^{\pm}\rangle$ is positively correlated with population transfer from the donor to the acceptor (note that traces in each panel have been vertically offset for clarity). As was observed in the 2D-ES simulations, the amplitude of oscillations in the site-probe response increases with S, and is also enhanced by the resonance, $\omega_{\text{vib}} = \Delta$. Comparing Figure 2.3a and Figure 2.5a, we observe that for $S \leq 0.02$, oscillation amplitudes are significantly more robust in the 2D spectrum than in the site-probe response.

This same observation can be made from Figure 2.3b and Figure 2.5b: while in the 2D-ES measurement the amplitude of late-time oscillations increases steadily with increasing S, site-probe response oscillations are relatively insensitive to the vibration for $S \leq 0.02$. Oscillations that, with increased S, appear in the 2D spectrum but not in the site-probe response must arise from vibrational wavepackets (both on the ground electronic state and localized on a single pigment in the excited state). The comparison between Figure 2.3 and Figure 2.5 confirms that in our simulations, the 2D-ES late-time oscillations at 77 K do not correspond to coherence between sites. Similarly for $\omega_{\text{vib}} = \Delta + 100$ cm^{-1}, Figure 2.3b shows late-time oscillations that are nearly absent in and Figure 2.5b, for all $S \leq 0.05$. Detuning the vibrational frequency prevents sufficient mixing for long-lived vibronic delocalization, so that when $\omega_{\text{vib}} = \Delta + 100$ cm^{-1}, the late-time oscillations in the 2D spectra are vibrational in nature. Examining the results for $S > 0.02$ in Figure 2.5a, we observe that increasing the vibronic coupling prolongs the lifetime of site-probe response oscillations, which implies a delay in irreversible decoherence and excitation localization. Since the Franck-Condon factor that weights the coupling between $|\phi_{1e}\rangle|\chi_{e0}^1\rangle$ and $|\phi_{2e}\rangle|\chi_{e1}^2\rangle$ scales as $\sqrt{S}$ for $S \ll 1$, a larger S produces stronger vibronic mixing and more delocalized $|e_1^{\pm}\rangle$ states. The vibrational relaxation in this model is slow, so that coherences with more mixed character vibronic coherence persist for longer. Our simulation indicates that the Franck-Condon factor of 0.05 ($S \approx 0.056$) measured for a 192 cm^{-1} mode in BChl may be large enough to induce long-lived vibronic delocalization effects in PPCs with a near-resonant electronic energy gap, albeit only at low temperature (see Figure 2.5c).

For $S = 0.05$ (red line) in Figure 2.5a, the site-probe oscillation shows clear early- and late-time components, with close to a π difference in phase. We find that early- and late-time components do not fit well to a sum of exponential sinusoids. Instead, we used the form

$$a_0 + \sum_{i=1}^{2} a_i\, e^{-t/\tau_i} + a_3 e^{-t/\tau_3}\cos(\omega t + \phi) + a_4 e^{-t/\tau_4}\cos(\omega' t + \phi')\sigma(t)$$

Equation 2.11

where $\sigma(t) = [1 + e^{-k(t-t_0)}]^{-1}$ is a logistic function that determines the amplitude and arrival timing for the late-time component. A least-squares fit of the $S = 0.05$ site-probe response trace in Figure 2.5a was obtained with coefficient of determination [74] $R^2 = 0.9988$. The early oscillatory component with $\omega = 223.5$ cm^{-1}decays with $\tau_3 = 145$ fs. The late-time oscillatory component turns on after $\tau_0 = 261$ fs, with $\omega' = 222.3$ cm^{-1} and decay time $\tau_4 = 665$ fs. The phase difference $\phi - \phi'$ between the components is 190°. This form suggests that the site-probe response dynamics result from two distinct processes. The two oscillation decay timescales both

fall between the environmental reorganization time ($\gamma_{\text{env}}^{-1} = 50$ fs) and the vibrational dephasing time ($\gamma_{\text{vib}}^{-1} = 2$ ps) ,which implies a mixed-character vibronic origin for both components.

If it seems in Figure 2.5b Fig. 5b that increasing S prolongs the lifetime of oscillations, when $\omega_{\text{vib}} = \Delta + 100$ cm^{-1}, we must interpret the simulation carefully. These longer lifetimes are due in part to the adjustment in the overdamped environmental reorganization energy, $\lambda_{\text{total}} = \lambda_{\text{env}} - S\omega_{\text{vib}} = 35$ cm^{-1}. While this adjustment preserves the total amount of dissipation despite an increase in S, in order to do so it must decrease the spectral density at $\omega \neq \omega_{\text{vib}}$. This will cause an increase with S in the lifetime of oscillations with frequencies far from ω_{vib}. Nonetheless, the difference between the results in Figure 2.5a and b indicates that this trivial dependence cannot be the only influence of the Huang-Rhys factor on the site-probe response and dynamical localization.

Figure 2.6 shows the time-windowed Fourier transforms of the site-probe response traces. As in Figure 2.4, the left hand panels show the oscillation frequencies for the waiting time period $t_2 \leq 400$ fs, while the right hand panels show frequencies for 400 fs $\leq t_2 \leq$ 800 fs. In Figs. 2.6a and 2.6b the site-probe response oscillates at the energy gap Δ, not at ω_{vib} as seen in the 2D spectrum. We attribute this site-probe oscillation to the evolution of the $|e_1^{\pm}\rangle\langle e_0|$ electronic coherence. At 300 K (Figure 2.6b and c), very small amplitude site-probe oscillations instead appear near ω_{vib}. These are explained by the minimal amount of inter-site coherence oscillation associated with the vibrational wavepacket, when there is a small amount of residual vibronic mixing. By comparing the frequency content of the site-probe response and the 2D-ES cross-peak oscillations, it is clear that at 77 K the 2D-ES oscillations (for the relatively weak couplings considered here) dominantly originate from electronic coherence only for systems with *very* weakly coupled vibrations, $S < 0.005$.

In all of the simulations described here, the majority of the energy transfer is accomplished within the environmental reorganization timescale, $\gamma_{\text{env}}^{-1} = 50$ fs. In the range of small Huang-Rhys factors that we consider, the rate of EET as measured in the calculated responses does not change significantly with increased S. We see this both in the site-probe measurement (Figure 2.5) and also in the initial decays of DP2 in the rephasing spectrum (not shown). This observation agrees with the findings of Ishizaki and coworkers [65]: when both electronic coupling and electron-vibrational coupling are small, although multidimensional spectroscopies remain very sensitive to coherences of all types (vibrational, vibronic, electronic), these coherences have little influence on the overall population transfer dynamics from one site to another via relaxation and energy transfer.

Our strategy of calculating time-dependent correlations between optical pump excitations and subsequent density matrix elements is not limited to probing site populations. To more clearly visualize the effect of vibrations on site-site entanglement and exciton delocalization, we calculate a quantity which we call the "concurrence-probe response". Concurrence (C) is a widely used measure of entanglement between a pair of qubits [75], [76]. For a coupled dimer in which excitation is completely delocalized over the two sites, $C = 1$; for a localized excitation, $C = 0$. After two interactions with the laser field, the reduced density operator $\rho_{\text{exc}}(t)$ has an "X-structure"[77], so that the concurrence in the single excitation manifold conveniently reduces to [78]

$$C(t) = \text{Tr}[|1\rangle\langle 2|\rho_{\text{exc}}(t)]$$

Equation 2.12

Hence, similarly to Equation 2.10, we can construct

$$C_{12}(\omega_1, t_2) = 2i^2 \int_0^\infty dt_1 e^{i\omega_1 t} \ \mathrm{Tr}[|1\rangle\langle 2|\mathcal{G}(t_2)\,\mu^{\times}_{\rightarrow}\mathcal{G}(t_1)\mu^{\times}_{\leftarrow}\rho_{\mathrm{exc}}(-\infty)]$$

Equation 2.13

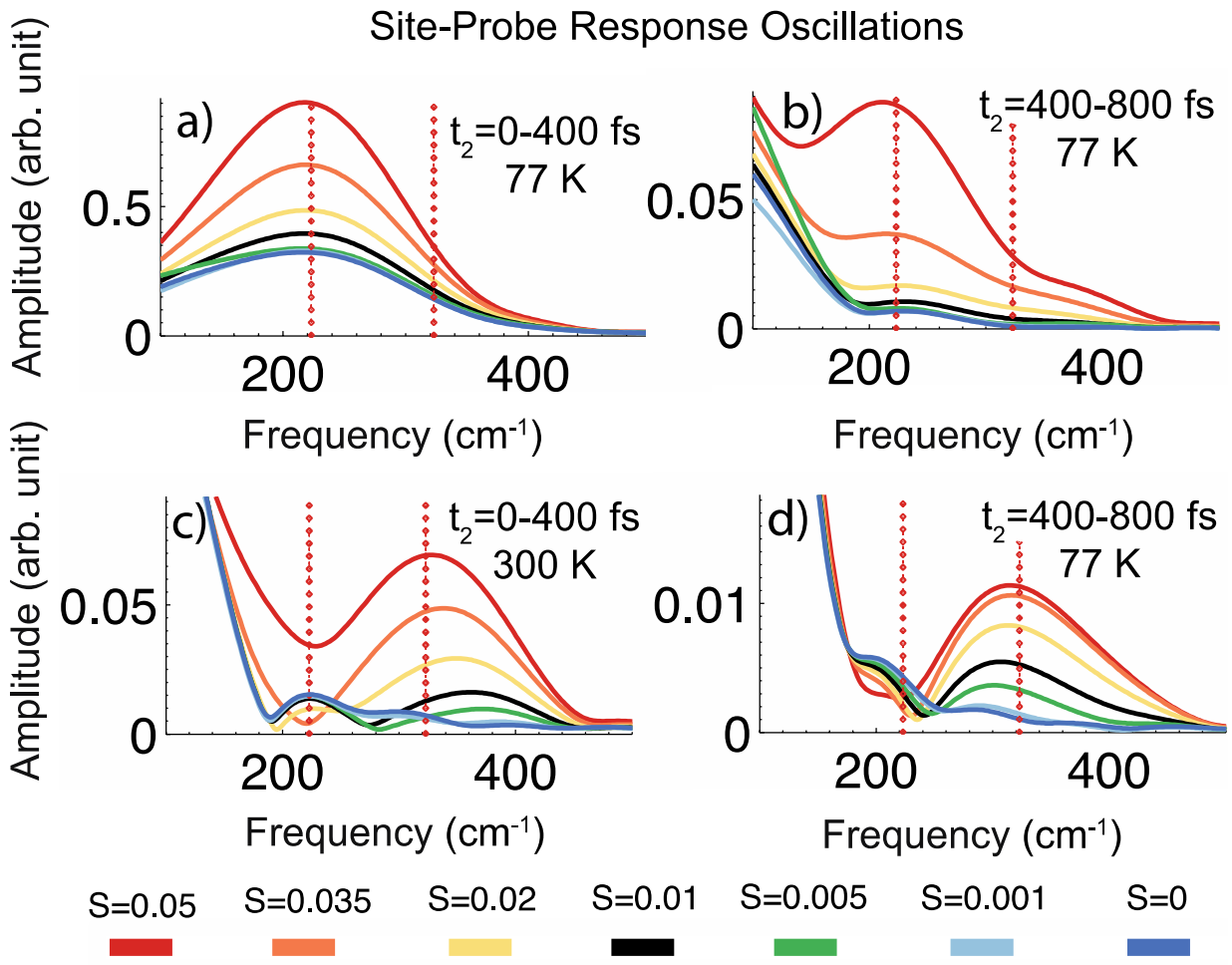

Figure 2.6 Time-windowed Fourier transforms of the donor site-probe response to excitation at the upper exciton, shown in Figure 2.5b and d, for various S and with $\omega_{\mathrm{vib}} = \Delta + 100$ cm^{-1}, at 77 K for waiting time (a) 0 fs $\leq t_2 \leq$ 400 fs and (b) 400 fs $\leq t_2 \leq$ 800 fs, and at 300 K for waiting time (c) 0 fs $\leq t_2 \leq$ 400 fs and (d) 400 fs $\leq t_2 \leq$ 800 fs. The dotted lines indicate the electronic energy gap frequency, $\Delta = 223.6$ cm^{-1}, and the vibrational frequency, $\omega_{\mathrm{vib}} = 323.6$ cm^{-1}. Note the changes in amplitude scale between panels. A moving-average filter was used to partially remove the exponential rise in the time-domain data, and a tapered cosine window was applied to 400 fs segments of the resulting waiting time oscillations.

Here the doorway function $\mathcal{D} = \mu_{\rightarrow}^{\times}\mathcal{G}(t_1)\mu_{\leftarrow}^{\times}$ and time-evolution $\mathcal{G}(t_2)$ are identical to those in both the 2D spectrum and site-probe response calculations, but the window function is now taken from Equation 2.12. Figure 2.7 shows waiting time traces of $C_{12}(\omega_1, t_2)$, for $\omega_{vib} = \Delta$ and $\omega_{vib} = \Delta + 100$ cm^{-1}, at 77 K and 300 K.

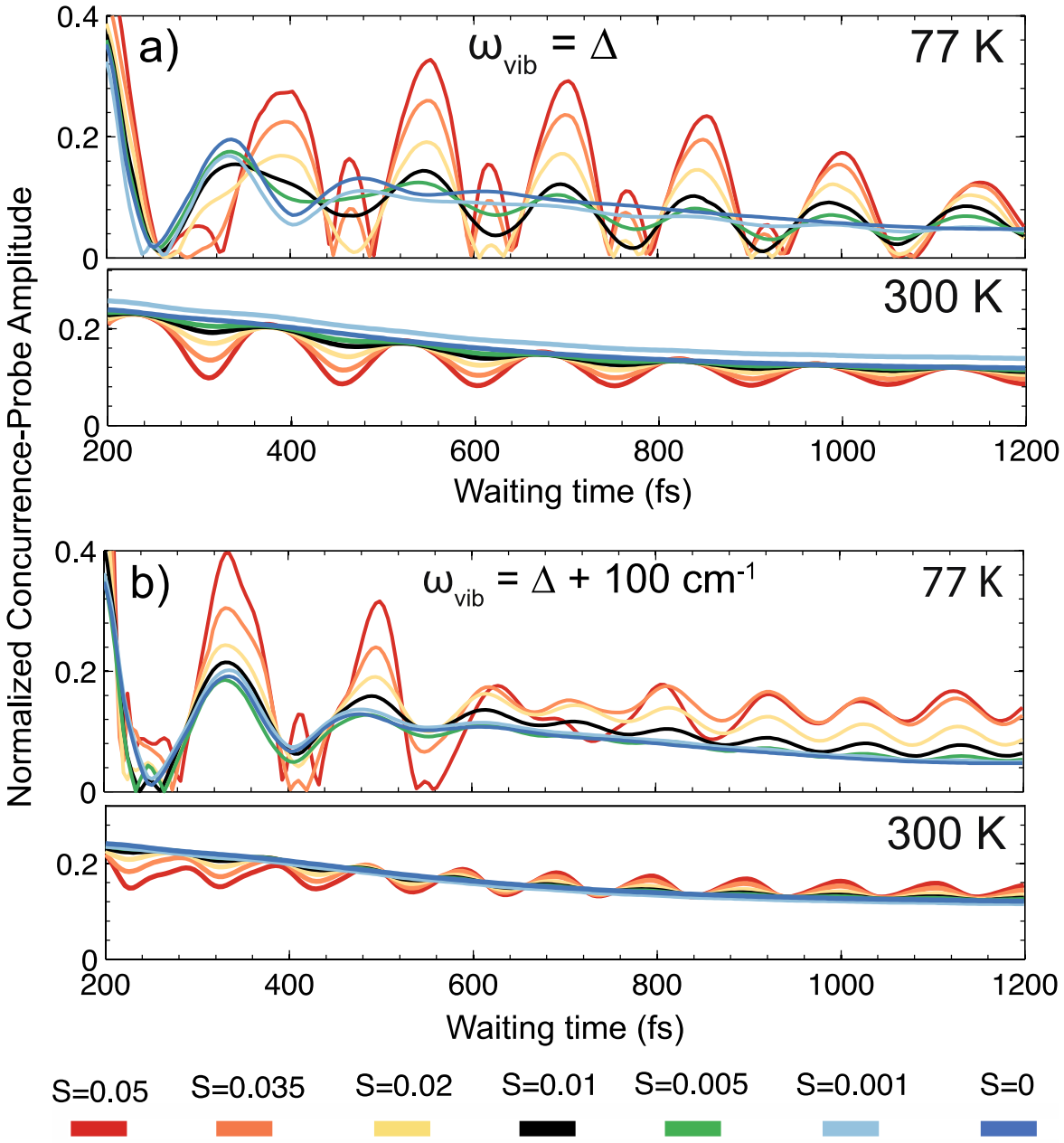

Figure 2.7 Optical-pump, concurrence-probe amplitude (see Equation 2.13) as a function of waiting time t_2, at 77 K and 300 K and for various S with (a) $\omega_{vib} = \Delta$ and (b) $\omega_{vib} = \Delta + 100$ cm^{-1}. Traces are at a constant pump frequency ω_1, chosen from the DP2 feature in the simulated 2D-ES. Each trace is normalized to its respective maximum value.

As with the site-probe response traces in Figure 2.5, the optical pump frequency ω_1 was chosen from the DP2 feature in the 2D-ES. This concurrence-probe response represents the time-dependent correlation between optical pump interactions at the upper exciton frequency and the subsequent amount of entanglement between the two pigment sites.

The low-temperature concurrence-probe response in Figure 2.7 exhibits dramatic extinctions and revivals of the concurrence. Similarly, "entanglement sudden death" and "rebirth" have been observed in the dynamical behavior of open quantum systems [79], [80]; this effect can arise as a consequence of non-Markovianity in the environment [81], [82] and was found to be characteristic of the intermediate-coupling regime [83]. With increasing S in our simulations, the contribution to the environment from the non-Markovian vibration increases relative to that of the overdamped environmental modes; the amplitude of revivals in Figure 2.7 correspondingly increases. The effect of the vibration on the concurrence-probe response is somewhat more robust when $\omega_{\text{vib}} = \Delta$ (Figure 2.7a) than in the off-resonant case (Figure 2.7b). At 300 K (see Figure 2.7c and d), the entanglement revivals are small and much less dependent on S. We find these results in agreement with our analysis of the site-probe response: at 77 K, the S-weighted coupling and near-resonance between $|\phi_{1e}\rangle|\chi^1_{e0}\rangle$ and $|\phi_{2e}\rangle|\chi^2_{e1}\rangle$ creates states that are more resistant to environment- induced localization. When electronic excitation energy localizes, information about the wavefunction at the other site has been irreversibly lost. The concurrence-probe oscillations demonstrate that when the vibrational and electronic DOFs are correlated through mixing, some of that information passes reversibly to the underdamped vibration, and then returns to the electronic system. At 300 K, the environmentally-induced fluctuations are powerful enough to destroy the mixing, and therefore prevent strong revivals from appearing in the concurrence-probe response.

2.5 Concluding Remarks

In order to better understand the effect of very weakly coupled vibrations on 2D electronic spectra and the coherence dynamics they measure, we have simulated 2D spectra of a model heterodimer. Our model incorporates environmental effects and an intra-pigment vibrational mode at each site via a phenomenological form of the relaxation function for the non-equilibrium excitation energy. Crucially, this approach correctly describes the destruction of vibrational-electronic mixing by environmentally induced fluctuations. We have systematically studied the impact of vibrations with very small Huang-Rhys factors, which are typical in photosynthetic pigment-protein complexes. We introduced the "site-probe response," a formalism for effectively comparing simulated 2D-ES waiting time dynamics with the underlying dynamics at specific sites. We show that even the very weak electronic-vibrational interactions common in pigment-protein complexes can significantly affect the oscillations in a multidimensional spectrum so much that localized vibrational wavepackets obscure the underlying inter-site coherence dynamics at 77 K. Our simulations also demonstrate that at 77 K and for a Huang-Rhys factor comparable to the strongest low-frequency vibration in BChl, a vibration 100 cm^{-1} away from resonance with the electronic energy gap produces only localized vibrational coherence oscillations in the 2D spectra at late waiting time but that a near-resonant vibration significantly increases the inter-site coherence and delocalization remaining after 600 fs. However, by comparing simulated 2D spectra with the site-specific response calculation, we find that evidence of this vibronic resonance effect is obscured by the purely vibrational oscillations and is not discernible from the 2D spectrum alone. We confirm that, due to the

fragility of vibronic mixing to the environmentally induced fluctuations, vibronic resonance effects vanish at 300 K.

The contrast between the 2D-ES simulations and the fictional site-probe response measurement simulated here highlights the potential impact of future experiments that access site-specific information, as opposed to the response from delocalized excitonic states, on our understanding of photosynthetic light-harvesting. Like the site-probe response discussed here, such experiments might measure the time-dependent correlation between excitons that are generated via Franck-Condon transitions and the energy subsequently available at a specific pigment. A spatially inhomogeneous observable, such as localized higher electronic states, transition dipole orientations, or intrapigment vibrations, plays the role of the site basis projection. The 2D electronic-vibrational spectroscopy [84]–[86] recently developed in our laboratory, for example, is able to measure the site-probe response — so long as the probed vibration is confined on a single pigment. Such measurements, sensitive to changes in the location of excitation energy, enable a view of energy transfer not just as equilibration between eigenstates but as a flow across nanoscale distance. Besides insensitivity to vibrational wavepackets, such measurements might provide empirical evidence of how local variations in the spectral density [87] affect EET mechanisms. While 2D electronic spectra provide an important measure of energy dynamics in pigment-protein complexes and other molecular aggregates, it should not be neglected that very weakly coupled low-frequency vibrations can easily mitigate the correspondence between long-lived oscillations in 2D spectra and inter-site coherence.

3 Methods for Increased Sensitivity in 2D Electronic Spectroscopy

The 2D-ES experiments in Chapters 4 and 5 are exceptional in part because the solid state materials studied are a highly scattering inhomogenous film and a single atomic layer, respectively. Obtaining good quality spectra from thin or highly scattering samples requires a high signal-to-noise ratio. Several experimental factors are used to control the signal-to-noise in 2D spectroscopy. The laser power should be stable over the time required for the measurement. The alignment, especially the degree of overlap between the local oscillator and the signal, should be robust. Optics should be mounted on pedestal mounts as opposed to ordinary posts. However, for experiments in the background-free geometry, the most important contribution to noise is the large amount of laser light from either the pump beams or probe that can be scattered into the phase-matched direction. The experiments in this thesis were achieved after implementing a simple but important rapid scatter subtraction protocol. And, as discussed below, careful signal processing can further reduce noise and artifacts. Finally, although it has proved somewhat impractical, detecting fluorescence instead of absorption can radically reduce the influence of scatter on 2D spectra.

3.1 Signal Processing and Time-Domain Windowing

In their original paper describing the 2D-ES apparatus [66], Brixner et al. describe in detail a general data processing procedure which continues to be used in our lab (see Appendix A: MATLAB Code for 2D-ES Signal Processingfor an example of the MATLAB code used to produce the 2D spectra presented in Chapters 4 and 5). For weak signal and scattering samples, the heterodyne detection method is especially important because we are able to control and measure the delay t_{34} between the local oscillator and the signal. This delay is manifested as fringes in the spectral interferogram measured on the CCD pixel array. When transformed into the time domain, the signal can then be windowed around $t=t_{34}$. This selects the signal emitted after the probe arrives and removes contributions from scattered pump beams. Larger values of t_{34} give denser interference fringes, so that the upper bound on t_{34} is given by the resolution of the grating in the spectrometer. It can be controlled by inserting thin coverslip glass into the local oscillator beam path, slightly angled to avoid the incidence of back-reflections.

When relying on time-domain filtering of the heterodyned signal for scatter subtraction, there is an important artifact to remember. Extreme spikes in scatter intensity can appear at waiting times $T = 0$ and $T = 2t_{34}$. It is at these two waiting times that $t_{14} = t_{24} = t_{34}$, and time-domain window cannot remove the interference of scattered pump beams with the local oscillator beam 4.

3.2 Rapid Scatter Subtraction Using Choppers and a Microcontroller

To improve the signal to noise of 2D-ES measurements on thin and highly scattering samples, we implemented rapid scatter subtraction using choppers and a microcontroller as described in the section below.

Spectrometers and cameras are used in ultrafast spectroscopy to achieve high resolution in both time and frequency domains. Frequency-resolved signals from the camera pixels cannot be processed by common lock-in amplifiers, which have only a limited number of input channels. Here we demonstrate a rapid and economical method that achieves the function of a lock-in amplifier using mechanical choppers and a programmable microcontroller. We demonstrate the method's effectiveness by performing a frequency-resolved pump-probe measurement on the dye Nile Blue in solution.

3.2.1 Introduction

In a pump-probe experiment, a single-channel photodiode may be used to measure the intensity of the signal field heterodyned with the probe field. In order to remove the effects of environmental background noise, as well as portions of the pump beam scattered into the detector, the pump or both the pump and the probe are usually modulated by mechanical choppers, acoustic-optic or electro-optic modulators. The resulting signal then appears modulated at a frequency which depends on the modulating scheme employed. The modulation signal is provided as the reference input to a lock-in amplifier, which takes the photodiode output and extracts the amplitude and the phase (relative to the reference) of the signal appearing at the reference frequency. This signal processing method is most useful in experiments where the probe is narrowband around a single wavelength and only optical transitions near this wavelength are of interest. One such example is the use of time-domain thermoreflectance to measure thermal properties, which usually involves probing at a single wavelength [89]–[91].

However, when frequency resolution within a broad spectrum is required, as when there are multiple optical transitions of interest, detection by a single-channel photodiode is not ideal. Of course, a monochromator or bandpass filters can be used to select a narrowband probe at a certain wavelength, and photodiode-detected experiments can be repeated at each wavelength. This method is, however, time- consuming. A better solution is to resolve the whole spectrum of the signal heterodyned with the probe using a spectrometer with a camera. In this strategy, different frequency components in the heterodyned signal are dispersed inside the spectrometer onto different pixels of the camera and frequency-resolved with high resolution.

Unfortunately, common cameras offer no hardware access to signals on individual pixels. Besides, common commercial lock-in amplifiers have only a limited number of input channels (less than 10), so that there is no way to process the signal from every pixel by a lock-in

amplifier. Therefore, there is a need for an alternative device and accompanying algorithm which together function like a lock-in amplifier. One simple solution is to use shutters to modulate the beams, just like slow choppers except that the user actively controls their opening and closing. The signals with shutters open and closed are collected, and numerically manipulated to extract the material response and remove noise [92], [93]. This solution suffers from the limited lifetime of mechanical shutters, and especially from low efficiency since shutters take several milliseconds or longer to open or close, during which several pulses are wasted for laser systems with repetition rates at 1 kHz or greater. For improved efficiency, faster methods have been proposed [94], [95] which use choppers and a voltage acquisition board, such as a National Instruments (NI) DAQ, to passively read the chopper status.

Here we describe and demonstrate the implementation of a rapid data acquisition scheme for ultrafast frequency-resolved spectroscopy similar to that described by Heisler et al. [95] but with a widely available, economical, programmable and compact microcontroller (Arduino Uno). We discuss the implementation in details and compare results of a frequency- resolved pump-probe experiment on Nile Blue, in which the data is acquired by the microcontroller and a CCD (charge-coupled device) camera versus by a photodiode and a lock-in amplifier. We find that our proposed method can achieve good signal-to-noise ratio with sufficient efficiency, despite that it cannot benefit from the sophisticated electronic noise filters of a typical lock-in amplifier.

We demonstrate the proposed data acquisition method by performing degenerate pump-probe measurements. The pump and the probe are of the same color and polarization, so that the noise caused by scattered pump light cannot be removed by bandpass filters nor polarizers. A commercial amplified femtosecond laser (Astrella, Coherent, Inc.) provides pulses centered at 800 nm with 1 kHz repetition rate. The 800 nm light pumps a home-built noncollinear optical parametric amplifier (NOPA), generating pulses in the visible range, which are then used for both the pump and the probe.

3.2.2 Experimental Implementation

Figure 3.1 illustrates the device connection and synchronization scheme. The synchronization and delay generator (SDG) associated with the laser can output transistor-transistor logic (TTL) signals with repetition rates of 1 kHz or integer fractions of 1 kHz, synchronized with the laser pulses. We have configured two SDG channels: one provides a 500 Hz signal to drive two choppers, and the other provides the undivided 1 kHz signal to trigger shot-to-shot acquisition by the CCD. One of the choppers uses one half of the frequency of this signal (i.e. 250 Hz) as its driving frequency, while the other uses 500 Hz undivided. Each chopper is equipped with an optical sensor that detects the wheel's real-time position and generates a 50% duty-cycle TTL as a feedback for frequency and phase stabilization. We monitor this signal to indicate the laser beam status, i.e. blocked or passed, in real time as it is modulated by the chopper. The CCD is configured as has been described by Augulis et al. [94], and to our knowledge common commercial CCD detectors can be similarly configured. Briefly, the acquisition cycle of the CCD is set as 1 ms so that it can be synchronized with the 1 kHz trigger from the SDG and a number of laser pulses can each be captured without pause during the CCD running time. Thus the two choppers and the CCD are all synchronized with the laser and there is a fixed phase relation between the operations of any pair of these devices. During its running time, the CCD in turn provides a burst of TTL pulses, each synchronized with a single

acquisition cycle, i.e. the exposure and the readout of a single frame. As shown in Figure 3.1, the TTL signals from the chopper sensors and the TTL burst signal from the CCD are all connected to the digital pins of the microcontroller, an Arduino Uno board in our implementation.

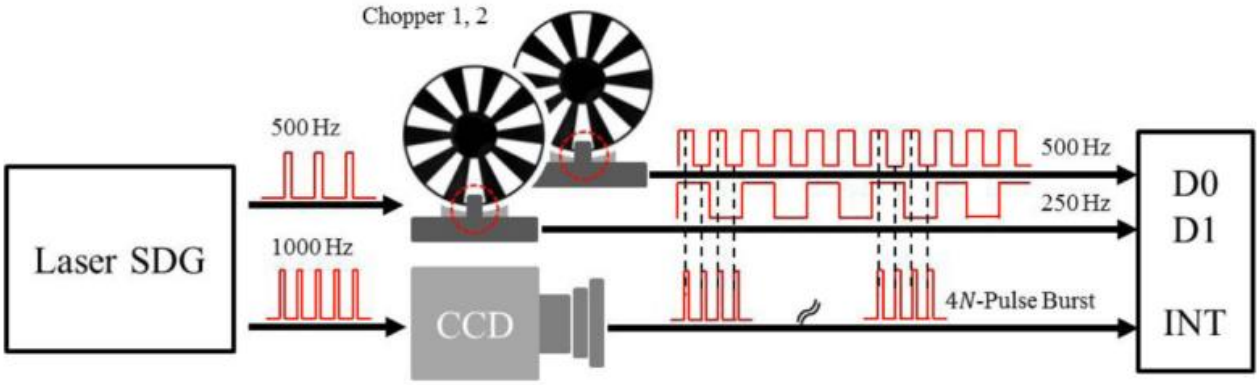

Figure 3.1: Device connection and synchronization scheme. SDG: synchronization and delay generator; D0(1): digital input pin with index 0(1); INT: digital input pin for hardware interrupt. The dashed red circles indicate the positions of the feedback optical sensors on the choppers.

The microcontroller is programmable as an independent computer with analog-to-digital conversion modules. Its function here is to read the status of the choppers at the moment when the CCD acquires a frame. This task is accomplished using a hardware interrupt of the processor on the microcontroller. An interrupt is a signal sent by either hardware or software to notify the processor of an event even while it is running another process. This is a basic function of most microcontrollers. The microprocessor can be programmed such that it will immediately exit the current running code upon receiving an interrupt and enter a sub-routine called the interrupt service routine (ISR). The Arduino Uno has two digital pins capable of accepting external hardware interrupts. We wire one of these to the output from the CCD, which provides the TTL burst synchronized with frame acquisition as shown in Figure 3.1. The microcontroller is programmed so that a voltage rise at the interrupt pin is interpreted as an interrupt event (alternatively, interrupts could be triggered by a voltage fall or change). Therefore, when the CCD is reading a frame, the rising edge of the synchronized pulse is captured by the interrupt pin and the microcontroller switches to the ISR. In the ISR, voltages are read at pins D0 and D1, which are wired to the output from the chopper feedback sensors. The clock speed of an Arduino Uno is 16 MHz, so that it reacts to interrupts within several microseconds, much faster than the chopping periods (4 and 2 ms), which ensures the status is read accurately. Similarly, the laser pulses (as detected on a photodiode), the TTL pulses from the SDG, and the TTL burst pulses from the CCD are all synchronized with a delay much smaller than the chopping periods. Thus, provided that the chopper is correctly phased and its sensor properly aligned, the reading by the microcontroller reflects whether the laser pulses are blocked or passed in real time.

The chopper feedback TTL signal V_f should be low ($V_f = 0$) when a laser pulse is passed and be high ($V_f = 1$) when a laser pulse is blocked (of course this may be reversed, with 0 meaning blocked and 1 meaning passed). This is checked on an oscilloscope by viewing the output of a photodiode placed in the beam path after the chopper, together with the sensor

feedback signal, using the latter as the oscilloscope trigger. Figure 3.2 demonstrates the influence of chopper alignment on the detection of pulse status. The feedback signal is produced by the optical sensor installed on the chopper as shown by dashed red circles in Figure 3.1, and marked as a red dot in Figure 3.2. A beam going through the green dot is passed when the sensor is exposed with $V_f = 1$, while the beam is blocked when the sensor is blocked with $V_f = 0$. For a beam going through the yellow dot, the situation is similar except that the $V_f = 0$ when the pulses are passed. However, if the beam goes through the blue dot, then reading V_f cannot unambiguously detect the pulse status. Care is therefore required when aligning the position of the beam relative to the chopper sensor.

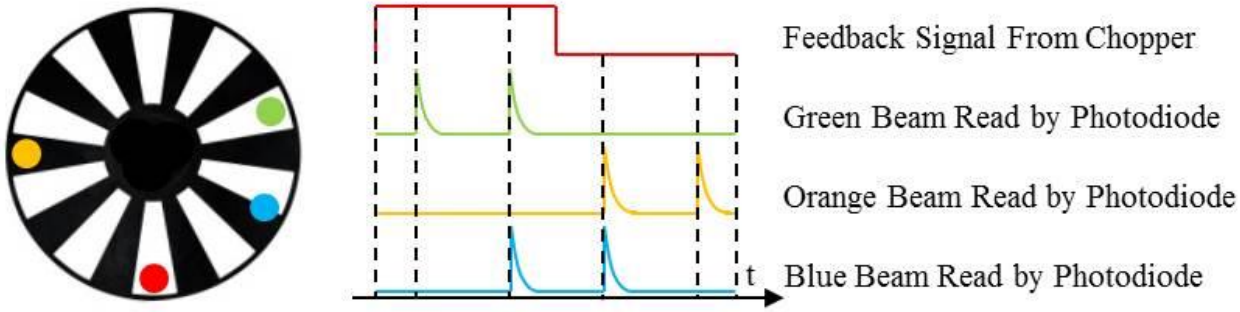

Figure 3.2: Influence of beam alignment on the reading of pulse status, blocked or passed. In this example the laser repetition rate is four times the chopping frequency.

The delay or the phase of the chopper relative to the SDG TTL signal, and thus to the laser pulses, can be easily tuned on the chopper controller front panel. Figure 3.3 shows the well-synchronized readouts of the chopped laser spectrum from the CCD and the pulse status from the microcontroller after configuring the setup as discussed.

During examination of the signal timing as shown on the right side of Figure 3.2, the time scale of the oscilloscope should be on the order of 1 ms/grid to display multiple periods of the feedback signal on the screen. At such scales, the fast response (~1 ns) from the photodiode may not be well captured because common oscilloscopes will reduce the sampling rate automatically when sampling time range is increased. One trick to overcome this issue is to increase the beam power, saturating the photodiode so that the electronic pulses from the photodiode have much longer duration. Another solution is to adjust the input impedance of the oscilloscope, for instance to 1 MΩ.

In our setup, the pulsed laser has a repetition rate of 1 kHz and the two choppers modulate the pump and the probe at 250 Hz and 500 Hz, respectively. With such a design, every four successive frames acquired by the CCD correspond to a sequence of four intensity values: I_{00} for pump on, probe on; I_{01} for pump on, probe off; I_{10} for pump off, probe on; I_{11} for pump off, probe off. The desired signal is then proportional to $I_{00} - I_{01} - I_{10} + I_{11}$. The microcontroller is programmed to digitally read and send the pulse status as 1 or 0 to a computer, which also accepts the frames from the CCD and performs this numerical calculation. For each delay between the pump and the probe, we acquire $4N$ (N is an integer) successive frames and therefore get N data points, which are then averaged for recording. In practice, since the

modulation is perfectly periodic, the microcontroller only needs to read and send the status of the first four frames in any consecutive set.

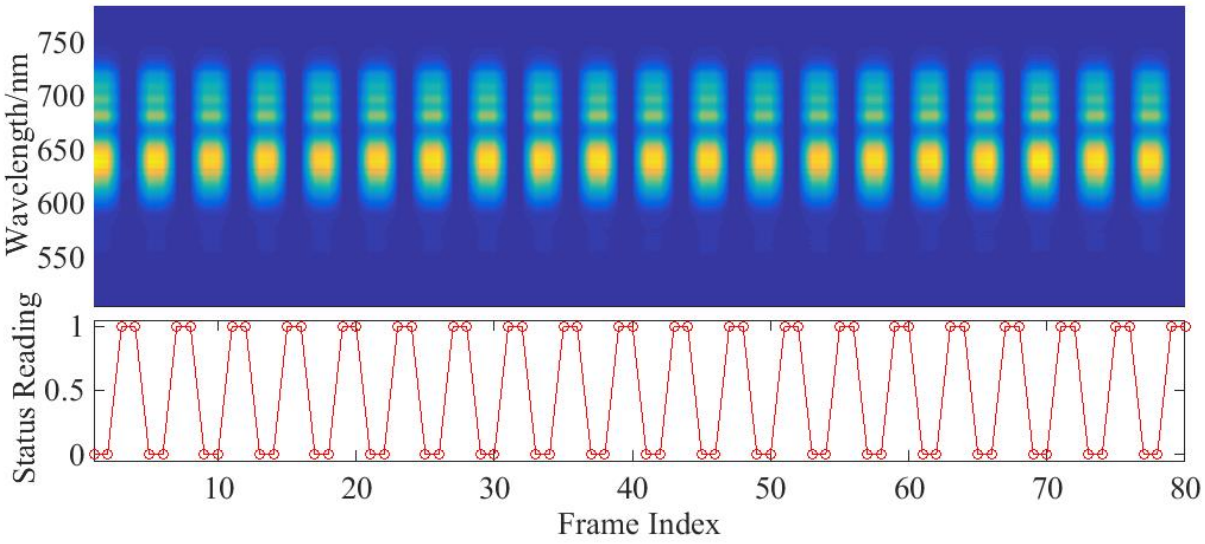

Figure 3.3: 80 frames of synchronized readouts from the CCD and the microcontroller for one chopped beam. The pulsed laser has a repetition rate of 1 kHz and the chopper is working at 250 Hz. The upper plot shows the frequency-resolved intensity detected by the CCD and the lower shows the corresponding chopper status. The chopper sensor is aligned such that the feedback signal is one when the light is blocked.

3.2.3 Demonstration with Pump-Probe Signal

The pump-probe measurements are performed on a solution of Nile Blue dye in ethanol with a concentration of 67 μM contained in a 1 mm-thick cuvette, with a photodiode and lock-in detection and alternatively with a CCD and the proposed data acquisition method. For fair comparison, the experiment setup before the sample is unaltered. The absorption spectrum of the sample and the normalized laser spectrum are shown in Figure 3.4(a) while the normalized autocorrelation trace of the laser pulses is shown in Figure 3.4(b) together with a Gaussian fit, which indicates a pulse duration of 29 fs. The pump fluence is kept at 183 μJ/cm^2.

For lock-in detection, the signal heterodyned with the probe beam propagates through a 40 nm wide bandpass filter centered at 600 nm and is sent into the photodiode (DET210, Thorlabs, Inc.). The pump and the probe are chopped at 357 and 500 Hz respectively with the 7/5 two-frequency chopper wheel. The mixing signal at the sum frequency 857 Hz is used as the lock-in reference. The time constant and sampling rate of the lock-in amplifier are 300 ms and 512 Hz, respectively. Each data point is averaged 80 times, rendering a total time of 8 minutes to acquire 801 data points for 801 delays with step size 6.7 fs, plotted in blue in Figure 3.5(b). For CCD detection, the signal heterodyned with the probe is dispersed by a spectrometer onto the CCD (PIXIS100, Princeton Instruments). As described in the previous section, the pump and the probe are modulated by 250 Hz and 500 Hz respectively. Each data point at a specified pump-probe delay is obtained by taking 200 successive frames with the CCD, averaging by 200/4 = 50 and repeating this process by 8 times for further averaging.

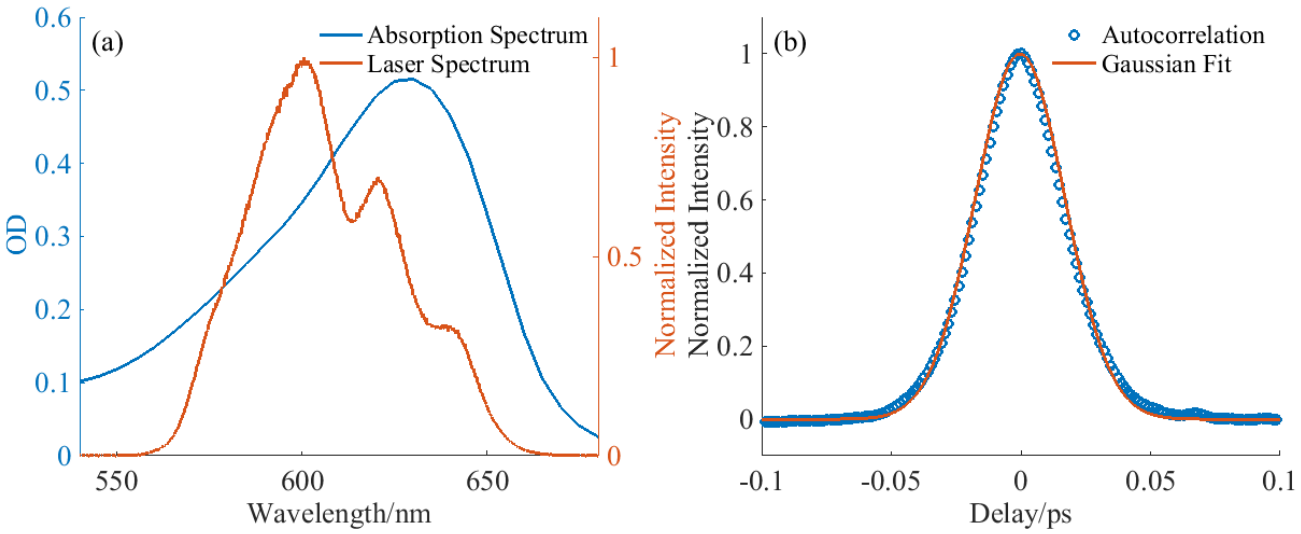

Figure 3.4 (a) Absorption spectrum of Nile Blue in ethanol (left axis) used in the test and the laser spectrum (right axis); (b) Autocorrelation trace of the laser pulse and the Gaussian fit, which indicates a pulse duration of 29 fs.

It takes 104 minutes for acquisition of 801 spectra as shown in Figure 3.5(a). The signals at pixels corresponding to the same spectral range (580 to 620 nm) as in the lock-in detection are summed up and shown in Figure 3.5(b) for comparison with the lock-in detection. These plots feature photo-induced bleaching via the S_0-S_1 vibronic transition in Nile Blue.

Weak oscillations with a period of roughly 60 fs appear in both measurements, which decay within 0.5 ps after excitation and can be attributed to an impulsively excited ring distortion vibrational mode [96]. Because the laser spectrum is narrower than the sample absorption band (Figure 3.4(a)), calculating the relative change of transmission $\Delta T/T$ in the frequency-resolved results leads to artifacts outside the laser spectral coverage. Therefore, in Figure 3.5(a) we show the normalized absolute change of the transmitted probe intensity. For the frequency-integrated curves in Figure 3.5(b), we have divided the signal by the incident probe intensity and plot $\Delta T/T$ normalized to its maximum. The peak signal in Figure 3.5(b) corresponds to $\Delta T/T$ = 20%. The two signals in Figure 3.5(b) show different responses within 500 fs around the maximum probably because the spectra captured in the two strategies are not perfectly identical.

In order to compare the noise levels in the two measurements, 50 successive data points are taken at negative delay after normalization, where there is no sample response. The standard deviation for this noise is 0.0017 for the photodiode and lock-in detection and 0.0019 for the CCD and microcontroller detection. Considering the experimental time cost and noise level, the photodiode and lock-in detection is significantly more efficient if responses at only a few transitions are concerned. This is not surprising since the lock-in amplifier has a sophisticated internal signal-processing apparatus. However, the lower efficiency of the CCD detection is offset by its ability to simultaneously resolve responses from multiple optical transitions.

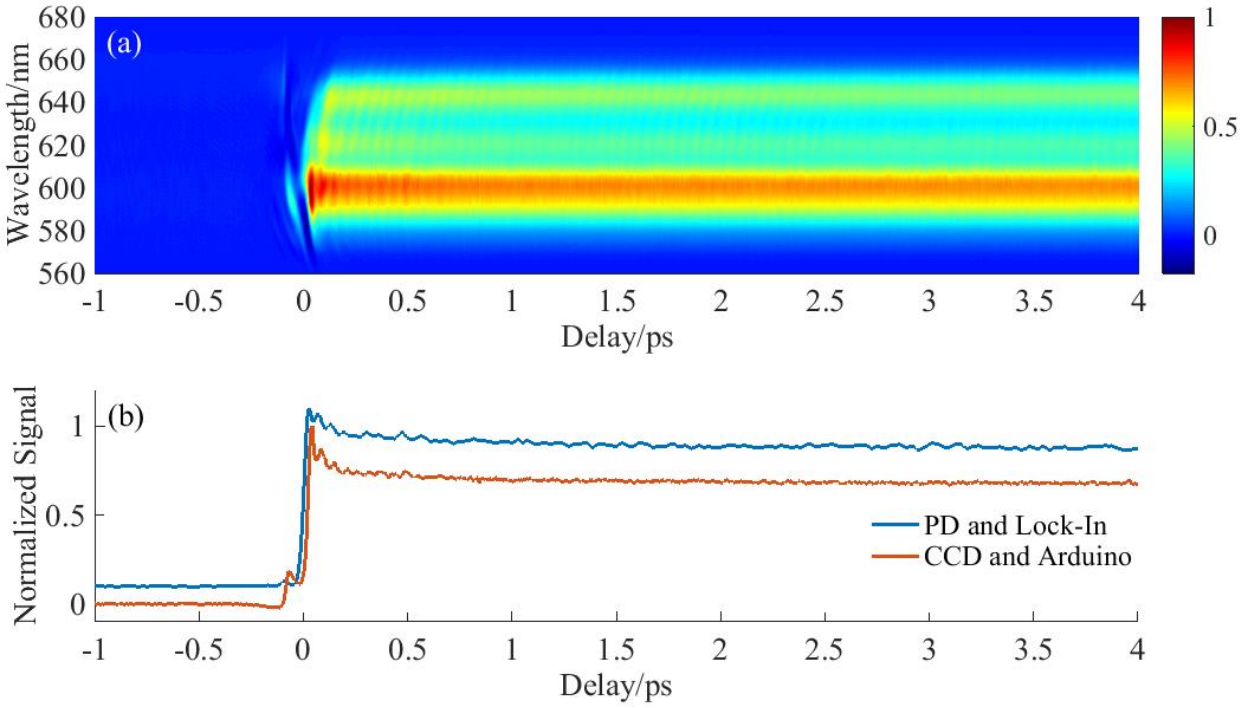

Figure 3.5 (a) Pump-probe measurement results (normalized ΔT) on the solution of Nile Blue dye in ethanol measured by a CCD with the proposed data acquisition method, normalized by the maximum value near 0 ps around 600 nm. (b) Comparison of pump-probe measurement results (normalized $\Delta T/T$) by the two methods: the blue curve indicates the signal measured by a photodiode (PD) with lock-in detection, and is vertically shifted for clarity; the red curve indicates the sum of the frequency-resolved signals from 580 to 620 nm in (a).

We have implemented a rapid data acquisition method for ultrafast frequency-resolved spectroscopy, for which lock-in amplifiers cannot easily be applied. The method is based on a spectrometer with a CCD detector, two choppers and a compact, economical, programmable microcontroller. We demonstrate the performance of this method with pump-probe measurements and compare it with lock-in detection. Although lock-in detection is still preferred when applicable, our method offers commensurate signal-to-noise while measuring all probe frequencies simultaneously, a significant advantage when material responses within a broad spectrum are required with high frequency resolution. Our method is evidently more efficient and robust than shutter-based acquisition, and it is especially advantageous for multidimensional spectroscopy, in which frequency-resolved measurements are repeated for different pulse delays. Furthermore, the functions performed by the microcontroller can be flexibly modified by uploading different programs. Since the microcontroller itself is a programmable computer, it can run independently from the main computer during data acquisition, which helps to release the working load of the CPU and the programing difficulty in correlating the chopper status with data acquisition of the CCD in real time. Compared with other acquisition boards such as NI DAQ, which usually costs hundreds of dollars, the $20 microcontroller is much cheaper and thus is especially useful for groups with multiple ultrafast spectroscopy systems.

3.3 Fluorescence-Detected 2D-ES

Another strategy for more radically improving the signal-to-noise ratio in 2D-ES is to implement fluorescence detection. This approach is especially necessary if experiments are to be performed on small ensembles or single molecules, where phase-matching conditions are not strong and cannot be used to isolate a desired nonlinear signal. When a third-order four-wave-mixing emission cannot be measured, the third order response can be accessed by fluorescence. A fourth interaction converts the final polarization (which in conventional 2D-ES emits the four-wave-mixing signal) into an excited state population (which emits fluorescence). The red-shifted fluorescence photons are then separated from the laser light using sharp cutoff filters and counted with sensitive detectors. The photon count then provides an indirect measure of the third-order polarization. However, in order to isolate only the fluorescence resulting from a single interaction from each pulse, the three beams must be phase-cycled, a technique borrowed from NMR spectroscopy. Our implementation of fluorescence-detected two-dimensional spectroscopy with 27-step phase cycling is described in the section below.

We present a novel experimental scheme for two-dimensional fluorescence-detected coherent spectroscopy (2D-FDCS) using a non-collinear beam geometry with the aid of confocal imaging of a dynamic (population) grating and 27-step phase-cycling to extract the signal. This arrangement obviates the need for distinct experimental designs for previously developed transmission detected non-collinear two-dimensional spectroscopy and collinear 2D-FDCS. We also describe a novel method for absolute phasing of the 2D spectrum. We apply this method to record 2D spectra of a fluorescent dye in solution at room temperature and observe spectral diffusion.

3.3.1 Introduction

In 2D-ES, interaction of a bulk sample with three optical fields from three non-collinear phase-stable pulses generates a time-dependent macroscopic third-order ($\chi^{(3)}$) polarization which emits a signal field in a background-free direction by virtue of momentum conservation of optical fields; this is known as phase-matching. The phase-stability at optical frequencies is maintained by a variety of techniques, e.g., 1) interferometer with i) passive phase-locking using diffractive optics [66], [98], [99] ii) active phase-locking using feedback electronics [100], and iii) inherently phase-stabilized geometry [101] and 2) (phase-only) pulse-shaping [102].

However, in a bulk sample ultrafast (coherent) dynamics is often obscured by inhomogeneous dephasing due to averaging over a large ensemble of molecules or molecular

complexes [103]. Thus one of the remaining challenges in this field is to enhance the sensitivity of 2D-ES to small ensemble of molecules (or molecular complexes), ideally to single molecule level [104], [105]. Note that despite the pioneering work by van Hulst and co-workers [106]–[108], 2D-ES of isolated single molecules has not been demonstrated yet. Although detection of single molecule by absorption was demonstrated both at low temperature [109] and quite recently at room temperature [110]–[112], the sensitivity is greatly enhanced by fluorescence detection [113] which has been a standard tool for single molecule spectroscopy [114]. Phase-matching, being a macroscopic phenomenon, does not apply in a small ensemble of molecules [70]. This motivates the extension of 2D-ES to two-dimensional fluorescence-detected coherent spectroscopy (2D-FDCS), pioneered by Warren and co-workers [115]–[117]. In 2D-FDCS (incoherent) fluorescence is recorded as a function of time delay between four collinear pulses. The specific third-order ($\chi^{(3+1)}$) signal is retrieved either by cycling through different relative phase-combinations among phase-stable pulses known as phase-cycling or by synchronous detection with respect to a reference phase-modulation in an otherwise phase-unstable interferometric set-up as developed by Marcus and co-workers [118]. The implementation of 2D-FDCS hinges on generation of *collinear* train of pulses with controllable delay and phase which requires instrumentation different from that in 2D-CS with *non-collinear* beam geometry; this is either met by spectral phase and amplitude shaping of a laser pulse with a pulse-shaper [115]–[117] or using Mach–Zehnder interferometers [118].

Here, we demonstrate 2D-FDCS of a fluorescent dye in solution at room temperature using conventional non-collinear beam geometry employed for phase matching in 2D-ES. We discuss how to isolate the pathway-specific signal with a combination of confocal imaging of dynamic (population) grating and 27-step phase-cycling; this allows us to use a single set-up to alternate between the two detection methods avoiding the need of having multiple experimental arrangements. We also present a new method for absolute phasing of the 2D spectrum.

3.3.2 Nonlinear 2D-FDCS: Concept

Nonlinear 2D-FDCS has been implemented to probe conformation of fluorescent dye aggregates [119], [120], spatially mapping nanoscale coherence [121]. For a two-level system, a comparison of the double-sided Feynman diagrams for 2D-CS with 2D-FDCS is shown in Figure 3.6. In 2D-FDCS four collinear phase-stable pulses modulate the excited state population which is proportional to the fluorescence intensity. The diagonal element of the density matrix may be written as [70]:

$$\rho_{ii}^{(3+1)}(t) = \int\int\int\int dt_4 dt_3 dt_2 dt_1 Q^{(3+1)}(t_4,t_3,t_2,t_1) E(t-t_4) E(t-t_4-t_3) E(t-t_4-t_3-t_2) E(t-t_4-t_3-t_2-t_1)$$

Equation 3.1

where $Q^{(3+1)}$ is the correlation function which contains all possible pathways. For the rephasing pathway it may be written as (with $\omega_{ee} = 0$):

$$Q^{(3+1)}(t_1, t_2, t_3, t_4) \propto \left|\mu_{ge}\right|^4 e^{-i\omega_{ge}t_1} e^{-i\omega_{ge}t_3} e^{-\Gamma_{ge}t_1} e^{-\Gamma_{ee}t_2} e^{-\Gamma_{ge}t_3} e^{-\Gamma_{ee}t_4}$$

Equation 3.2

where phenomenological decay constants are included to account for pure dephasing (Γ_{jk}) and population relaxation (Γ_{jj}).

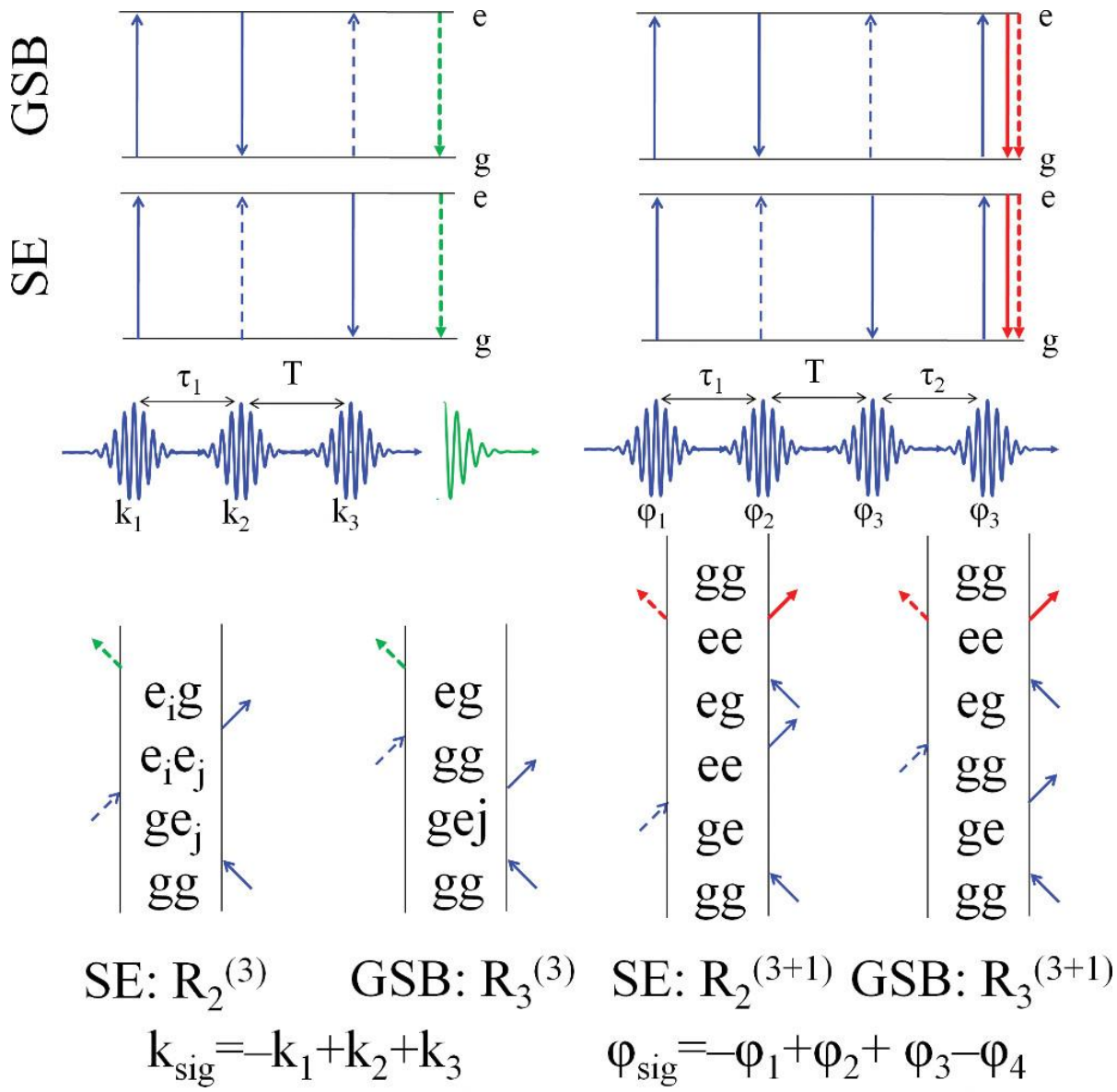

Figure 3.6 (From top) Energy level diagrams, pulse sequences, and double-sided Feynman diagrams for 2D-ES (left) and 2D-FDCS (right); incident field, coherent signal field, and incoherent fluorescence are shown as blue, green, and red arrows, respectively, while bra and ket side interactions are shown as solid and broken arrows, respectively.

The signal phase for the rephasing $Q^{(3+1)}$ pathway (for collinear geometry) in Figure 3.6 is:

$$e^{-i\varphi_1}e^{+i\varphi_2}e^{+i\varphi_3}e^{-i\varphi_4} = e^{-i\{\omega_0(t-t_1)-k_1.r\}}e^{+i\{\omega_0(t-t_2)-k_2.r\}}e^{+i\{\omega_0(t-t_3)-k_3.r\}}e^{-i\{\omega_0(t-t_4)-k_4.r\}}$$
$$= e^{i\omega_0(\tau_2-\tau_1)}$$

Equation 3.3

Unlike 2D-ES where only one coherence time (τ_1) is scanned (Figure 2), in 2D-FDCS both coherence times (τ_1 & τ_2) are scanned for a given waiting time (T) and for each τ_1-τ_2 combination phase-cycling is performed to isolate the rephasing or non-rephasing signal with phase $\pm(-\varphi_1+\varphi_2+\varphi_3-\varphi_4)$ or $\pm(+\varphi_1-\varphi_2+\varphi_3-\varphi_4)$. Fourier transform of the time-domain two-dimensional fluorescence interferogram along both τ_1 and τ_1 axes generates the 2D spectrum.

Since the observable is the excited state population, the role of the last pulse is just to convert the third-order coherence into a population; so this is still equivalent to a third order or $\chi^{(3)}$ process and we denote it as $\chi^{(3+1)}$ process to distinguish it from other fourth order or $\chi^{(4)}$ processes. Although the final population has a time dependence, we do *not* measure this time dependence of the excited state population; instead we measure the time-integrated or steady-state fluorescence instead of fluorescence life-time. In this way, 2D-FDCS functions similarly to any experiment probing excited state population, *e.g.* photoemission electron microscopy [121].

3.3.3 Experimental Implementation

Figure 3.7 shows a schematic of the experimental set-up:

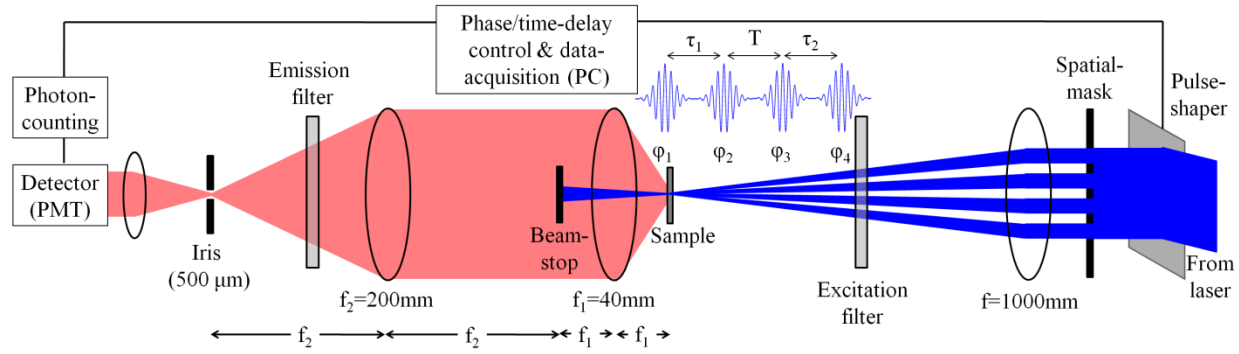

Figure 3.7 Schematic of the experimental set-up excluding the detail of the pulse-shaper which controls the temporal delay and phase of each pulse (blue) independently. Forward scattered fluorescence (red) is collected through an iris kept at the Fourier plane where the fluorescence interferogram is imaged.

The expanded beam from a Ti:sapphire regenerative amplifier (RegA 9000, Coherent), producing nearly transform-limited pulses (~55fs FWHM) at 250 kHz centered on 800nm, was guided to a phase-only pulse-shaper, originally designed by Nelson and co-workers [102], [122] and described elsewhere [123]. Briefly, the 4f zero-dispersion pulse-shaper utilizes a liquid crystal on silicon spatial light modulator (LCOS-SLM) with rectangular array of 792x600 pixels

(X10468, Hamamatsu) kept in the Fourier plane where the spectral components of the laser pulse were horizontally spread. Only the first-order vertically diffracted beam from the LCOS-SLM was used for the experiment to remove the higher-order satellite pulses. To generate different output beams/pulses from a single expanded input beam/pulse, the vertical array of 600 pixels was divided into several domains; within a given domain, application of a linear spectral phase with a partially rotating frame across the horizontal array of 792 pixels resulted in translation of the corresponding pulse in time. Thus the shaper can manipulate time delay and phase of each pulse. An additional spatial mask was placed at the output to generate a circular beam shape from the input rectangular beam. Note that, instead of the boxcar geometry usually employed for 2D photon-echo set-up, we chose the output beams vertically aligned in order to preserve parallel horizontal polarization.

3,3'-Dethylthiatricarbocyanine iodide (DTTCI) dye was purchased from Exciton and used without further purification; a solution of the dye in 1:1 ethanol:ethylene-glycol mixture was percolated through a 1mm path-length flow-cell (Starna) via a peristaltic pump to avoid photo-bleaching; in addition, we used a mechanical chopper running at 500Hz as 'bunched-pulse excitation' was shown to reduce photo-bleaching as well as photo-thermal effects [124], [125]**.** The optical density of the sample was ~0.3 at 800nm. The output beams from the pulse-shaper were focused on to the sample using a long focal length lens (f = 100cm). The forward scattered fluorescence) was collected with a 0.5NA aspheric lens (f_1 = 4cm) and the collimated fluorescence beam was imaged, with another lens (f_2 = 20cm), on the conjugate focal plane where a collapsible iris (or a pinhole, either with 500μm diameter) was kept for confocal detection. Thus, the optical interference pattern of the shallow-focusing non-collinear beams at the sample was imaged at the confocal plane with x5 magnification (since $f_2/f_1 = 5$) and the iris (or pinhole) spatially selected a small portion of the interference fringe, thereby enabling us to probe a small sample volume without spatio-temporal averaging (Figure 3.8).

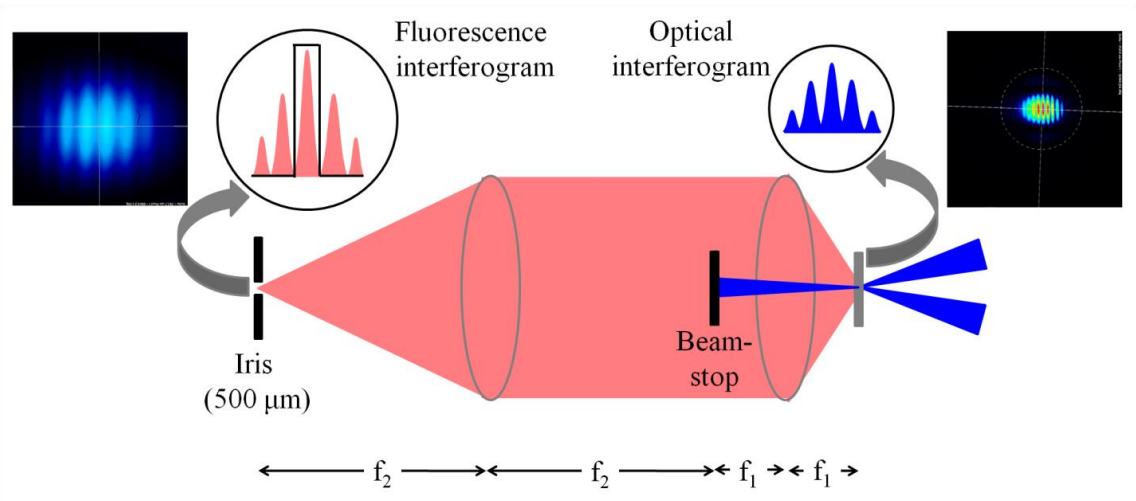

Figure 3.8 Schematic of confocal imaging dynamic grating; also shown are images of a two-pulse optical interferogram and magnified (x5) fluorescence (from DTTCI in ethanol/ethylene-glycol mixture) interferogram taken with a beam profiling CCD camera.

To block the excitation beam, a beam-stop was kept at the Fourier plane of the fluorescence collection optics so that the beam-stop does not impart any shadow on the image other than a small reduction of the fluorescence intensity. A long-pass emission filter (OD>6.0 for ≤825nm, custom-made, CVI-MellesGriot) was used before sending the fluorescence to a photo-multiplier (H7422P-50, Hamamatsu) with photon counting modules (C9744 and C8855-01, Hamamatsu). We used cage-structures (Thorlabs) to increase the mechanical stability of the confocal system and light-tight lens tubing before the PMT. All optical and opto-mechanical components were purchased from Thorlabs. The SLM and the PMT were interfaced with a personal computer where data acquisition was performed by a LabView program while for data processing and plotting we used Matlab.

Here we used a phase-only pulse-shaper to maintain phase-stability and perform phase-cycling, but the same can be met with any phase-stable non-collinear set-up where quasi phase-cycling can be performed by delaying pulses by a fraction of the wavelength, *e.g.* by tilting a Brewster window [126]. Moreover, instead of shallow focusing with vertical spatial mask, tighter focusing with boxcar mask can also be employed so long as the fluorescence interferogram without error, so that signal from only a single period of the interferogram is recorded.

3.3.4 Confocal imaging of a transient grating

According to Equation 3.3, for perfectly collinear pulses the relative phase varies only temporally, not spatially; consequently, as the delays are scanned a 2D temporal fluorescence interferogram is produced. This is precisely the reason for using collinear pulses in linear [127]–[129] and nonlinear [115]–[118] FD-CS experiments.

If two pulses interfere non-collinearly at the sample, for a given time delay between them the relative phase changes periodically across the sample as:

$$e^{i\Delta\varphi_{12}} \propto e^{i(k_1-k_2).r}$$

Equation 3.4

Consider the linear projection of this interference pattern across the beam profile. The condition for fringe maxima is given by:

$$(k_1 - k_2).x = 2kx\sin\theta = \frac{4\pi x}{\lambda}\sin\theta \equiv 2\pi n$$

Equation 3.5

where λ is the wavelength, θ the angle with respect to the normal of incidence, n an integer and we have assumed $|k_1| = |k_2| = k$. Thus the spatial period of the interference pattern is $= \frac{\lambda}{2sin\theta}$.

The relative phase of two pulses varies temporally as well as spatially (depends on both τ and *r*). This spatial phase variation periodically produces modulation of the population in ground and excited states across the sample, resulting in a dynamic population grating [130]. In fact, phase matching in 2D-CS (or transient-grating pump-probe spectroscopy) may be viewed as a scattering of the third pulse from this population grating encrypted by the first two pulses where the crossing-angle between pulses controls the phase-matching band-width [131], [132]; this is why non-collinear pulses are used in conventional 2D-ES. However, due to this very spatio-temporal coupling, only the spatial locations of crests and troughs change when τ is scanned and

the total fluorescence intensity (spatially integrated over the population grating) is conserved Thus, no fluorescence modulation results while scanning τ.

In our experiment, the shallow focusing (approaching the collinear limit with crossing angle ~0.1 degree) results in visibly six interference lobes which were magnified and imaged at the conjugate focal plane. The fringe spacing in the magnified image of any two successive beams (1&2 or 3&4) was slightly above 0.5mm as measured with a beam profiling CCD camera. An iris of 0.5mm diameter selects a single period of this pattern, allowing us to probe only a portion of the excitation volume and to avoid spatial averaging. Figure 3.9 shows the effect of spatial averaging on the temporal interferogram when we recorded the two-pulse fluorescence interferogram while gradually opening the iris. Note that the spatial interferogram along the beam propagation direction is negligible for a small crossing angle. A vertical mask (instead of a boxcar mask) ensures that the polarizations of different beams remain parallel at the focus, resulting in a simple and easily tractable four beam interference pattern.

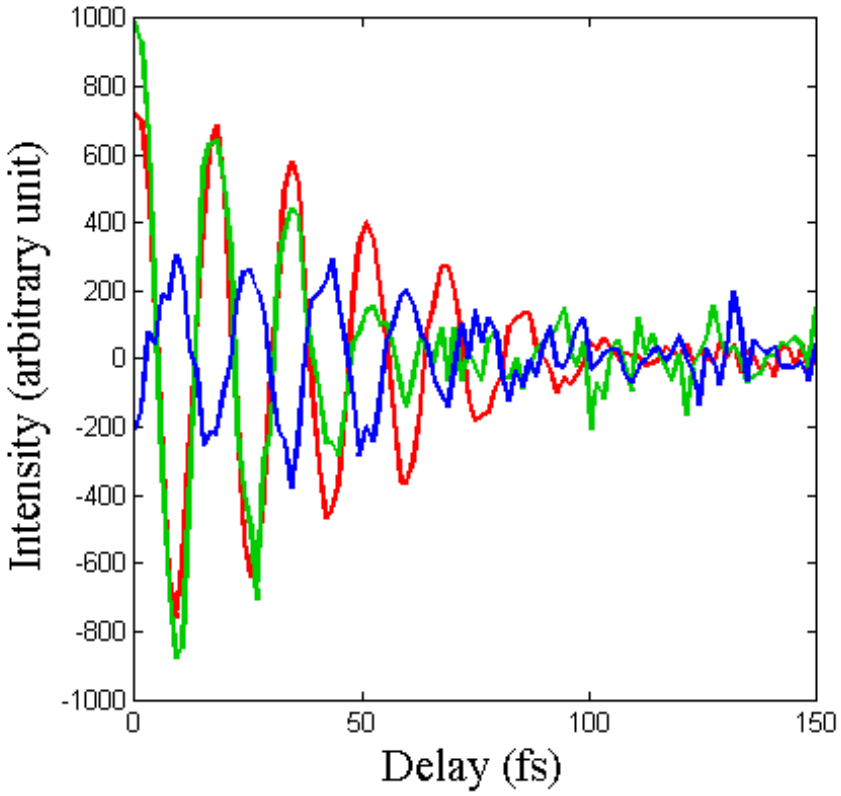

Figure 3.9 The effect of confocal iris diameter on two-pulse fluorescence interferogram from DTTCI in ethanol/ethylene-glycol mixture; the oscillations wash out due to spatial averaging over dynamic grating as the diameter is increased from 0.5mm (red) through 1.5mm (green) to 2.5mm (blue). Relative pulse delay was generated with a partially rotating-frame centered on 975nm and 2-step π phase-cycling.

3.3.5 Absolute phasing of the 2D spectrum

In 2D-ES the phase of the complex 2D signal is usually retrieved by comparing the projection of the 2D spectra on the emission axis with pump-probe spectra, exploiting the projection slice theorem [133]. Since in Equation 3.3 the signal phase is proportional to relative phases (φ_2-φ_1) and (φ_4-φ_3), one may directly measure the relative phases by recording the temporal interferogram with a pinhole [134] or by imaging the spatio-temporal interferogram at the focal plane with a camera [135]. In a similar spirit, we fix the absolute phase by adjusting the oscillation phase in the fluorescence interferogram. This is shown in Figure 3.10, where the each interference fringe is maximized at zero coherence time and superimposed.

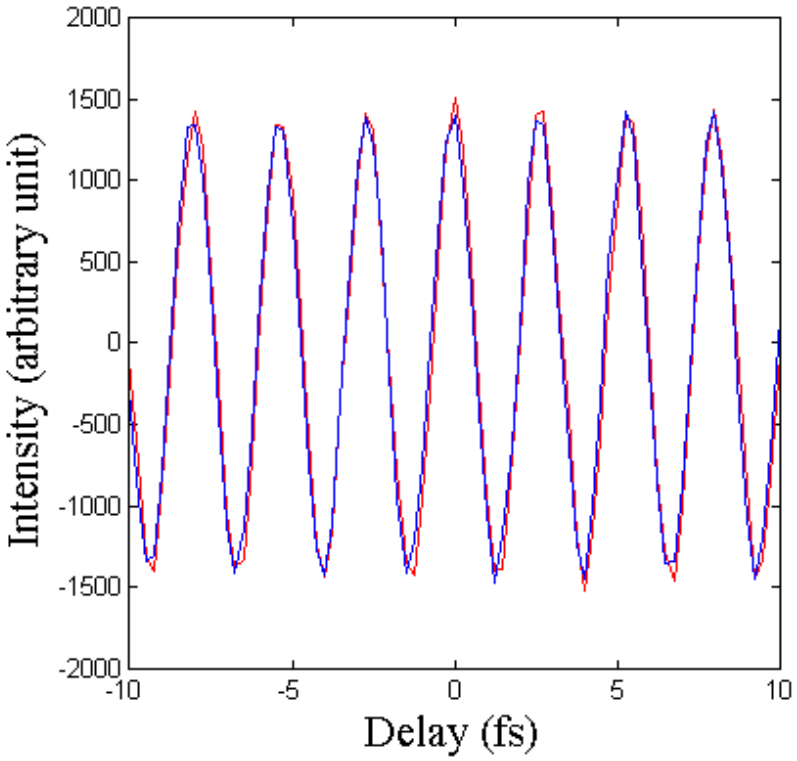

Figure 3.10 Absolute phasing of the 2D spectrum by superimposing the 12 (red) and 34 (blue) fluorescence (from DTTCI in ethanol/ethylene-glycol mixture) interferograms, both maximized at zero coherence time. Pulse 2 or pulse 4 was delayed with reference to laboratory-frame in combination with 2-step phase-cycling. Note the ~2.66fs oscillation period corresponds to the carrier frequency of the laser.

3.3.6 Pathway selection with phase cycling

When phase-cycling with a sequence of *n* pulses, the phase of i-th pulse (φ_i) is varied from 0 by increments of $^{2\pi}/_{m_i}$ ($\varphi_i = 0, 2\pi/m_i, 2*2\pi/m_i, 3*2\pi/m_i, \ldots, (m_i-1)*2\pi/m_i$); this is done for *n*-1 pulses. All possible permutations among φ_i are considered to get a table of

phases for a given inter-pulse delay, so that the total number of configurations is $= m_1 \times m_2 \times m_3 \times ... \times m_{n-1}$. We call this *M*-step phase-cycling. For a given set of pulse phases, the signal phase corresponding a specific dynamical pathway (that we wish to isolate) is calculated and the measured *total signal* (which has contribution from all pathways) is multiplied by a coefficient equal to the complex conjugate of the specific signal phase. The contribution of a specific pathway gets a weight of unity, while that of any other unwanted pathway gets a different weight since it has a phase different from the specific signal phase. This is repeated for every phase combination in the set and the signal contributions are summed to obtain a *processed signal*. The contribution of a specific pathway gets a weight equal to the number of phase combinations in the set while that of any other pathway is minimized. The value of m_i's are increased to get a new set of phase configurations and the process is repeated until the signal contributed from every other unwanted pathway gets a zero weight.

For 2D ($\chi^{(3+1)}$) FDCS, n = 4, and as before we first implemented a phase-cycle corresponding to $m_1 = m_2 = m_3 = 2$ & $m_4 = 1$, i.e. a 2x2x2x1 = 8-step phase-cycle.
It may be seen that with a 8-step phase cycle we can isolate all $\chi^{(3+1)}$ order pathways where each of the four pulses has perturbed the system only once; however, 8-step phase-cycling cannot separate between rephasing and non-rephasing pathways. For this a higher-step phase-cycling is required. The signal was processed as:

$$S^{processed} = (+1) * S^{total}_{\varphi_1=0,\varphi_2=0,\varphi_3=0,\varphi_4=0} + (-1) * S^{total}_{\varphi_1=\pi,\varphi_1=0,\varphi_1=0,\varphi_1=0} + \cdots + (+1) * S^{total}_{\varphi_1=\pi,\varphi_2=\pi,\varphi_3=0,\varphi_4=0} + (-1) * S^{total}_{\varphi_1=\pi,\varphi_2=\pi,\varphi_3=0,\varphi_4=0}$$

Equation 3.6

The spectra without phase-cycling and with 8-step phase-cycling are shown in Figure 3.11. Only a zero frequency noise spectrum is recorded without phase-cycling (Figure 3.11a) while 2D spectrum is retrieved with 8-step phase-cycling (Figure 3.11b).

A 3x3x3x1 = 27-step phase-cycling scheme ($m_1 = m_2 = m_3 = 3$, $m_4 = 1$) can isolate rephasing and non-rephasing pathways. To isolate the rephasing pathway, we processed the signal as:

$$S^{processed} = (+1) * S^{total}_{\varphi_1=0,\varphi_2=0,\varphi_3=0,\varphi_4=0} + (-0.5 + 0.866i) * S^{total}_{\varphi_1=0,\varphi_1=0,\varphi_1={}^{2\pi}/_{3},\varphi_1=0} + \cdots + (-0.5 + 0.866i) * S^{total}_{\varphi_1={}^{4\pi}/_{3},\varphi_2={}^{4\pi}/_{3},\varphi_3={}^{2\pi}/_{3},\varphi_4=0} + (-0.5 - 0.866i) * S^{total}_{\varphi_1={}^{4\pi}/_{3},\varphi_2={}^{4\pi}/_{3},\varphi_3={}^{4\pi}/_{3},\varphi_4=0}$$

Equation 3.7

As shown by Warren and co-workers [115]–[117], with a 4x1x4 = 16-step ($m_1 = m_3 = 4$, $m_2 = 1$) phase-cycling only the (2+1)-pulse photon-echo (equivalent to 2-pulse photon-echo in 2D-ES) signal (T = 0) can be isolated, for which a more economical 1x5x2 = 10-step ($m_2 = 5$, $m_3 = 2$, $m_1 = 1$) phase-cycling scheme exists [47]. However, with either scheme we cannot scan the population time (since the second and third field interactions are executed by the same pulse). This leads us to perform a 3x3x3x1 = 27-step phase-cycle to isolate the (3+1)-pulse photon-echo signal (containing information equivalent to the 3-pulse photon-echo in 2D-ES).

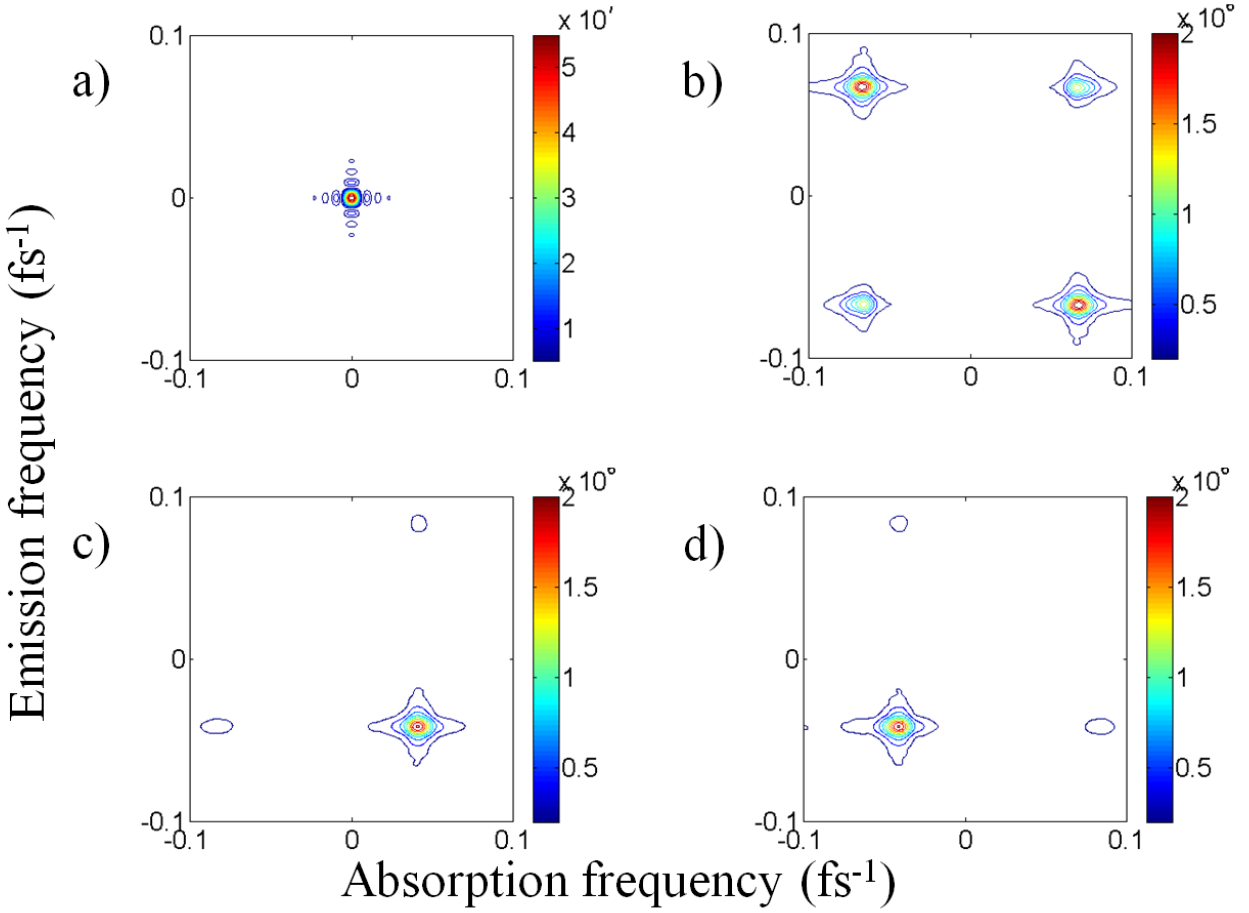

Figure 3.11 Absolute 2D spectrum (at T = 0 fs) of DTTCI in ethanol/ethylene-glycol mixture recorded (a) without phase-cycling, (b) with 8-step phase-cycling and (c-d) with 27-step phase-cycling isolating rephasing (c) and non-rephasing (d) specta; data were collected with a partially rotating-frame centered on 975 nm and is presented without adjusting the frequency shift after FFT. Note that the rephasing and the non-rephasing spectra appear in different quadrants as expected.

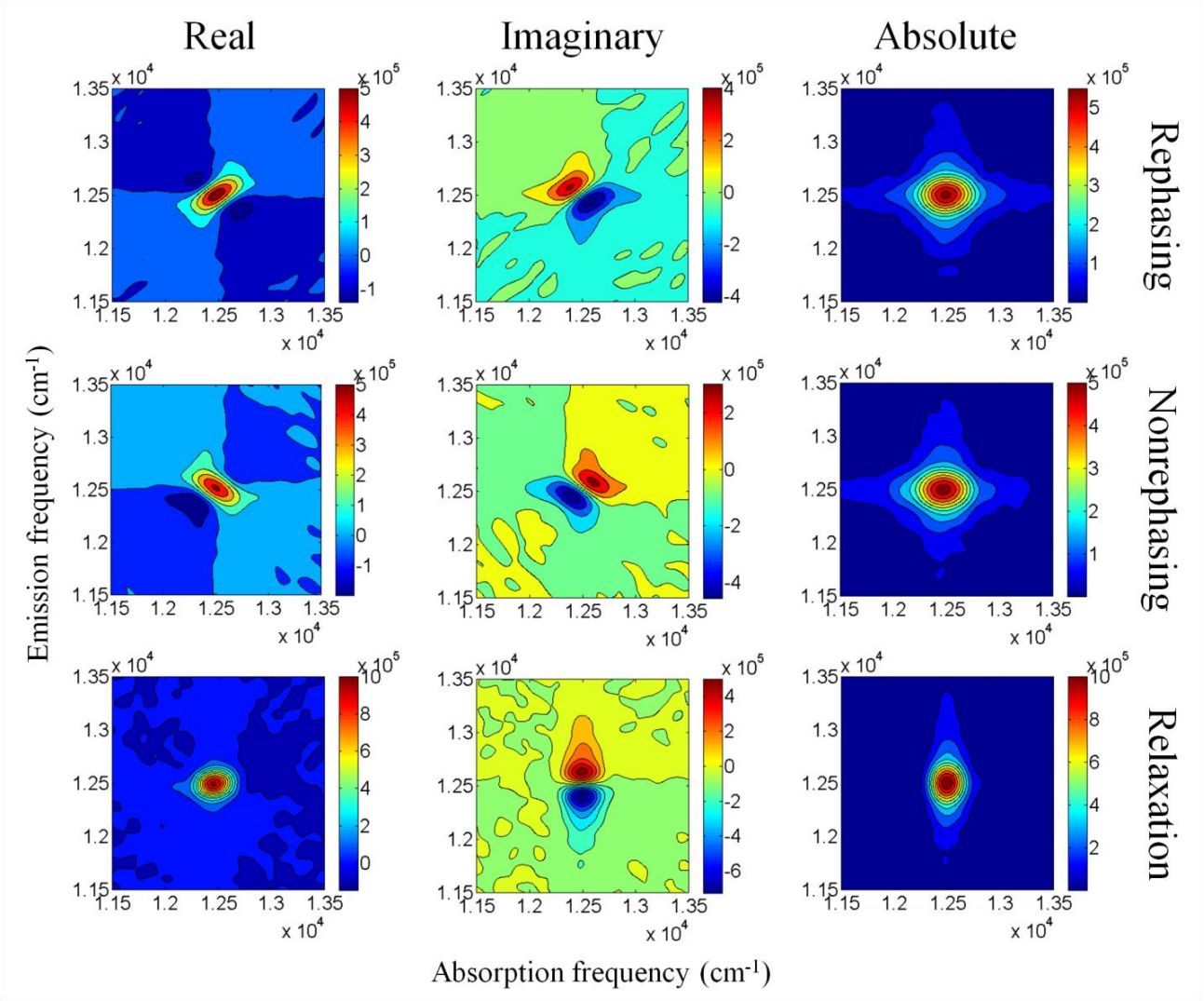

Figure 3.12 Real, imaginary and absolute parts of the 2D rephasing, non-rephasing and relaxation spectra (at T = 0fs) of DTTCI in ethanol/ethylene-glycol mixture; data were collected with a partially rotating-frame centered on 850nm with 27-step phase-cycling.

To record the 2D spectrum for a particular waiting time within a reasonable experimental time window, we changed the rotating frame center to 850nm. The 2D rephasing, non-rephasing and relaxation or total correlation (*i.e.* rephasing plus non-rephasing) spectra at zero waiting time are shown in Figure 3.12. We also collected 2D relaxation spectra at waiting times. As evident from Figure 3.13, the diagonal elongation observed at early waiting time decays at later times as a result of spectral diffusion. This demonstrates that a 27-step phase-cycling is necessary to isolate specific signal pathways as a function of waiting-time. Similar 27-step phase-cycling with four collinear pulses (followed by a fifth pulse in a non-collinear pump-probe geometry) have recently been implemented in a fifth-order 3D spectroscopy experiment [63].

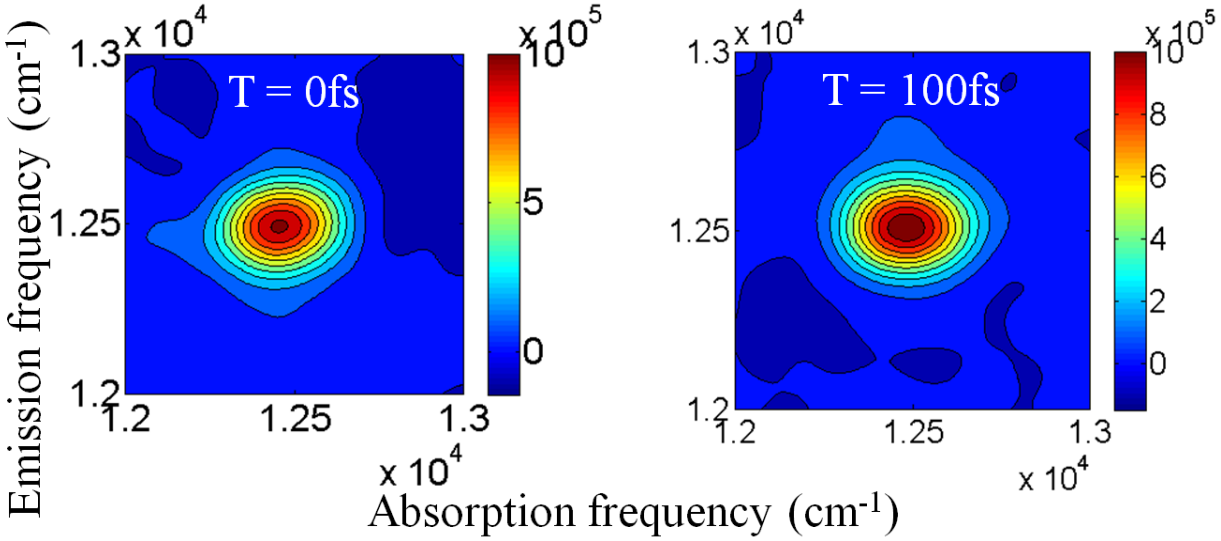

Figure 3.13 Real part of the 2D relaxation spectra of DTTCI in ethanol/ethylene-glycol mixture showing spectral diffusion.

3.3.7 Future Direction

To conclude, we have described a new method for implementing 2D-FDCS using the standard experimental design for 2D-ES with a non-collinear beam geometry, thus eliminating the requirement of having different types of experimental geometries and allowing facile interchange between the two methods. We have also demonstrated a novel way of absolute phasing of the 2D spectra by superimposing the two-pulse fluorescence interferograms.

2D-FDCS is advantageous over 2D-ES where phase-matching is difficult, *e.g.* in a highly scattering sample such as cellular membrane extract, or in a small ensemble of molecules. An immediate application of the present method would be imaging the entire pattern of the dynamic grating (*e.g.* with a CCD camera) to perform space-resolved 2D spectroscopy. Extending the present technique with enhanced sensitivity to smaller number of molecules in the probe volume will be of special interest to explore the microscopic detail of ultrafast coherent dynamics involving coupled chromophores.

3.4 Concluding Remarks

When embarking upon a 2D-ES study of a new material, it is important to consider the expected signal strength and scattering properties. A setup that works well for strong absorbers in solution may not be so appropriate for studying dilute solutions, amorphous films, or single-layer materials. The first and easiest remedy for noisy data can be to experiment with time domain windowing in the data processing. Next, while dynamical scatter subtraction increases the experimental time 2 or 4x, the decrease in residual scatter was found necessary for the experiments described in Chapters 4 and 5. For setups that include a pulse shaper, phase cycling **(**or quasi phase cycling [126]**)** allows shot-to-shot scatter subtraction without sacrificing signal

accumulation. Finally, because our fluorescence detection strategy requires scanning an additional time delay, it squares the experimental time. This severely limits this method's usefulness, especially on samples that degrade or photobleach during hours or days-long signal acquisitions. Nevertheless, for robust samples with very weak signals, the fluorescence-detected 2D-ES may allow experiments that would not otherwise be possible.

4 2D-ES of Electron-Phonon Interactions in Lead Halide Perovskite

Material in this Chapter is adapted with permission from Ref [136]:
"A Room Temperature Coherent Optical Phonon in 2D Electronic Spectra of $CH_3NH_3PbI_3$ Perovskite is a Possible Cooling Bottleneck"
by Daniele M. Monahan, Liang Guo, Jia Lin, Letian Dou, Peidong Yang and Graham R. Fleming
Journal of Physical Chemistry Letters DOI: 10.1021/acs.jpclett.7b01357

A hot phonon bottleneck may be responsible for slow hot carrier cooling in methylammonium lead iodide hybrid perovskite, creating the potential for more efficient hot carrier photovoltaics. In room-temperature 2D electronic spectra near the band edge, we observe amplitude oscillations due to a remarkably long lived 0.9 THz coherent phonon population at room temperature. This phonon (or set of phonons) is assigned to angular distortions of the Pb–I lattice, not coupled to cation rotations. The strong coupling between the electronic transition and the 0.9 THz mode(s), together with relative isolation from other phonon modes, makes it likely to cause a phonon bottleneck. The pump frequency resolution of the 2D spectra also enables independent observation of photoinduced absorptions and bleaches independently and confirms that features due to band gap renormalization are longer-lived than in transient absorption spectra.

By repeating the measurements at 90 K, we were able to observe similar coherent phonon oscillations in the low-temperature orthorhombic phase. The phonon signature in the orthorhombic phase is slightly narrower and red shifted compared to the tetragonal phase, consistent with low temperature THz spectra of this material.

4.1 Introduction

Hybrid organic-inorganic perovskites, especially methylammonium lead iodide (MAPI), have in recent years demonstrated remarkable increases in photovoltaic efficiency. Despite a soft, fluctuating structure, MAPI films exhibit an impressive set of optoelectronic properties, including microsecond carrier lifetimes, high carrier mobility, and long carrier diffusion lengths [137]–[142]. From the intensive study of these materials in recent years, it has become clear that fundamentally different physics are responsible for the high performance of hybrid perovskite photovoltaics as compared to more traditional solid state semiconductor devices. In addition to their promise for solar energy, hybrid perovskites may find applications in LED, photodetector, laser [143], [144] and thermoelectric[145] devices. Because these materials are solution processible, they are potentially quite economical. Unfortunately, MAPI's commercial applications are limited by thermodynamic instability,[146] moisture sensitivity, and lead toxicity. Understanding the principles and mechanisms behind this material's exceptional optoelectronic properties is an important step in the search for a variant material with the potential for wider application [147].

Unlike conventional solid-state inorganic photovoltaics, MAPI is soft and polarizable. At room temperature, it has a high dielectric constant and strong Coulomb screening. This results in small exciton binding energies [148], [149] and consequent rapid free carrier generation upon photoexcitation. Screening effects are also important in determining the strength of carrier-carrier and carrier-lattice interactions. Wang et al. observed a large difference in carrier lifetimes between the low temperature orthorhombic phase of MAPI and the room temperature tetragonal phase, [92] consistent with the changes in Coulomb screening caused by the discontinuity in the dielectric constant across this phase boundary. Zhu and co-workers proposed a "large polaron" model [150] to explain the slow recombination at room temperature. In the polaron model, the methylammonium cation rotations and/or lattice deformations rapidly respond to charge carrier generation, creating a solvation-like envelope and a barrier to recombination. Indeed, Zhu and co-workers' optical Kerr effect measurements showed liquid-like reorientation dynamics stemming from the organic cation [151]. In a recent 2D-IR study,[152] Bakulin et al. directly measured the organic cation reorientations, observing separate fast (~0.3 ps) and slow (>2 ps) timescales. However, the extent to which the organic cation (as opposed to deformations of the inorganic lattice) might contribute to screening or polaron formation remains an open question.

The observation of persistent hot carriers [153]–[155] presents another intriguing prospect for hybrid perovskite photovoltaics. Paired with energy-selective electrical contacts, such a material could be used to make a hot-carrier solar cell with the potential to surpass the Shockley-Quessier efficiency limit. Zhu and co-workers suggested [150], [155] that reduced carrier-lattice interactions due to polarons could explain the slow cooling observed in transient absorption[153], [154] and time-resolved two-photon photoelectron [155] measurements. Beard and co-workers instead proposed that a hot-phonon bottleneck produces the effect. A bottleneck forms when an excited phonon subpopulation relaxes so slowly that, at high excitation densities, it nears thermal equilibrium with hot carriers. This model naturally raises the question of which phonon modes are responsible for a bottleneck, so that phonon engineering approaches (common in the design of thermoelectric materials) might be applied to optimize perovskites for hot carrier photovoltaics. Very recently, Yang et al. [156] suggested that acoustic phonon up-conversion could allow energy to be recycled into the lowest frequency optical phonons, producing the bottleneck.

4.2 2D Electronic Spectroscopy at the Band Edge

Here we present 2D electronic spectra of MAPI thin films at room temperature and covering the energy region near the band edge. The waiting time dynamics show carrier cooling as well as a persistent "warm" carrier population above the band edge. We also observe a long-lived coherent phonon at 0.9 THz, which we identify as potentially responsible for a hot phonon bottleneck. Finally, we observe that the pump frequency resolution in a 2D spectrum allows the photo-induced absorption feature due to bandgap renormalization to be observed independently from the carrier cooling dynamics.

Figure 4.1a shows the shape of the MAPI film absorption spectrum near the band edge together with the laser spectrum after it has passed through the sample. A flat laser spectrum covering 1.55-1.75 eV yields a peak in the transmitted light at frequencies below the band edge. Figure 4.1b shows the laser pulse sequence used to obtain a 2D spectrum. Each 2D plot is obtained by scanning the coherence time τ for a set value waiting time T.

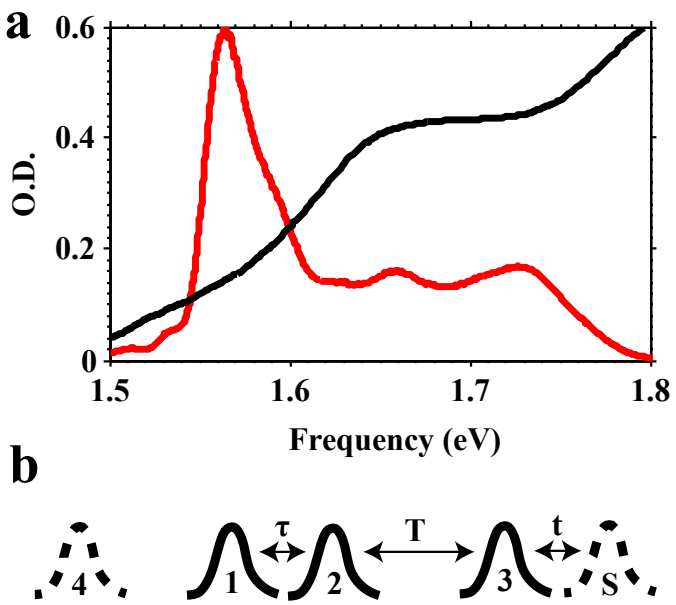

Figure 4.1 (a) Linear absorption spectrum of 150 nm thick MAPI film (black) and transmitted laser power spectrum (red), which acts as the local oscillator for heterodyne detection, and places the limits on the frequencies in the 2D spectrum. At 1.65 eV the optical density of the film was 0.6. (b) Pulse sequence and time delays for 2D electronic spectroscopy. Pulses 1 and 2 provide pump interactions; pulse 3 is the probe; pulse 4 is the local oscillator used for heterodyne detection; 'S' denotes the emitted echo/four-wave mixing signal. We refer to the delays τ and T as coherence time and waiting time, respectively. For a more detailed description of 2D-ES, refer to Brixner et al. [66].

The excitation frequency ω_τ is obtained via Fourier transform from the time domain data, while the emission frequency ω_t is measured by a spectrometer. The result is displayed as a 2D time-resolved frequency correlation spectrum, as in Figure 4.2.

Figure 4.2 shows the real portion of the phased 2D spectra at a progression of waiting times. The initial carrier density is $n = 1.3 \times 10^{18}$ cm^{-3} (see calculation in Experimental Methods). The dominant signal is a bleach resulting from absorption at and above the band edge (1.65 eV). Within the first 300 fs, the main peak shifts slightly below the diagonal. This indicates the rapid lattice reorganization and/or carrier thermalization, which was very recently investigated with 2D-ES using ultrashort pulses.[157] A broad bleach below the diagonal grows as carriers initially excited above 1.65 eV cool to fill the states along the sloping band edge. For pump energies below the band gap, we observe a broad photo-induced absorption (PIA) feature, which has been previously observed in transient absorption measurements [153],[154]. The PIA red of the band edge is attributed to bandgap renormalization, a photo-induced red shift that results when carrier-carrier exchange and correlation interactions lower the conduction band energy. This feature is only visible for pump energies below the band gap because at higher pump energies it is canceled by the strongly positive bleach feature. Interestingly, the PIA observed here appears less transient than was observed at the same probe energy in transient absorption.

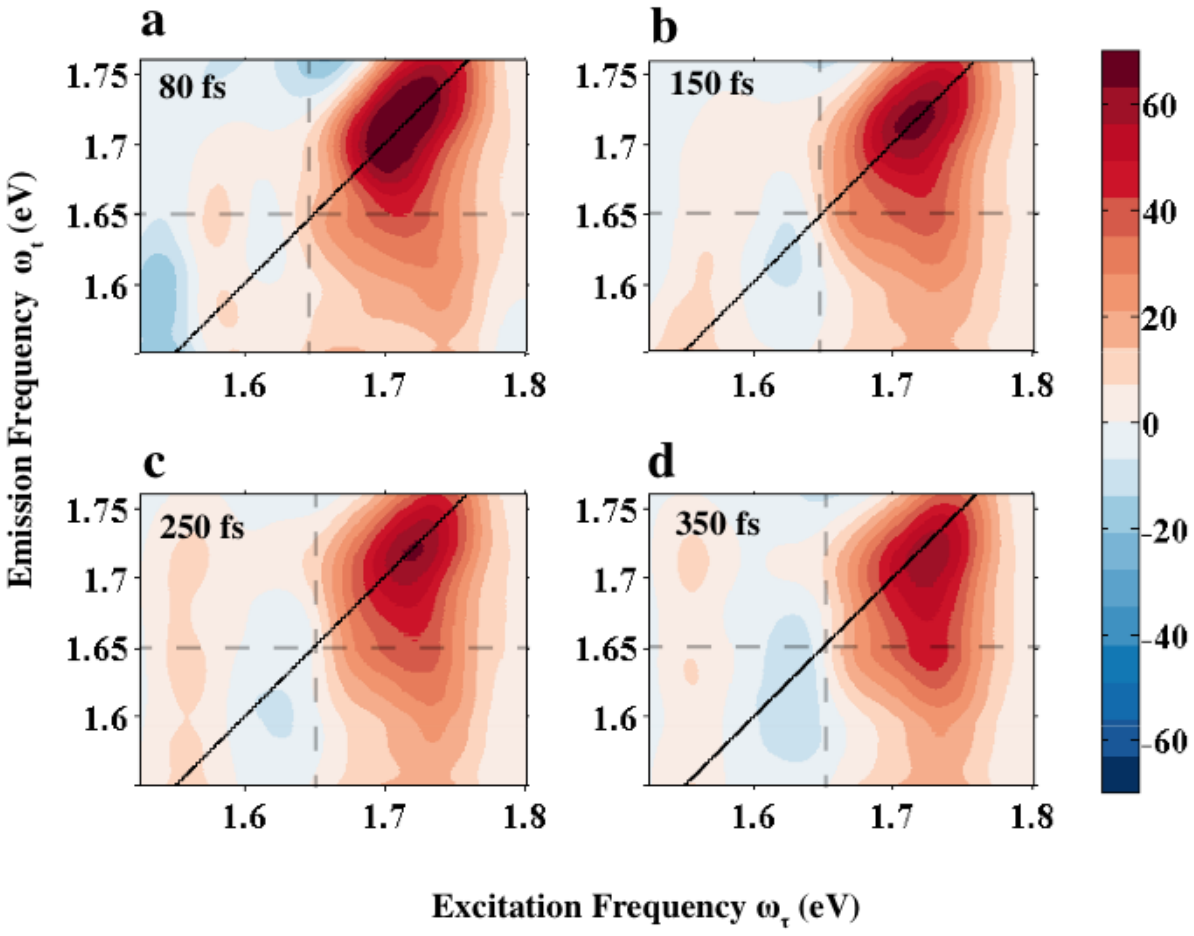

Figure 4.2 Real (absorptive) 2D spectra of MAPI films at waiting times a) T=80 fs b) T= 150 fs c) T=250 fs d) T= 350 fs. The black line marks the spectrum diagonal, and the band edge at 1.65 eV is marked with the dashed lines. The positive (bleach) signals are colored red, and negative (photo-induced absorption) signals are blue. A downward elongation of the main bleach feature results when carriers cool toward the band edge.

Indeed, a feature due to band gap renormalization should decay on a similar timescale as the carrier population. In transient absorption spectra, the PIA is canceled on a more rapid timescale as the lower diagonal bleach feature associated with hot carrier cooling grows in. The pump frequency resolution in a 2D spectrum therefore allows the bleach and PIA signals to be measured semi-independently.

Figure 4.3a shows the total absolute-value 2D spectrum taken at waiting time T=10 ps. The average amplitudes within the boxed areas are plotted in Figure 3b. The red and orange traces show the cross-peak growth associated with carrier cooling, with an exponential rise time of about 300 fs.

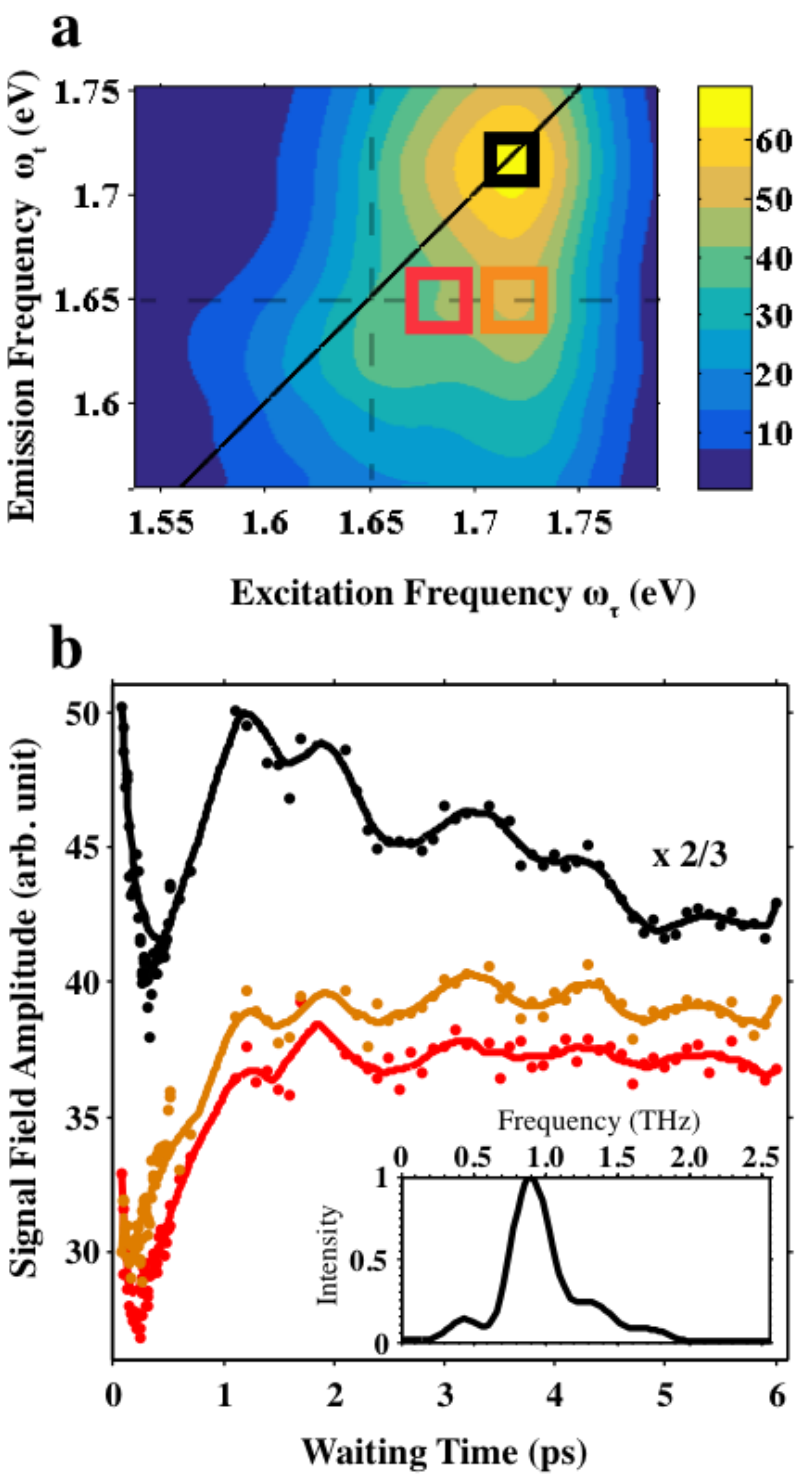

Figure 4.3 (a) Total (absolute-value) 2D spectrum at T = 10 ps, with boxed regions of interest corresponding to the main diagonal peak above the band edge (black) and two lower cross peak areas (orange and red). The band edge at 1.65 eV is marked with the dashed lines. (b) Plots over waiting time of the absolute value spectrum amplitude averaged over the different boxed regions shown in (a). Lines to guide the eye have been drawn using a smoothed spline interpolation of the raw data points (also plotted). Amplitude oscillations in the black, red, and orange curves decay with exponential lifetimes of 4 ps, 6 ps, and 18 ps respectively. The main diagonal peak amplitude plot (black) has been scaled by a factor of 2/3. Inset: Fourier power spectrum of the coherent phonon amplitude oscillations obtained from the spline interpolation of the lower cross peak trace (orange line) from 2 to 6 ps. Early time data was omitted to remove the zero-frequency component, while the 0.1 ps data interval only adequately samples frequencies up to about 2.5 THz. The peak frequency is at 0.9 THz (30 cm^{-1}, 3.7 meV).

However, the majority of the carriers remain above the band edge for more than 6 ps, as evidenced by the slow decay of the upper diagonal peak. The bandwidth available in our experiment shows that the slow cooling occurs for carriers with a broad range of energies up to at least 75 meV ($3k_BT$) above the band edge. Though our experiment does not measure hot carriers far above the bandgap, the slow cooling we observe for these "warm" carriers is consistent with that previously observed in transient absorption [153], [154] and time-resolved two-photon photoelectron [155] measurements.

4.3 Coherent Phonon Oscillations

The traces in Figure 4.3b show very clear amplitude oscillations, with the same phase and frequency preserved throughout different areas the 2D spectrum. The Fourier power spectrum of these oscillations peaks strongly at 0.9 THz, as shown in the inset. Such oscillations in the 2D electronic spectrum are caused by the evolution of vibrational wavepackets (phonons), generated through an indirect bandgap excitation and interacting with the charge carriers.

The frequency matches that of coherent phonon oscillations recently observed in pump-probe experiments on MAPI films in the orthorhombic phase at 77 K [158], though not previously seen at room temperature. Because the 2D spectrum measurement is background-free, oscillations can be measured more sensitively than by transient absorption. Moreover, when the signal is integrated over the excitation axis as in transient absorption spectroscopy, small phase differences can attenuate the resulting sum oscillation. We note that the limited range of waiting times measured in this work effectively broadens the Fourier peak, so that the width is not necessarily meaningful.

A collection of modes in the 0.9-1 THz frequency range have been assigned to a set of Pb-I-Pb angular distortions with mixed transverse-longitudinal optical character [159]. This frequency has been previously observed in both Raman [159], [160] and THz [159], [161] spectra of MAPI in both the orthorhombic and tetragonal phases. In fact, owing to low symmetry in the MAPI structure, phonons cannot be simply assigned to irreducible symmetry groups, and most exhibit both Raman and IR activity [160]. It is therefore interesting that the 2D spectra show no influence from the second prominent collection of optical phonons near 2 THz [161]. These modes were assigned to Pb-I bond stretches, and are strongly coupled to the methylammonium tumbling because the cage contractions lead to collisions with the interstitial cation [162]. This is in stark contrast to the Pb-I-Pb angular distortions, which preserve bond length and are essentially uncoupled to the organic cation.

4.4 Low Temperature 2D Spectra and Coherent Phonon Oscillations

MAPI is exceptional among hybrid perovskites in that it undergoes a phase transition at 160 K. Below this transition, the crystal structure is orthorhombic. The broken symmetry in this structure is energetically favorable because it allows a closer Pb-I bond distance along the compressed direction of the orthorhombic cell. Above 160 K (k_BT = 14 meV, 3.3 THz), methylammonium rotational degrees of freedom become accessible, so that entropy favors a lattice expansion to a tetragonal structure that enables free cation motion. As temperature increases, there is a slow continuous transition to a more highly symmetric cubic phase.

The phase transition in this material offers an opportunity to examine how small changes in the Pb-I lattice structure affects the electronic properties. The transition causes a sharp discontinuity in the temperature dependence of the low-frequency dielectric constant $\epsilon(0)$, which is up to 4x larger in the tetragonal phase than in the orthorhombic phase [163]. This difference in dielectric screening is likely responsible for an increased exciton binding energy at low temperature. The exciton can be seen as a sharp resonance in the linear absorption spectrum:

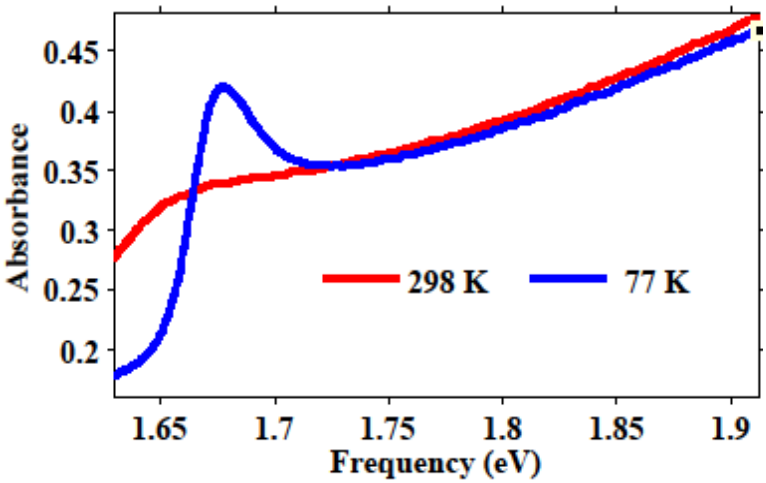

Figure 4.4 Linear absorption of 400 nm MAPI films in a N_2 cryostat at 298 K (red) and 77 K (blue).

Previous work in our lab [92] showed that the transient absorption signal decays much faster in the low temperature orthorhombic phase, either due to faster carrier recombination or exciton-exciton annihilation. Because the dielectric constant of MAPI strongly depends of electric field frequency [164], the difference in ultrafast response in the two phases cannot be just understood in terms of the low-frequency dielectric constant; not all of the polarizations and nuclear motions that contribute to $\epsilon(0)$ respond rapidly enough to affect ultrafast dynamics. Thus the exact physical origin of the difference in transient absorption lifetime remains to be explained.

We found that the difference between a lineshape dominated by excitons vs. free carriers can also be seen in 2D spectra of MAPI in its two phases. Figure 4.5 shows spectra of the same 400 nm film taken at 90 K and 298 K. These spectra were dominated by a lower diagonal peak corresponding to excitation and emission both near the band edge, and a cross-peak corresponding to higher energy excitation followed by cooling to the lowest lying states in the conduction band. The 90 K spectrum shows a sharp, round peak at around 1.68 eV, the same position as the excitonic peak in the linear absorption spectrum. While the orthorhombic MAPI absorbs light with energy above the exciton resonance, excitations rapidly relax into the bound exciton state. By contrast, in the 298 K spectrum the emission is more broad, with the strongest signal coming from the band edge, below 1.65 K. This indicates that in the tetragonal form, when the exciton binding energy is small, hot carriers cool to populate a wider distribution of states near the band edge.

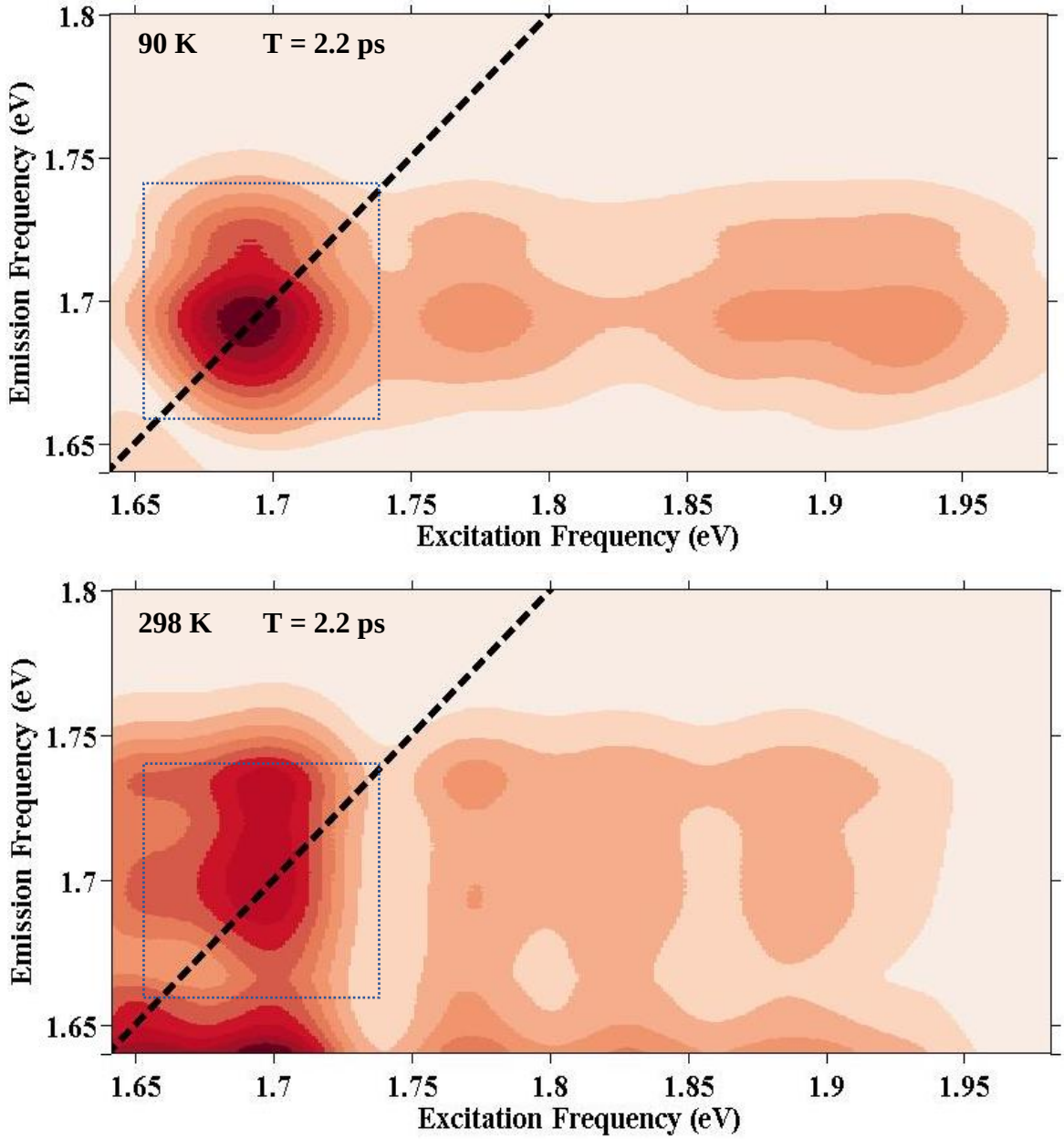

Figure 4.5 Total amplitude 2D spectra of the same 400 nm thick MAPI film at 90 K (top) and 298 K (bottom). The dashed black line marks the spectrum diagonal, and the box shows the integration area for the Fourier transform over waiting time (Figure 4.6).

Using the same data processing techniques described in the caption of Figure 4.3, coherence oscillations were also found in waiting time traces of these spectra (Figure 4.6). The 298 K oscillations are centered at 0.89 THz, while the 90 K oscillations are shifted to 0.81 THz. This is in good agreement with a phonon frequency shift that has previously been measured in a low temperature THz spectrum [162].

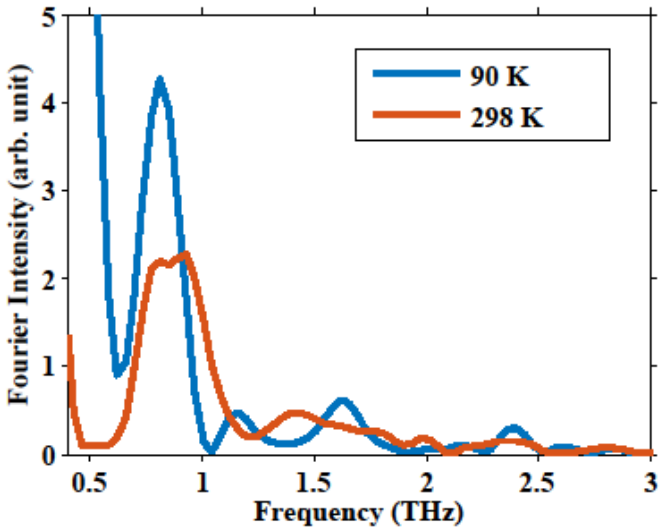

Figure 4.6 Fourier power spectrum of 2D spectrum amplitude oscillations integrated over the boxed region shown in Figure 4.5. The same sample was examined at 90 K (blue) and 298 K (red).

The relative amplitudes have not been rescaled, but are not necessarily useful to interpret, because they depend on many data processing variables including the spectrum integration region and the zero frequency component subtraction. Still, it appears the low temperature THz oscillation peak is more narrow than that measured on the same sample at 298 K. This implies that the coherent phonon in the orthorhombic form has a slightly longer lifetime. We also note that the linewidth in Figure 4.6 is broader than the true lifetime, because the first 2 ps are truncated to avoid the large zero-frequency component (and to avoid an early-time artifact inherent in our 2D-ES setup as described in Section 3.1).

That the same coherent phonon oscillations can be observed both in the low temperature orthorhombic phase (where cation motions are locked) and in the tetragonal phase at room temperature (where cations reorient freely) further indicates that the coherent modes do not couple to the methylammonium cation. We note that observing the organic cation librations themselves (strongest around 5 to 7 THz) in 2D spectral oscillations would require a greater sampling rate over the waiting time than used in this work.

4.5 Phonon Assignment and Possible Bottleneck

The vibrational dephasing times evidenced by the amplitude decay of the 0.9 THz oscillations are remarkably slow. At room temperature, oscillations on the main diagonal peak (Figure 4.3b, black) decay with an exponential lifetime of $\gamma^{-1} = 4$ ps, while the two lower cross peak regions show $\gamma^{-1} = 6$ ps (Figure 4.3b, red) and $\gamma^{-1} \approx 18$ ps (orange). Dephasing times are greater or equal to this at 90 K, as can be seen by the relative peak widths in Figure 4.6. By contrast, Leguy et al. estimated a much shorter lifetime of ~100 fs for the 2 THz mode from the Raman linewidth at 300 K (but did not have sufficient experimental resolution to estimate lifetimes for the modes near 1 THz) [159]. The long dephasing times suggest that the 0.9 THz

optical phonon(s) we observe has a strong coupling to the electronic transition, but weak interactions with the remainder of the phonon modes, especially compared to the 2 THz mixed organic-inorganic mode. The strong coupling between the inorganic-only phonon and the electronic transition is consistent with a calculation by Kawai et al. [165] predicting that charge carriers couple mainly to the lattice and only indirectly to the interstitial cation, because the valence and conduction band states involved in the near-band edge transitions consist of only I and Pb orbitals. However, an isotopic substitution study by Gong et al. demonstrated that carrier lifetimes indeed depend on the cation libration frequency [166]. Together with the absence of persistent hot carriers in the all-inorganic perovskite $CsPbBr_3$ [151], this suggests that the organic cation still plays a key role. The following picture emerges: electronic transitions and free charge carriers interact on the shortest timescales only with the inorganic lattice phonons, especially a low frequency mode involving only angular distortions. On longer timescales, the organic cation begins to have an indirect influence on the charge carriers via the coupling between cation rotations and lattice stretching modes. If a large portion of the initial energy lost to the lattice is deposited in the coherent 0.9 THz mode(s), isolated from the rest of the lattice, a bottleneck could form.

Because MAPI films have poor thermal conductivity, suggesting strongly scattered and/or highly localized acoustic phonons, it is tempting to think that acoustic phonons might be responsible for the bottleneck effect. However, our observation of coherent phonon oscillations is evidence contrary to the recent suggestion that the bottleneck is due to acoustic phonon up-conversion, [156] because a cooling and up-conversion cycle would not preserve the phonon phase coherence. Therefore, if up-conversion into the low-energy optical phonons contributes to the bottleneck effect, it is only on timescales greater than ~10 ps.

Understanding the interaction of optical excitations and charge carriers with the nuclear motions of the lattice is critical to unraveling the puzzle of perovskites' remarkable photovoltaic properties. The enhanced resolution afforded by two energy axes in two-dimensional electronic spectra clearly reveals the coupling between the electronic transition and a coherent 0.9 THz optical phonon(s) in methylammonium lead iodide. It seems likely that the electrons also couple strongly to these motions, which in turn interact weakly with the rest of the phonon bath, making it a good candidate as the origin of a phonon bottleneck. Modes near 0.9 THz mode are assigned as to Pb-I-Pb angular distortions, which do not couple to the methylammonium cation reorientations. Despite the striking difference in both charge carrier relaxation and cation rotational freedom between the tetragonal and orthorhombic forms, what is not clear is whether the methylammonium cation interacts with the charge carriers on timescales relevant to the electron cooling.

4.6 Experimental Methods

4.5.1 Methylammonium Lead Iodide (MAPI) Films

Samples were prepared in by Dr. Jia Lin in Peidong Yang's lab at Berkeley. To fabricate ~150 nm thick MAPI films used in the first set of room temperature experiments, a two-step method was adopted. 0.2 M PbI_2 in N,N-dimethylformamide (DMF) was spin-coated at 4,000 rpm onto the glass substrate, and then heated at 75°C for 5 min. The perovskite film was grown by dipping the PbI_2 film for 1 minute in a 8 mg ml^{-1} solution of methylammonium iodide in 2-propanol at a temperature of 75°C. The substrate was then dried by heating on a hotplate to

100°C for 10 min. A similar procedure was optimized to generate 400 nm films of high optical quality, except that the spin coater was set to 1500 rpm (these were used to take the 90 K and 298 K spectra in Section 4.4). All the processes were carried out in a N_2 filled glove box. Samples were exposed briefly to air when transferring to an N_2 filled optical cryostat for the spectroscopic experiments.

4.5.2 Carrier Density Calculation

For the first set of room temperature experiments, using the conventional equation

$$n_0 = \frac{(1 - T - R) * \phi}{h\nu * l}$$

Equation 4.1

(transmission $T = 10^{-0.6}$; reflection $R = 11\%$; total pump fluence $\phi = 8.2$ uJ/cm^2 ; photon energy $h\nu = 1.65$ eV; film thickness $l = 150$ nm), we calculate an excitation density of n_0 = 1.3 x 10^{18} cm^{-3}. However, because this calculation does not take into account the overlap between the sample absorption spectrum and the laser spectrum, it is only an estimate.

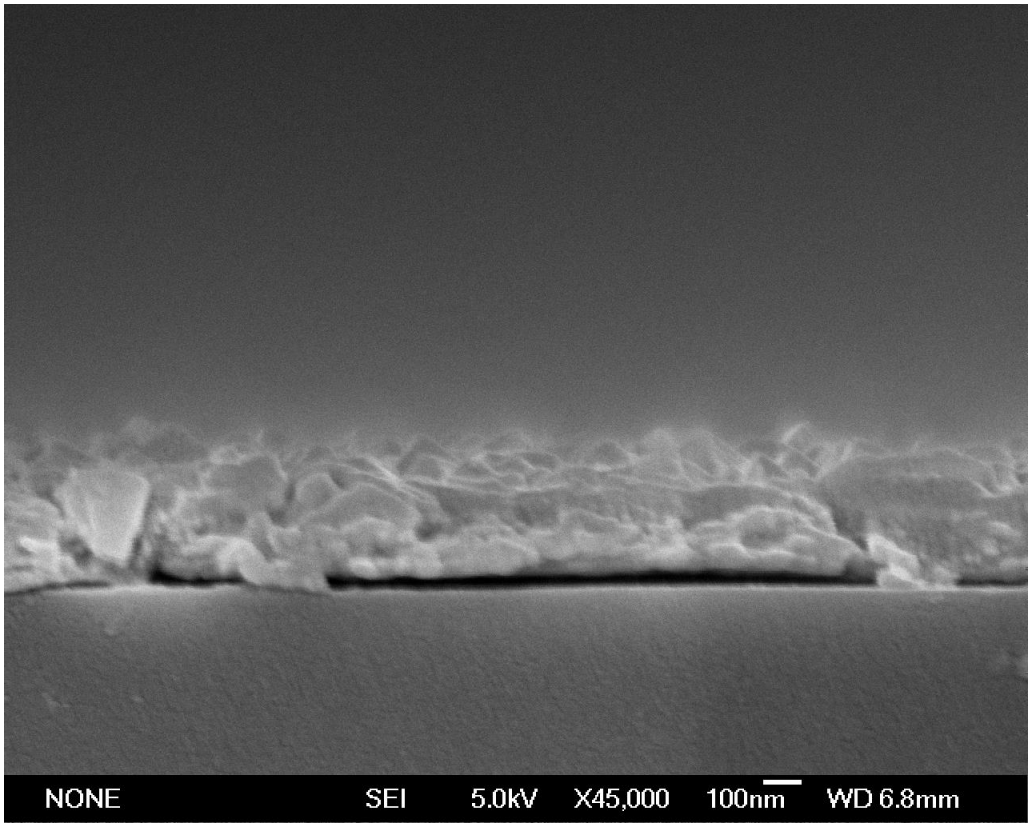

Figure 4.7 Cross-sectional TEM of a sample from the same preparation as those used for the experiments in Section 4.4. The film thicknesss is approximately 400 nm, but it is highly disordered with a far from uniform crystalline structure.

The uncertainty in carrier density is compounded by the fact that the film thickness was not measured precisely. The second set of 298 K and 90 K experiments were carried out with a similarly prepared film. This time the thickness was measured to be ~400 nm using cross-sectional TEM, shown in Figure 4.7.

In order to better compare the carrier density generated by the same laser pulses on the tetragonal and orthorhombic MAPI, we compute n_0 using a more exact formula:

$$n_0 = \int d\omega \frac{(1 - T(\omega) - R(\omega)) * \phi(\omega)}{\hbar\omega * l}$$

Equation 4.2

For the 400 nm films, this gives $n_0 = 1.2 * 10^{17}$ cm^{-3} in the orthorhombic phase at 90 K, but $n_0 = 1.4 * 10^{17}$ cm^{-3} in the tetragonal phase at 298 K. The increased absorption in the tetragonal phase is due to the red shift of the band edge, which captures more of the laser spectrum.

4.5.3 Two-Dimensional Electronic Spectroscopy

Broadband laser pulses were prepared by pumping a homebuilt non-collinear optical parametric amplifier with a 1 kHz amplified Ti:Sapph laser (Coherent Inc., Astrella). The pulses were compressed to 80 fs using a pair of fused silica prisms, as measured via autocorrelation on a two-photon photodiode at the sample position. The beams were attenuated to achieve a fluence of 4.2 uJ/cm^2 for each pump beam and 0.9 uJ/cm^2 for the probe beam at the sample position.

The phase-stable two-dimensional electronic spectroscopy (2D-ES) experimental arrangement used in this work has been described elsewhere [66]. A combination of a beam splitter and diffractive optic were used to generate four beams in a box-car geometry. The waiting time delay T between pump and probe was controlled using a motorized delay stage, while the delay τ between the two pump pulses was controlled by translating 4-degree glass wedge pairs placed in the beam path. The four beams were focused to a $1/e^2$ diameter of 60 μm and carefully overlapped at the sample position. The signal was then emitted along the phase-matched direction, co-propagating with the attenuated local oscillator beam. The heterodyned four-wave mixing signal was detected in the frequency domain using a spectrometer (Princeton Instruments, Acton Advanced SP2300A) and CCD camera (Princeton Instruments, PIXIS 100). A linear phase correction corresponding to the time delay between the signal and local oscillator was added to generate the approximately phased spectra in Figure 2. Amplitude oscillations were measured using the absolute value spectra (see Figure 3) in order to rule out any possible artifact from the phasing procedure.

All spectra were taken using optical cryostats (Oxford Microstat He for Section 4.2-4.3, and Oxford Optistat DN for section 4.4) flushed with dry nitrogen to protect the samples from air and moisture. For low temperature experiments, samples were transferred directly into the nitrogen cryostat pre-cooled to 77K, and then slowly warmed to the desired temperature. The rapid cooling seems to prevent the formation of cloudy scattering domains during the phase transition.

The MAPI samples are much more scattering than a typical single crystal or nanocrystal solution, which poses a significant experimental challenge in 2D-ES. Two choppers and an

economical microcontroller (Arduino Uno) were used to dynamically remove undesired scattered light, especially the scattered probe interference with the local oscillator. This contribution is especially important to remove because the probe-local oscillator delay is nearly equal to the signal-local oscillator delay, so it is not easily removed using a time-domain window during the data processing. A detailed description of this scheme for significantly improving the signal-to-noise ratio can be found in Chapter 3 and Ref. [88] in which a frequency-resolved pump probe measurement was used for demonstration.

5 2D-ES of Exciton-Phonon Scattering and Electronic Couplings in Monolayer MoS_2

5.1 Introduction: Optoelectronic Properties of Monolayer MoS_2

Moore's law first predicted and then dictated (through self-imposed semiconductor industry roadmaps) that the processing capability of a chip doubles every two years. This was achieved by progressively shrinking the size of the silicon transistor (now less than 7 nm), but nanoscale effects such as quantum tunneling make this approach unsustainable. Future growth in computing power will require a new approach. Because thinner electronics consume less power and generate less heat, meaning still more transistors could be packed on a chip, an interest has arisen in devices using new atomically thin materials such as monolayer MoS_2 [167], [168]. The physics of an atomically thin semiconductor are very different than in bulk materials, and there remains much to study in their optoelectronic properties.

In contrast to the bulk material, photosynthetic complexes, and the perovskite material examined in previous chapters, charge carriers in a monolayer of the semiconductor MoS_2 experience weak dielectric screening and quantum confinement. With only two dimensions for carrier diffusion and a limited dielectric response from the surrounding material [169], carrier-carrier interactions are enhanced. This leads to strongly bound excitonic states (electron-hole pairs) [170] and non-negligible photo-induced many body effects [171], [172]. Moreover, whereas bulk MoS_2 has an indirect bandgap (requiring phonon participation for excitation or recombination) the monolayers have a direct band gap [173] and correspondingly efficient absorption and emission [174]. Due to the lack of inversion symmetry in the MoS_2 structure, degenerate direct-gap transitions occur within two momentum-space valleys, denoted K and K'. Circularly polarized light may be used to selectively excite in a single valley [175], while linear polarization excites in both. Within each valley, spin-orbit coupling in the valence band splits the transition into a pair of exciton resonances separated by about 150 meV. Therefore, using circular polarization and frequency together, spin-selective excitation is possible in monolayer MoS_2, and it might be useful for information processing and storage applications.

The two exciton peaks are shown in the linear absorption spectrum, Figure 5.1. We call the lower exciton XA, and the upper exciton XB. At low temperature the exciton resonances are narrow and a weak shoulder peak emerges to the red of XA. This peak is due to a tightly bound "trion" [176], a quasiparticle made from an exciton bound to either a hole or an electron. These quasiparticles are not usually found in bulk semiconductors, because their formation depends the weak dielectric screening and strong many body interactions in the monolayer. When a current is applied to introduce additional electrons, the trion population grows, resulting in a stronger trion absorption peak and a weaker XA peak [176]. Extensive trion formation leads to a negative photoconductivity [177], in which the charge mobility in the conduction band decreases by up to 70% as carrier density increases. This illustrates the strong influence that many-body interactions can have on the optoelectronic function in a 2D semiconductor.

When monolayers are treated with the superacid TFSI to passivate defects, 100% photoluminescence yield has been achieved [178]. This makes monolayer MoS_2 an attractive

material for making highly efficient LEDs, or as a material for optical information storage and retrieval. Figure 5.1 shows the photoluminescence spectrum on the monolayer, with a single peak slightly red of the lower exciton XA resonance. This implies that the efficient photoluminescence originates from the XA state, and excitations into XB or above emit only after relaxing to XA. The same result was found in the electroluminescence spectrum [179], [180].

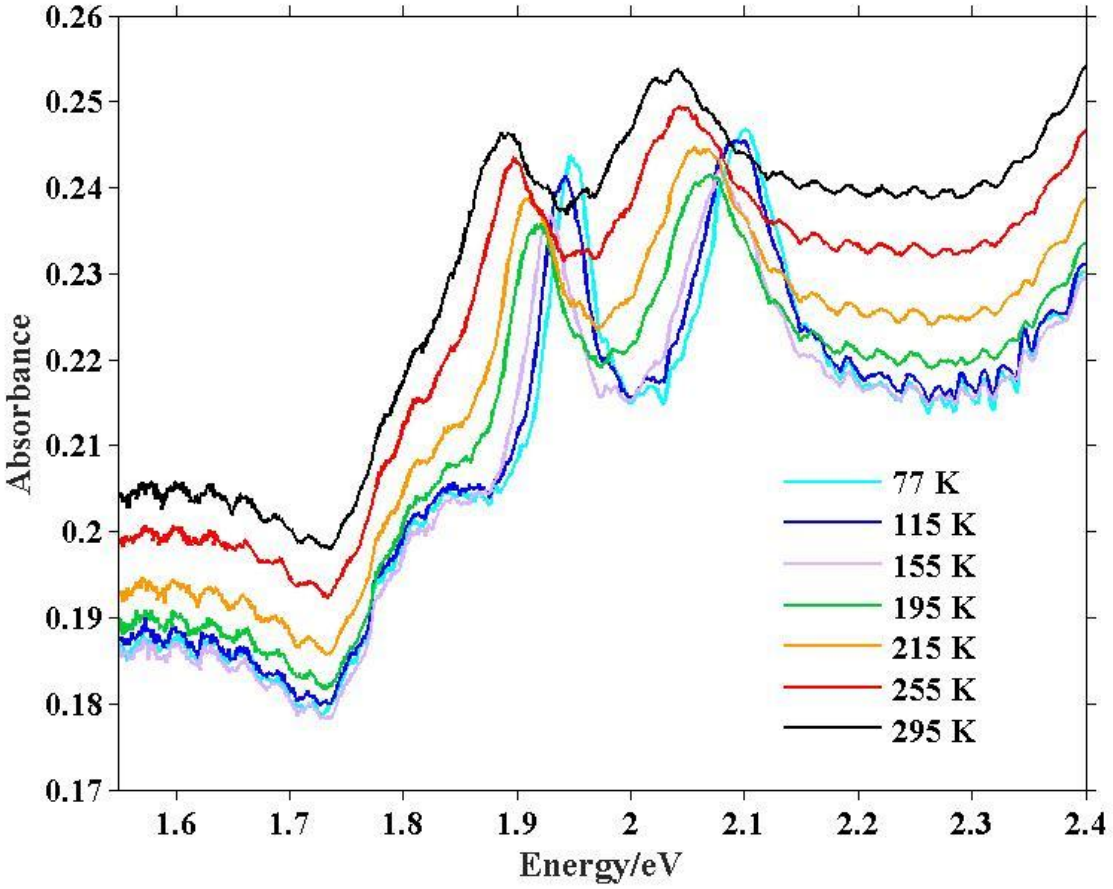

Figure 5.1 Linear absorption spectra of monolayer MoS_2 with temperature ranging from 77 K to 295 K.

In optoelectronic materials with photoluminescence yield < 100%, the loss of quantum efficiency is due to the existence of non-radiative recombination pathways. In non-radiative recombination, energy is dissipated to phonon degrees of freedom instead of light emission. In addition to reduced efficiency, non-radiative recombination causes undesirable heating in devices. In a direct-gap semiconductor, radiative recombination is much faster than non-radiative processes. However, momentum changes from an exciton-phonon interaction or defect scattering can populate indirect bandgap states with a slow radiative rate, allowing non-radiative pathways to compete with light emission.

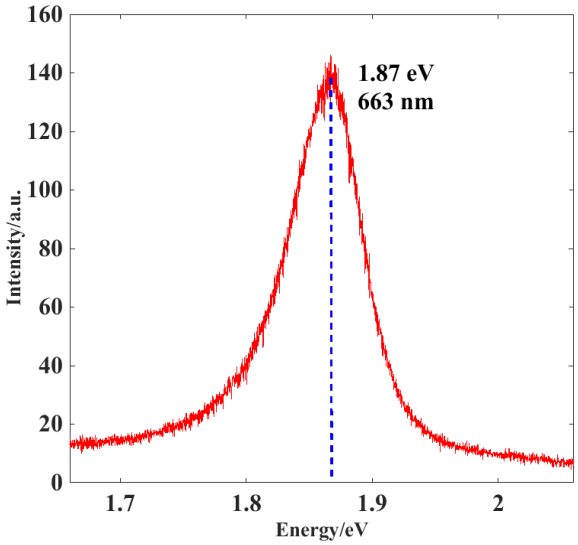

Figure 5.2 Photoluminescence spectrum of monolayer MoS_2 excited at 473 nm. The single emission peak is at 663 nm (1.87 eV).

In order to gain a complete picture of the kinetics leading to efficient photoluminescence, it is therefore important to measure the intrinsic exciton lifetime (the average time before a scattering interaction). Here we have used 2D electronic spectroscopy to isolate the intrinsic lifetime from the effects of ensemble broadening.

Furthermore, in the conventional Wannier-Mott model for delocalized semiconductor excitons, XA and XB are uncoupled because the transitions involve carriers of opposite spin. Using 2D spectroscopy we are able to measure sub-picosecond transient interactions that nonetheless occur between the two states. Our observations agree with first-principles GW-BSE calculations (performed in collaboration with Professor Steven Louie's group at Berkeley) that show significant exchange interactions between XA and XB in the ultrafast transient regime.

5.2 Exciton-Phonon Scattering and the Temperature Dependent 2D Lineshape

The width of the linear absorption peaks in Figure 5.1 depends on a combination of the excited state dephasing lifetime (the homogeneous linewidth) and the ensemble broadening (the inhomogeneous width). As the sample is cooled, fewer phonons are thermally populated, so that exciton-phonon scattering decreases and the excited state lifetime is extended. By examining the dependence of the homogeneous linewidth on temperature, one can determine which phonons most strongly interact with the exciton. A simple model separates the linewidth temperature dependence into a linear term due to interactions with acoustic phonon scattering and Bose-Einstein terms due to interactions with thermally populated optical phonons with frequencies ω_i:

$$\Gamma(\mathrm{T}) = \Gamma_0 + a\mathrm{T} + \sum_{\omega_i} \frac{b_i}{\exp\left(\frac{\hbar\omega_i}{k_B\mathrm{T}}\right) - 1}$$

Equation 5.1

Acoustic phonons are compression waves in the crystal lattice, while the higher energy optical phonons involve the motion of oppositely charged Mo and S in opposite directions. As such, optical phonons tend to couple more strongly to charge excitations (and to infrared light, hence their name). Therefore, a sharp increase in linewidth is can be expected as the lowest optical phonon becomes populated.

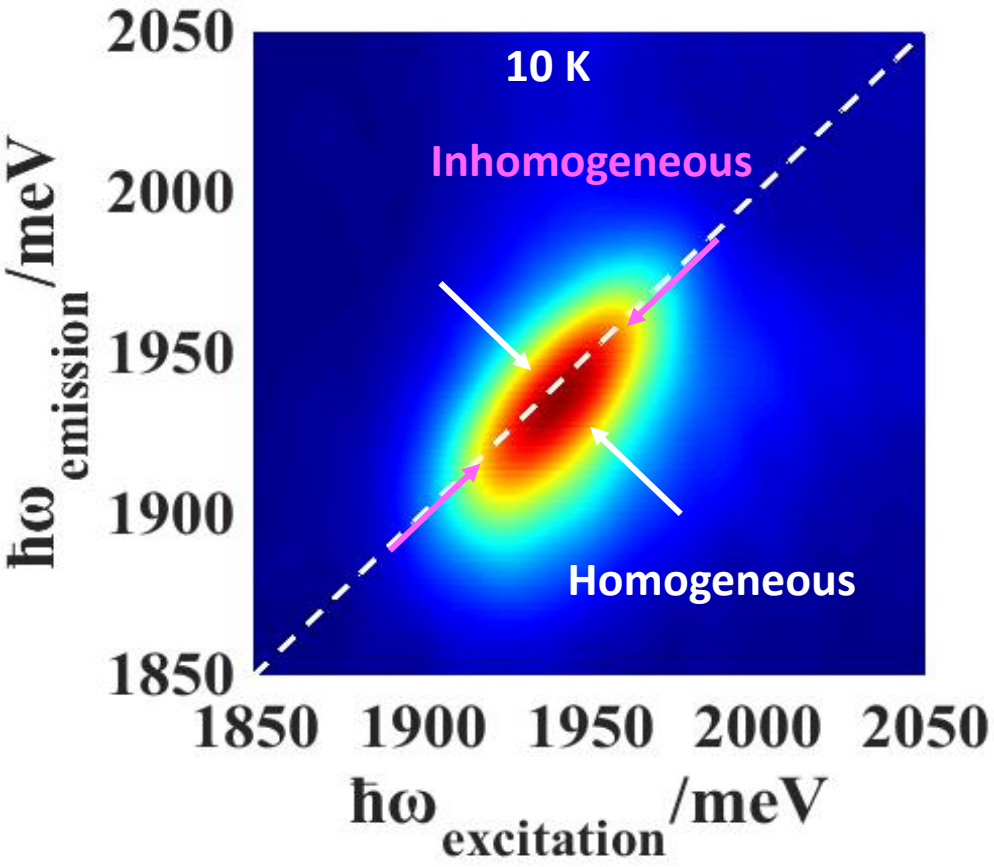

Figure 5.3 Total 2D spectrum of monolayer MoS_2 Exciton A at $t_2 = \sim 100$ fs and temperature 10 K. The antidiagonal width measures the homogeneous (intrinsic) linewidth, while the diagonal width measures the inhomogeneous broadening.

However, because the homogeneous and inhomogeneous widths are not easily separated, this information is not easily obtained from linear absorption spectra. One solution is to perform saturation-absorption or "hole-burning" experiments [181], in which a narrowband laser selectively bleaches a portion of the ensemble and causes a spectral hole in a subsequent broadband linear absorption spectrum. If the homogeneous linewidth is small compared to the inhomogeneous broadening, then the hole width measures the inverse dephasing lifetime. However, because the hole-burning technique lacks time resolution, the presence of ultrafast dynamics can complicate its interpretation. Photon echo spectroscopies, like 2D-ES, can provide a time-resolved deconvolution of the inhomogeneous and homogeneous widths, overcoming this

drawback. In Section 3.3 (see Figure 3.13) we showed the vanishing difference between the diagonal and anti-diagonal 2D linewidths with waiting time, due to rapid configuration exchanges in an ensemble of dye molecules in solution. Here we measure the anti-diagonal 2D linewidth of Exciton A at early waiting time and over a range of temperatures in order to identify the phonons responsible for exciton-phonon scattering.

First we obtained 2D spectra of MoS_2 monolayers using linearly polarized pulses compressed to ~40 fs and covering only the XA resonance. Figure 5.3 shows the total 2D spectrum of the Exciton A lineshape at waiting time $t_2 = \sim 100$ fs and temperature 10 K. The diagonally elongated peak shows that XA is inhomogeneously broadened. We quantitatively extracted the homogeneous linewidth according to a square lorentzian fitting method described by Siemens et al. [182]. Owing to the long coherence times in MoS_2, the rephasing portion of the 2D spectrum is much larger than the non-rephasing. Therefore, in order to avoid truncation artifacts from removing the $t_1 < 0$ non-rephasing portion, we analyzed the total spectrum and assume the contribution of the non-rephasing portion to the lineshape is negligible.

We took early-time 2D spectra at temperatures ranging from 10 K to 190 K, and plot the homogeneous width Γ in Figure 5.4:

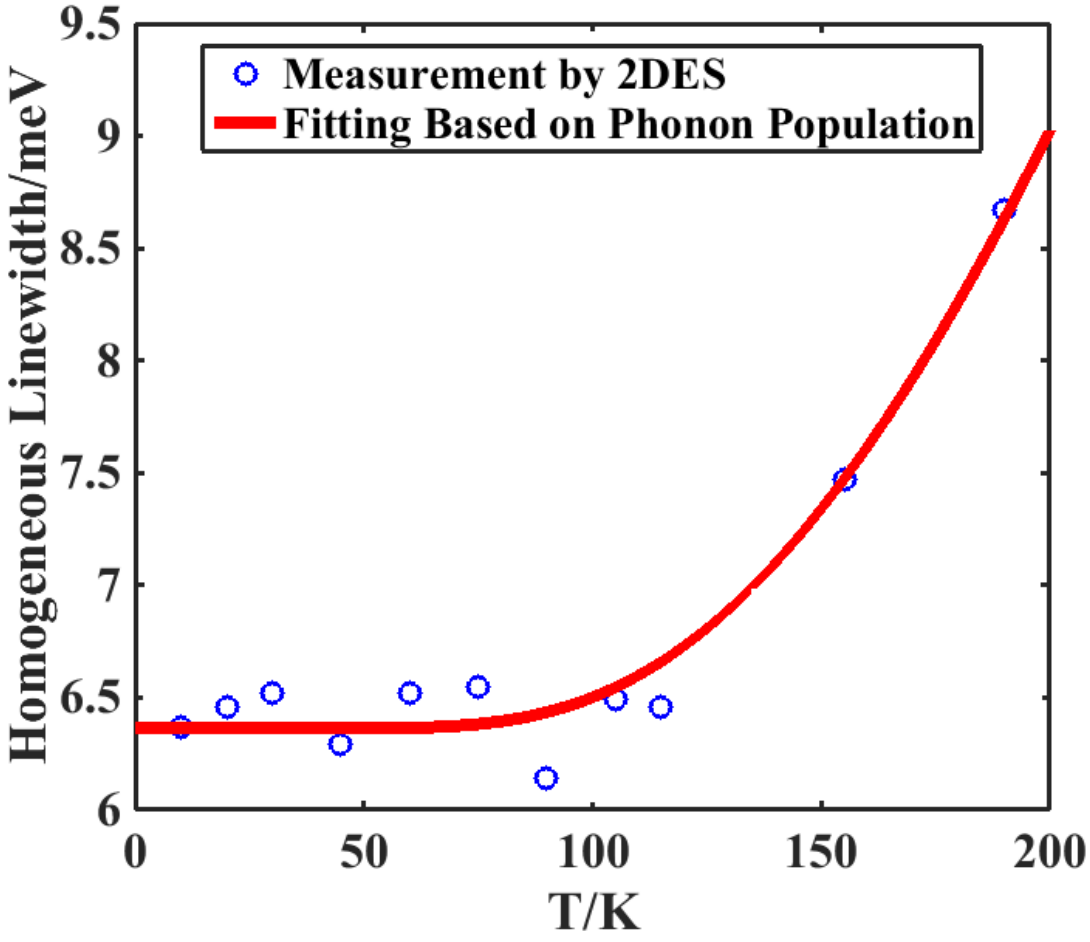

Figure 5.4 Anti-diagonal widths of low temperature 2D spectra (blue circles) and plot of Equation 5.1 (red), using $a = 0$, $b = 45.76$ meV, $\Gamma_0 = 6.36$ meV and $\omega_{LO} = 50$ meV.

At low temperature, Γ is approximately constant with $\Gamma_0 = 6.36$ meV, which gives an exciton dephasing time of about 650 fs. The absence of a linear broadening at low temperature ($a \approx 0$) implies that scattering interactions between the exciton and low energy acoustic phonons are negligibly weak. Using Equation 5.1 we find that we can get a very good agreement with the temperature dependent linewidth data (red line in Figure 5.4) considering a single longitudinal optical phonon with $\omega_{LO} = 50$ meV. This frequency is in good agreement with the energy of the lowest lying optical phonon states in a calculated phonon dispersion curve for the MoS_2 monolayer [183]. Our result implies that, in this sample, Exciton A scatters most strongly with phonons around 50 meV on the ultrafast timescale, and couples very weakly to acoustic phonons.

5.3 Electronic Coupling and Many-Body Effects

Next we generated more broadband ultrafast pulses (Figure 5.5, blue) that cover both the XA and XB resonances at 40 K (Figure 5.5, red). We used 2D-ES to investigate many-body interactions and exciton couplings in the excited state. Similar 2D-ES experiments have previously observed the exciton-trion coupling in $MoSe_2$ [184], [185]. Quarter waveplates were inserted to make co-circularly polarized pump and probe pulses.

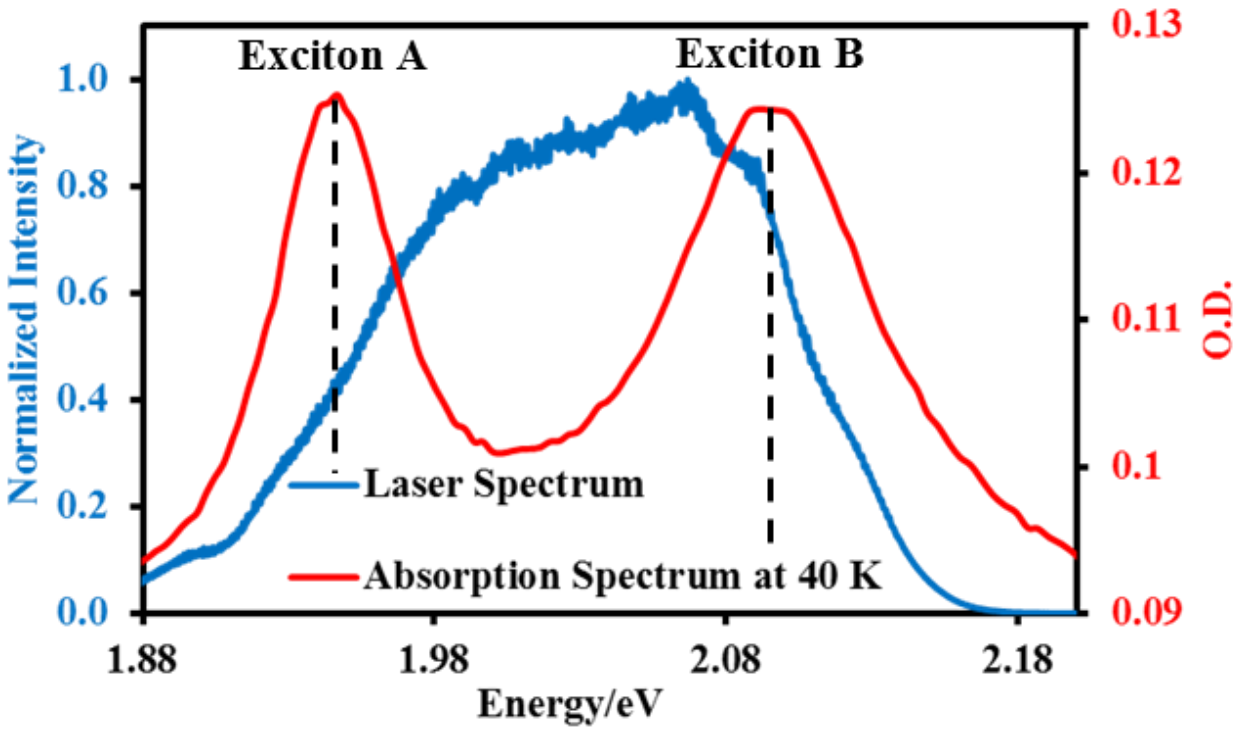

Figure 5.5 Laser spectrum (blue and left vertical axis) and absorption spectrum of monolayer MoS_2 at 40 K (red and right vertical axis).

The circularly polarized light selectively generates excitons in a single K-valley, ensuring that XA and XB observed involve electrons with opposite spins. Helicity-resolved pump-probe

measurements show that, depending on excitation density [186] this valley polarization may decay in less than 10 ps even at low temperature [187], [188]. However, for shorter waiting time we can be confident that any population exchange or interactions we measure are between excitons with the same momentum but opposite spin.

Linear absorption spectra with continuous-wave (CW) excitation accesses quasi-static states populated in proportion to their oscillator strength. Ultrafast pulses, however, generate nonstationary states whose evolution yields information about interactions between photo-excited excitons (see the discussion in Section 1.5). After excitation, the coherence terms in Equation 1.6 are gradually lost under the influence of open-system environmental fluctuations. The system has then collapsed into a combination of uncoupled eigenstates (although fluctuations continue to induce population relaxation until a thermal equilibrium distribution is reached).

Figure 5.6 shows time-resolved 2D spectra covering both exciton resonances at 40 K:

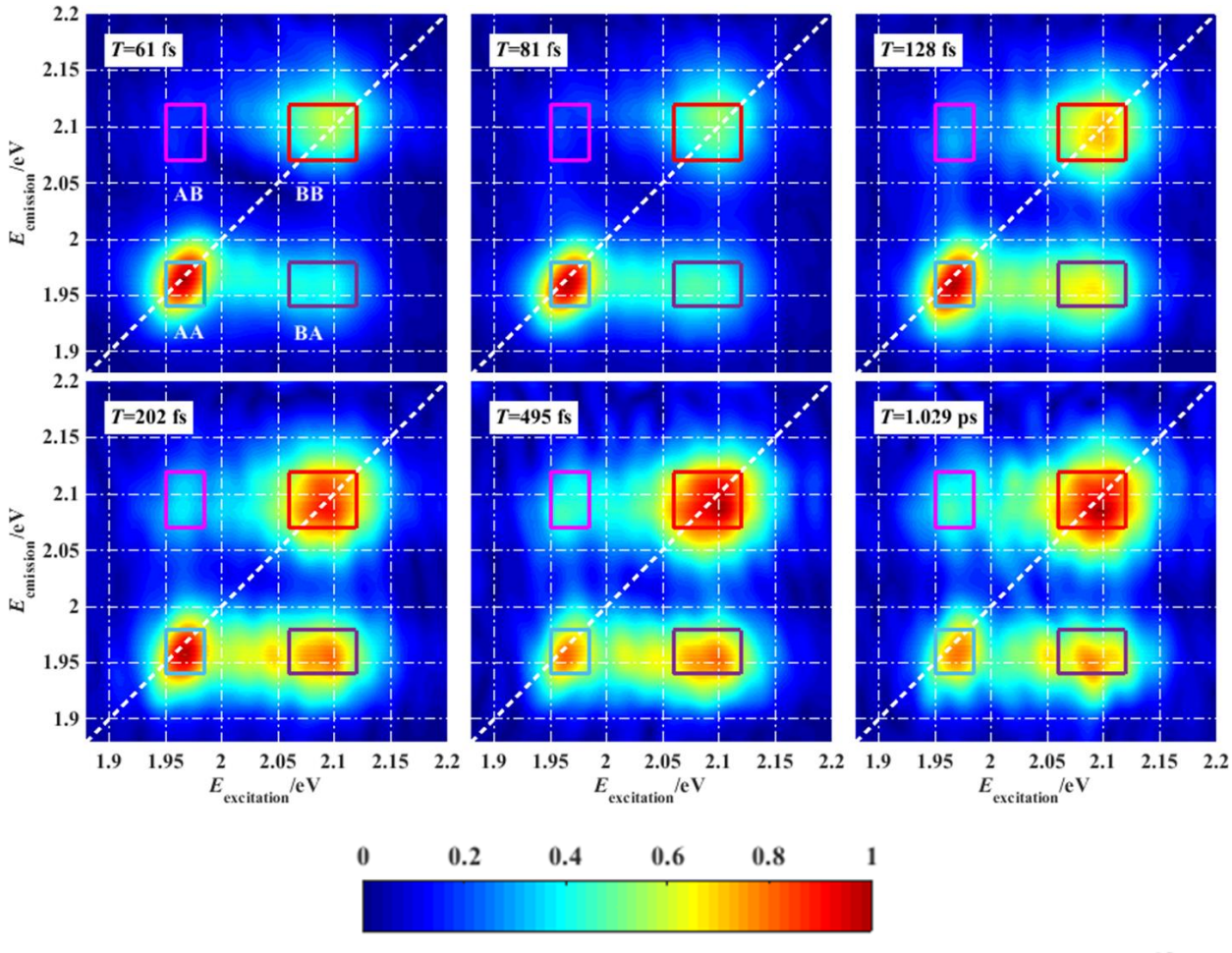

Figure 5.6 Broadband 2D-ES of MoS_2 monolayers at selected waiting times (T = 61, 81, 128, 202, 495 fs and 1.029 ps). The pump fluence was 5 μJ/cm^2. Four peaks are labeled in the T = 61 fs plot: diagonal peaks AA and BB, upper cross-peak AB and lower cross-peak BA. Peak regions are defined by colored squares (AA=blue, BB=red, AB=pink BA=purple).

Each spectrum shows two diagonal peaks corresponding to the XA and XB resonances, a lower cross-peak, and a weak upper cross-peak. The diagonal peaks indicate ground state bleaching and stimulated emission due to excitation of each individual interband transition. Both diagonal peaks decay monotonically with waiting time (despite normalization causing an apparent increase in the BB diagonal peak). The cross peaks correspond to excitation resonant with XA (XB) followed by emission from a third-order polarization resonant with XB (XA). In previous studies of semiconductors [184], [189], [185], the presence of such cross peaks in 2D spectrum has been attributed to excitation-induced shift (EIS) of the resonance energy and excitation induced dephasing (EID) of the electronic polarization caused by Coulombic interactions. EIS results when Coulombic interactions raise or lower the energy of states in the conduction band, changing the energy of interband transitions. EID occurs when many-body scattering interactions decrease the excited state dephasing lifetime, increasing the homogeneous width of subsequent transitions. Figure 5.7 illustrates how EID/EIS generate cross-peaks by creating an offset between ground state bleach (positive) and excited state absorption (negative) signals. This is a specific case of the correlated transitions discussed in Section 1.3 and references therein.

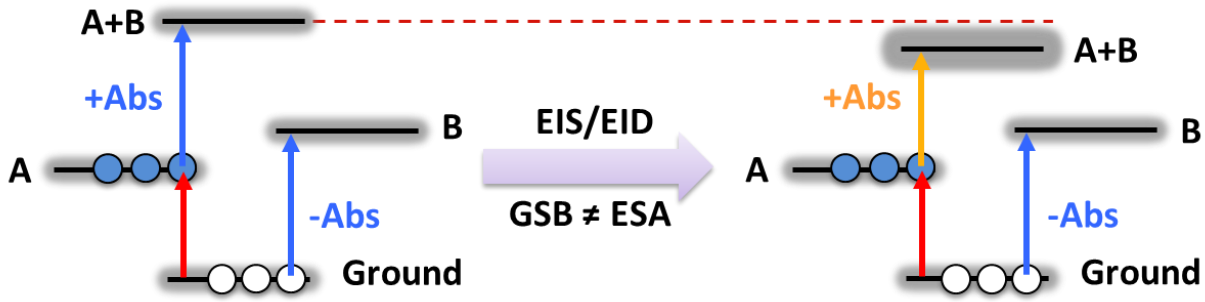

Figure 5.7 Effects of EIS and EID on transient absorption in a four-level system. Left: absent excited state many-body interactions (EIS/EID), excited state absorption (ESA) from A to A+B is identical (but for sign) to the bleaching signal for the transition from ground to B (GSB). The two signals cancel perfectly, and no correlation cross-peak is measured. Right: with EIS/EID, the A+B state is broadened and/or shifted by many-body Coulomb interactions. As pictured, the ESA signal would appear to the red of the GSB near the B transition energy, giving a twin peak in an absolute-value spectrum. A broadened negative ESA would also have lower amplitude, so that more of the positive GSB peak would emerge.

In the EIS/EID picture described in Figure 5.7, the amount of peak shift and broadening increases with the total excited state population because it is interactions with that population that generate the effect. Therefore, the upper cross-peak AB should reach its maximum amplitude at early waiting time, when the population of XA is largest, and then decay together with the diagonal peak AA. However, in our observations the dynamics of the cross peak AB deviate from this prediction. It is clear from Figure 5.6 that the AB cross-peak is quite dark for T=61 fs and grows brighter (relative to the diagonal peak AA) with increasing waiting time.

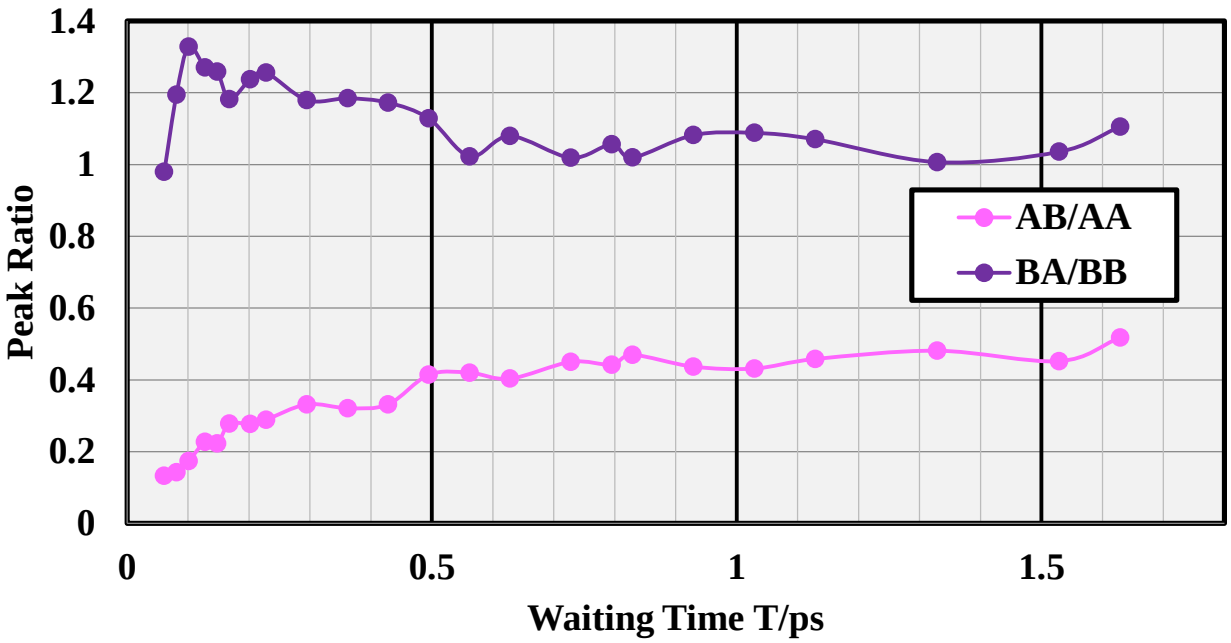

Figure 5.8 Ratio of cross-peak to diagonal peak amplitudes integrated over the boxed regions in the previous Figure 5.6. The upper cross-peak AB/AA is marked in pink and the lower cross-peak BA/BB in purple.

The amplitude of cross-peak AB (BA) relative to that of the diagonal peak AA (BB) is plotted in Figure 5.8. Constant peak ratios for T > 600 fs indicate both cross-peaks decay commensurately with the corresponding excited state population. For T < 600 fs, the lower cross-peak BA decays faster than the BB diagonal peak (as evidenced by a decreasing BA/BB ratio, purple). This indicates that at short waiting times the lower cross-peak is primarily the result of many-body interactions (EIS/EID), not population relaxation. By contrast, the upper cross-peak AB does not decay with the diagonal peak AA (the AB/AA ratio increases). Because this observation runs counter to the EIS/EID model for cross-peaks, it implies the AB peak may have a component due to population up-conversion from A to B.

Phonon-assisted population up-conversion, which has been previously observed spanning the smaller energy gap (Δ = 20-30 meV) between a trion and exciton in monolayer $MoSe_2$ and WSe_2 [184], [185], [190] can be ruled out here since phonons populated at 40 K (k_BT = 3.4 meV) can hardly surmount the energy gap between XA and XB, $\Delta_{AB} = 150$ meV. Because the AB peak amplitude depends only weakly on fluence (Figure 5.9), we can also rule out an Auger process, in which two XA interact to yield a photon and one XB.

To explain our experimental results, we turn to calculations of the many-body interactions based on first-principles GW-BSE. Preliminary results from these calculations, performed by Meng Wu, Ting Cai, and Professor Steven Louie at Berkeley, predict population conversion from XA to XB due to an exchange interaction of approximately $K_{AB} = 10$ meV. Exchange interactions are a consequence of Pauli repulsion between identical fermions (electrons or holes in the conduction or valence band, respectively). This interaction is effectively a coupling between the XA and XB states, which have opposite spin and are populated by a direct interband transition.

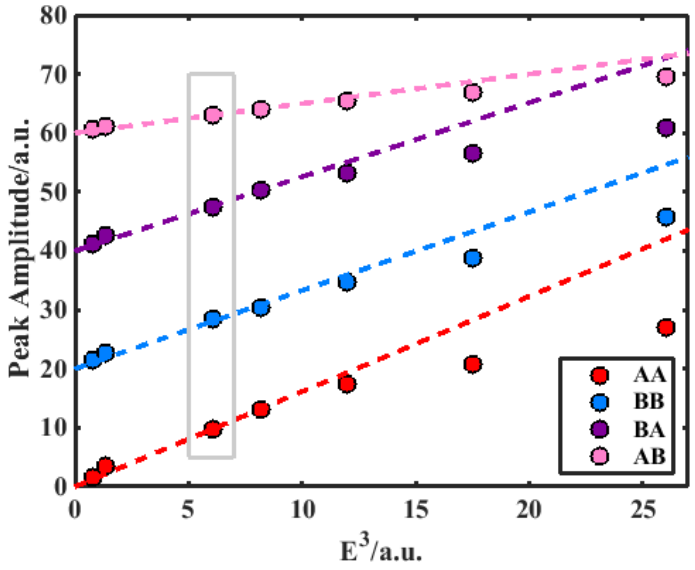

Figure 5.9 Dependence of 2D-ES signal on pulse field amplitude cubed. Seven different pulse fluences were used: 1.0, 2.0, 5.0, 6.3, 8.0, 10, and 13 μJ/cm^2. The amplitudes of the four peaks, AA, BB, BA, and AB, are marked by blue, red, purple, and pink dots while the dashed lines illustrate the linearity versus E^3 at low fluence and the deviation from linearity at high fluence. The grey box marks the fluence used for measurements in Figures 5.6 and 5.8. Note the weak and linear fluence dependence of AB, which rules out a higher-order Auger mechanism for XA to XB up-conversion.

The true system eigenstates will then be a mixture of XA and XB, and are not purely spin- and valley-polarized. Equivalently, one can say the state that couples to the laser excitation (XA or XB) is a coherent superposition of the system eigenstates. Therefore, if the initially prepared state evolves coherently, then there is some amount of spin flipping and population transfer from XA to XB. The Rabi frequency for this coherent evolution is $\Omega_{AB} = \sqrt{K_{AB}^2 + \Delta_{AB}^2} \approx \Delta_{AB}$, so that the half-period timescale for initial coherent population transfer is on the order of 10 fs. Of course, when the Rabi cycle is completed, this population transfer is reversed. Irreversible population transfer is only achieved through decoherence of the initial state through the influence of the environment (i.e. phonons).

At the time of this writing, the theory and experimental analysis remain in progress. The coherent spin-flip and population transfer, which we tentatively propose here to explain the upper cross-peak dynamics in our 2D-ES data, requires the participation of phonons for decoherence but not for momentum nor energy conservation. Similar to the "quantum ratchet" mechanism conjectured for photosynthetic energy transfer [26], [27], coherent evolution and subsequent decoherence results in a net uphill population transfer that is faster than the thermally activated process.

5.4 Experimental Methods

Monolayer MoS_2 (~10 mm^2, polycrystalline) was grown by chemical vapor deposition on a sapphire substrate, and was characterized by photoluminescence (Figure 5.2) and Raman spectra.

We were able to use the same sample for months of experiments with no observable damage or degradation, consistent with the excellent stability of this material seen under much more extreme photoexcitation [191]. The broadband laser pulses used for 2D-ES (Fig. 5.5) were generated by a home-built noncollinear optical parametric amplifier (NOPA) driven by a Ti:sapphire amplifier. During experiments, the sample was mounted in a cold-finger cryostat (Oxford Microstat He) cooled by liquid helium. 2D-ES spectra were obtained using the experimental arrangement described in Section 3.2 and in Chapter 4.

6 Perspective and Future Directions

The work in this dissertation provides a few examples of the importance of electron-phonon interactions to understanding the dynamics of light-induced energy transport in a diverse selection of materials and contexts. Although electronic energy transport occurs on an ultrafast timescale, this does prevent nuclear motion and environmental fluctuations from impacting the light-harvesting process or subsequent emission pathways. As such, models for these processes must be carefully chosen to avoid imposing a convenient but unphysical separation of timescales. Diversification of optoelectronic materials for photovoltaics, LEDs, nano-lasers, and phototransistors beyond the conventional variations on crystalline silicon provides an opportunity for electron-phonon interactions in the ultrafast regime to be exploited in new ways. Phonon engineering, already applied to optimize thermoelectrics, will become an important aspect of all electronics based on soft materials. Here we have discussed such concepts as vibronic resonances, electron-phonon scattering, phonon cooling bottlenecks, and polarons and dielectric screening. Developing semiconductors that exploit these processes requires the union of ultrafast spectroscopy with traditional materials characterization techniques and theoretical models.

Methylammonium lead iodide will never be widely used in solar cells, because it is both toxic and thermodynamically unstable. But this material, with its puzzlingly spectacular performance, can still teach us the design principles that might lead to a new class of cheap and efficient photovoltaics. In a recent perspective [192], Zhu and co-workers suggested that the coupling to the 0.9 THz mode found in our 2D-ES experiment (Chapter 4) might be the large polaron, which they argue is responsible for both slow carrier recombination and persistent hot carriers. A phonon bottleneck effect on hot carrier cooling strengthens with increasing excitation density, but a polaron shielding effect weakens when the polarons begin to overlap (when $n_0 = 10^{18}$ cm^{-3}) [193]. The decrease in hot electron population with excitation density up to 10^{18} cm^{-3} [155] implies a polaron shielding model explains hot carriers better than a bottleneck mechanism in this density regime. While our work shows strong coupling to an isolated phonon, this constitutes direct measurement of neither a polaron, nor a phonon bottleneck. Such direct measurements are difficult, but instrumental in settling the question of why charge carriers in MAPI cool slowly.

Observing a hot phonon bottleneck directly requires showing a carrier density dependent phonon population is out of equilibrium with the temperature of the surrounding lattice, and that the timescale for this phonon relaxation is similar to that for hot carrier cooling. In recent weeks, Kim et al. [194] reported a THz pump, visible probe experiment that confirms the strong coupling between electronic transitions and modes near 1 THz. Transient absorption measurements with a THz pre-pump could show the effect of populating specific phonon modes on hot carrier cooling. A visible pump, THz probe experiment could then measure phonon relaxation times in the presence of charge carriers, and identify whether a bottleneck mode is indeed populated out of equilibrium with other low-frequency modes.

Observing a polaron state directly requires high energy resolution, because the polaron formation energy is on the order of 0.1 eV [155]. Signatures attributed to the polaron have been found in time-resolved photoelectron [155] and nanosecond TA [195] experiments. However,

given the amount of energetic disorder in MAPI films, energy-resolved measurements can be difficult to interpret. How can we tell the difference between polarons that form everywhere in a film and a low-lying band-edge population due to different local structure? Or between persistent hot carriers and local sample heating? Recently, Huang and co-workers used ultrafast transient absorption microscopy (TAM) to observe charge transport in MAPI with 50 nm spatial resolution and 300 fs time resolution [196]. Similar experiments performed by Nah et al. [197] expose a large range of hot carrier cooling times due to inhomogeneity. These papers highlight the need for spatial resolution in future studies on MAPI. Microscopy setups are likely the best way to achieve such resolution, but heterojunctions and interfaces might also be used to generate signals with frequency and/or dynamics distinct from the bulk. The nanosecond TA work by Yang et al. [195] on a heterojunction between perovskite and a charge transport material is interesting from this perspective because states at the heterojunction can be selectively excited. Therefore, carriers are injected into a specific region of the film with distinct structural properties no doubt influenced by the interfacing material. In another unconventional spatially resolved study, Wong et al. used the polarization dependence of TAM spectra to isolate signals coming from grain boundaries in a polycrystalline TIPS-pentacene film [198]. With materials as disordered as hybrid perovskites, bulk measurements may miss the full picture, and future studies should focus on spatial resolution.

While multijunction solar cells using materials with different band gaps might be more practical than developing a hot carrier solar cell [199] using a single material, slow hot carrier cooling could be beneficial to all photovoltaics. Hot carriers have more kinetic energy, and therefore move faster in between scattering events. The TAM study by Huang and co-workers showed that in MAPI, ballistic charge transport indeed increases with excess carrier energy [196]. Extending this period of ballistic transport can greatly increase overall charge mobility in a material, allowing thicker films to be used and more light to be harvested. In order to design hot-carrier materials, it would be useful to develop fast, standardized measurements of hot carrier lifetime. 2D spectroscopy, while detailed, has the drawback of a complicated setup and relatively long experimental time. It would be better to standardize the use the photo-induced absorption signal [196] [197] to measure of carrier temperature. Similar to the TA snapshot technique recently developed in our group [200], a rapid measurement at a single waiting time and probe frequency could continuously monitor the carrier cooling properties in a sample. Such a simplified technique could then be applied to rapidly evaluate the effect of pump fluence, temperature, current, strain, and other variables in a sample. In a microscope, snapshot TA could also map hot carriers across the inhomogeneous sample.

Turning now to monolayer MoS_2, the work presented here highlights the importance of transient carrier-carrier coupling and of the 50 meV optical phonon in the dynamics leading to highly efficient emission. The many-body effects we observe are due to the weak dielectric screening in a monolayer. By the same token, optoelectronic properties in monolayer MoS_2 are very sensitive to interactions with the substrate [169]. This presents both a challenge in generating repeatable measurements, and an opportunity to explore tunable functionality and sensing capabilities. The substrate or an adjacent material layer can tune the dielectric constant through orbital overlap with the monolayer. Alternatively, a substrate can provide phonons or surface plasmons [201] that interact with charge carriers in the adjacent MoS_2 monolayer. Recently, a thin ionic liquid layer was used to screen charged defects and increase photoluminescence yield [202]. By using substrate to increase the environmental influence on excitations, it might even be possible to create dressed charge carriers similar to the polarons

seen in perovskite. The ultrafast dynamics, many-body couplings, and 2D lineshapes will measure the mechanisms through which such modifications control the optoelectronic function. Understanding the effect of adjacent materials on MoS_2's electronic response may also allow the monolayers to be used as a sensitive sensor detecting chemicals [203] and measuring surface characteristics.

2D-ES studies today are largely confined to studying molecules and materials, not devices *in operando*, because they demand a transmissive sample. In the spirit of 2D-FDCS described in Chapter 3, alternative detections schemes can be developed. Besides fluorescence or photoluminescence, photocurrents or photoconductivity (2DPC) [204] can be used to report an excited state population. By using the output of a device to report on the ultrafast dynamics in its component materials, future work on the role of electron-phonon interactions in optoelectronics can be extended to reflect physics in real devices.

Finally, a brief comment on the role of vibrations and vibronic coherences in photosynthesis: as our simulations demonstrate (Chapter 2), even the small vibronic couplings found in chlorophyll and bacteriochlorophyll can generate 2D-ES signatures that might be mistaken for pure electronic coherence. Aside from this measurement problem, resonances between vibrations and electronic energy gaps can have a large impact on coherence and energy transfer, as long as the environmental fluctuations are not too strong. Like the large charge mobility advantage gained from ballistic transport of hot carriers, coherent electronic transport extended through vibronic resonance mechanisms can provide a distinct advantage [40]. This raises the question of whether nuclear vibrations are actually used to tune function in the photosynthetic apparatus. For example, it has been proposed that the regulatory light-harvesting protein LHCSR undergoes a conformational change to switch between light-harvesting and quenching functions [205]–[207]. Is this switch in function fully explained by a changing chlorophyll separation, or can chlorophyll-protein interactions also affect a sensitive vibronic control mechanism? Although very challenging, we could begin to investigate this question using 2D-ES to measure changes in electronic couplings and 2D electronic-vibrational spectroscopy (2D-EV) to compare the energy transferred to vibrations in the two conformations.

It wasn't so long ago that we didn't know the structure of a light harvesting complex. Solar cell technology and even computing are still in their early generations, very much influenced by founding inventions and only beginning to sample the large space of technological variations. As we improve our fundamental understanding of nanoscale and ultrafast physics in real-world and untidy materials, we clear the way for technologies to mature.

References

[1] C. A. S. Hall and K. A. Klitgaard, *Energy and the Wealth of Nations: Understanding the Biophysical Economy*. New York: Springer, 2012.

[2] International Energy Agency, *World Energy Outlook 2016*. 2016.

[3] N. S. Lewis and D. G. Nocera, "Powering the planet: Chemical challenges in solar energy utilization," *PNAS*, vol. 103, no. 43, pp. 15729–157345, 2006.

[4] M. Schlosshauer, "Decoherence, the measurement problem, and interpretations of quantum mechanics," *Rev. Mod. Phys.*, vol. 76, no. 4, pp. 1267–1305, 2005.

[5] T. Brixner, J. Stenger, H. M. Vaswani, M. Cho, R. E. Blankenship, and G. R. Fleming, "Two-dimensional spectroscopy of electronic couplings in photosynthesis.," *Nature*, vol. 434, no. 7033, pp. 625–628, 2005.

[6] R. A. J. Janssen and J. Nelson, "Factors Limiting Device Efficiency in Organic Photovoltaics," *Adv. Mater.*, vol. 25, no. 13, pp. 1847–1858, 2013.

[7] W. S. Yang, B. Park, E. H. Jung, N. J. Jeon, Y. C. Kim, D. U. Lee, S. S. Shin, J. Seo, E. K. Kim, J. H. Noh, and S. Il Seok, "Iodide management in formamidinium-lead-halide – based perovskite layers for efficient solar cells," *Science*, vol. 356, no. 6345, pp. 1376–1379, 2017.

[8] M. Cai, Y. Wu, H. Chen, X. Yang, Y. Qiang, and L. Han, "Cost-Performance Analysis of Perovskite Solar Modules," *Adv. Sci.*, vol. 4, no. 1, 2017.

[9] A. Ishizaki and G. R. Fleming, "Unified treatment of quantum coherent and incoherent hopping dynamics in electronic energy transfer: Reduced hierarchy equation approach," *J. Chem. Phys.*, vol. 130, no. 23, p. 234111, 2009.

[10] M. Cho, T. Brixner, I. Stiopkin, H. M. Vaswani, and G. R. Fleming, "Two dimensional electronic spectroscopy of molecular complexes," *J. Chinese Chem. Soc.*, vol. 53, pp. 15–24, 2006.

[11] N. F. Scherer, D. M. Jonas, and G. R. Fleming, "Femtosecond wave packet and chemical reaction dynamics of iodine in solution: Tunable probe study of motion along the reaction coordinate," *J. Chem. Phys.*, vol. 99, no. 1, pp. 153–168, 1993.

[12] D. M. D. M. Monahan, L. Whaley-Mayda, A. Ishizaki, and G. R. G. R. Fleming, "Influence of weak vibrational-electronic couplings on 2D electronic spectra and inter-site coherence in weakly coupled photosynthetic complexes," *J. Chem. Phys.*, vol. 143, no. 6, 2015.

[13] H. Van Amerongen, L. Valkunas, and R. van Grondelle, *Photosynthetic Excitons*. World Scientific, 2000.

[14] Y.-C. Cheng and G. R. Fleming, "Dynamics of light harvesting in photosynthesis.," *Annu. Rev. Phys. Chem.*, vol. 60, pp. 241–262, 2009.

[15] G. S. Engel, T. R. Calhoun, E. L. Read, T.-K. Ahn, T. Mancal, Y.-C. Cheng, R. E. Blankenship, and G. R. Fleming, "Evidence for wavelike energy transfer through quantum coherence in photosynthetic systems.," *Nature*, vol. 446, no. 7137, pp. 782–786, 2007.

[16] T. R. Calhoun, N. S. Ginsberg, G. S. Schlau-Cohen, Y.-C. Cheng, M. Ballottari, R. Bassi, and G. R. Fleming, "Quantum coherence enabled determination of the energy landscape in light-harvesting complex II.," *J. Phys. Chem. B*, vol. 113, no. 51, pp. 16291–5, 2009.

[17] G. S. Schlau-Cohen, A. Ishizaki, T. R. Calhoun, N. S. Ginsberg, M. Ballottari, R. Bassi, and G. R. Fleming, "Elucidation of the timescales and origins of quantum electronic coherence in LHCII," *Nat. Chem.*, vol. 4, no. 5, pp. 389–395, 2012.
[18] S. Westenhoff, D. Paleček, P. Edlund, P. Smith, D. Zigmantas, D. Palecek, and D. Paleček, "Coherent picosecond exciton dynamics in a photosynthetic reaction center, Supplementary material," *J. Am. Chem. Soc.*, vol. 134, no. 40, pp. 16484–16487, 2012.
[19] F. D. Fuller, J. Pan, A. Gelzinis, V. Butkus, S. S. Senlik, D. E. Wilcox, C. F. Yocum, L. Valkunas, D. Abramavicius, and J. P. Ogilvie, "Vibronic coherence in oxygenic photosynthesis.," *Nat. Chem.*, vol. 6, no. 8, pp. 706–11, 2014.
[20] E. Romero, R. Augulis, V. I. Novoderezhkin, M. Ferretti, J. Thieme, D. Zigmantas, and R. van Grondelle, "Quantum coherence in photosynthesis for efficient solar-energy conversion," *Nat. Phys.*, vol. 10, no. 9, pp. 676–682, 2014.
[21] E. Collini, C. Y. Wong, K. E. Wilk, P. M. G. Curmi, P. Brumer, and G. D. Scholes, "Coherently wired light-harvesting in photosynthetic marine algae at ambient temperature," *Nature*, vol. 463, no. 7281, pp. 644–647, 2010.
[22] G. Panitchayangkoon, D. Hayes, K. a Fransted, J. R. Caram, E. Harel, J. Wen, R. E. Blankenship, and G. S. Engel, "Long-lived quantum coherence in photosynthetic complexes at physiological temperature.," *Proc. Natl. Acad. Sci. U. S. A.*, vol. 107, no. 29, pp. 12766–12770, 2010.
[23] A. Chenu and G. D. Scholes, "Coherence in Energy Transfer and Photosynthesis," *Annu. Rev. Phys. Chem.*, vol. 66, no. 1, pp. 69–96, 2015.
[24] S. F. Huelga and M. B. Plenio, "Vibrations, Quanta and Biology," *Contemp. Phys.*, vol. 54, no. 27 June, pp. 181–207, 2013.
[25] A. Ishizaki and G. R. Fleming, "Quantum Coherence in Photosynthetic Light Harvesting," *Annu. Rev. Condens. Matter Phys.*, vol. 3, no. 1, pp. 333–361, 2012.
[26] S. Hoyer, A. Ishizaki, and K. B. Whaley, "Spatial propagation of excitonic coherence enables ratcheted energy transfer," *Phys. Rev. E*, vol. 86, no. 4, p. 41911, 2012.
[27] A. Ishizaki and G. R. Fleming, "Theoretical examination of quantum coherence in a photosynthetic system at physiological temperature.," *Proc. Natl. Acad. Sci. U. S. A.*, vol. 106, no. 41, pp. 17255–17260, 2009.
[28] J. Wu, F. Liu, J. Ma, R. J. Silbey, and J. Cao, "Efficient energy transfer in light-harvesting systems: Quantum-classical comparison, flux network, and robustness analysis," *J. Chem. Phys.*, vol. 137, no. 17, p. 174111, 2012.
[29] A. W. Chin, A. Datta, F. Caruso, S. F. Huelga, and M. B. Plenio, "Noise-assisted energy transfer in quantum networks and light-harvesting complexes," *New J. Phys.*, vol. 12, no. 6, p. 65002, 2010.
[30] P. Rebentrost, M. Mohseni, I. Kassal, S. Lloyd, and A. Aspuru-Guzik, "Environment-assisted quantum transport," *New J. Phys.*, vol. 11, no. 3, p. 33003, 2009.
[31] M. Mohseni, P. Rebentrost, S. Lloyd, and A. Aspuru-Guzik, "Environment-assisted quantum walks in photosynthetic energy transfer.," *J. Chem. Phys.*, vol. 129, no. 17, p. 174106, 2008.
[32] N. Christensson, H. F. Kauffmann, T. Pullerits, and T. Mančal, "Origin of Long-Lived Coherences in Light-Harvesting Complexes," *J. Phys. Chem. B*, vol. 116, no. 25, pp. 7449–7454, Jun. 2012.
[33] N. Christensson, F. Milota, J. Hauer, J. Sperling, O. Bixner, a. Nemeth, and H. F. Kauffmann, "High frequency vibrational modulations in two-dimensional electronic

spectra and their resemblance to electronic coherence signatures," *J. Phys. Chem. B*, vol. 115, no. 18, pp. 5383–5391, 2011.
[34] V. Tiwari, W. K. Peters, and D. M. Jonas, "Electronic resonance with anticorrelated pigment vibrations drives photosynthetic energy transfer outside the adiabatic framework," *Proc. Natl. Acad. Sci.*, vol. 110, no. 4, pp. 1203–1208, 2013.
[35] A. Chenu, N. Christensson, H. F. Kauffmann, and T. Mančal, "Enhancement of Vibronic and Ground-State Vibrational Coherences in 2D Spectra of Photosynthetic Complexes," *Sci. Rep.*, vol. 3, p. 2029, 2013.
[36] R. Tempelaar, T. L. C. Jansen, and J. Knoester, "Vibrational Beatings Conceal Evidence of Electronic Coherence in the FMO Light-Harvesting Complex.," *J. Phys. Chem. B*, vol. 118, no. 45, pp. 12865–72, 2014.
[37] M. B. Plenio, J. Almeida, and S. F. Huelga, "Origin of long-lived oscillations in 2D-spectra of a quantum vibronic model: electronic versus vibrational coherence.," *J. Chem. Phys.*, vol. 139, no. 23, p. 235102, 2013.
[38] J. M. Womick and A. M. Moran, "Vibronic enhancement of exciton sizes and energy transport in photosynthetic complexes," *J. Phys. Chem. B*, vol. 115, no. 6, pp. 1347–1356, 2011.
[39] E. J. O'Reilly and A. Olaya-Castro, "Non-classicality of the molecular vibrations assisting exciton energy transfer at room temperature.," *Nat. Commun.*, vol. 5, p. 3012, 2014.
[40] A. Kolli, E. J. O'Reilly, G. D. Scholes, A. Olaya-Castro, E. J. O'Reilly, G. D. Scholes, A. Olaya-Castro, E. J. O'Reilly, G. D. Scholes, and A. Olaya-Castro, "The fundamental role of quantized vibrations in coherent light harvesting by cryptophyte algae," *J. Chem. Phys.*, vol. 137, no. 17, p. 174109, 2012.
[41] N. Killoran, S. F. Huelga, and M. B. Plenio, "Enhancing light-harvesting power with coherent vibrational interactions: a quantum heat engine picture," *J. Chem. Phys.*, vol. 143, p. 155102, 2015.
[42] A. W. Chin, J. Prior, R. Rosenbach, F. Caycedo-Soler, S. F. Huelga, and M. B. Plenio, "The role of non-equilibrium vibrational structures in electronic coherence and recoherence in pigment–protein complexes," *Nat. Phys.*, vol. 9, no. 2, pp. 113–118, 2013.
[43] V. Butkus, L. Valkunas, and D. Abramavicius, "Vibronic phenomena and exciton–vibrational interference in two-dimensional spectra of molecular aggregates," *J. Chem. Phys.*, vol. 140, no. 3, p. 34306, 2014.
[44] V. Butkus, D. Zigmantas, L. Valkunas, and D. Abramavicius, "Vibrational vs. electronic coherences in 2D spectrum of molecular systems," *Chem. Phys. Lett.*, vol. 545, pp. 40–43, 2012.
[45] V. Perlík, C. Lincoln, F. Šanda, and J. Hauer, "Distinguishing electronic and vibronic coherence in 2D spectra by their temperature dependence," *J. Phys. Chem. Lett.*, vol. 5, no. 3, pp. 404–407, 2014.
[46] V. Butkus, D. Zigmantas, D. Abramavicius, and L. Valkunas, "Distinctive character of electronic and vibrational coherences in disordered molecular aggregates," *Chem. Phys. Lett.*, vol. 587, pp. 93–98, 2013.
[47] C. Kreisbeck, T. Kramer, and A. Aspuru-Guzik, "Disentangling electronic and vibronic coherences in two-dimensional echo spectra," *J. Phys. Chem. B*, vol. 117, no. 32, pp. 9380–9385, 2013.
[48] J. Seibt and T. Pullerits, "Beating signals in 2D spectroscopy: Electronic or nuclear coherences? application to a quantum dot model system," *J. Phys. Chem. C*, vol. 117, no.

36, pp. 18728–18737, 2013.
[49] J. Yuen-Zhou, J. J. Krich, and A. Aspuru-Guzik, “A witness for coherent electronic vs vibronic-only oscillations in ultrafast spectroscopy,” *J. Chem. Phys.*, vol. 136, no. 23, p. 234501, 2012.
[50] A. S. Johnson, J. Yuen-Zhou, A. Aspuru-Guzik, and J. J. Krich, “Practical witness for electronic coherences.,” *J. Chem. Phys.*, vol. 141, no. 24, p. 244109, 2014.
[51] K. a Fransted, J. R. Caram, D. Hayes, and G. S. Engel, “Two-dimensional electronic spectroscopy of bacteriochlorophyll a in solution: Elucidating the coherence dynamics of the Fenna-Matthews-Olson complex using its chromophore as a control.,” *J. Chem. Phys.*, vol. 137, no. 12, p. 125101, 2012.
[52] D. Hayes, G. B. Griffin, and G. S. Engel, “Engineering coherence among excited states in synthetic heterodimer systems,” *Science*, vol. 1431, no. April, pp. 2014–2016, 2013.
[53] A. Halpin, P. J. M. Johnson, R. Tempelaar, R. S. Murphy, J. Knoester, T. L. C. Jansen, and R. J. D. Miller, “Two-dimensional spectroscopy of a molecular dimer unveils the effects of vibronic coupling on exciton coherences,” *Nat. Chem.*, vol. 6, no. 3, pp. 196–201, 2014.
[54] M. Schröter, T. Pullerits, and O. Kühn, “Unraveling the quantum state mixing of excitonic and vibronic excitations in the dynamics of molecular aggregates,” *Ann. Phys.*, vol. 527, no. 9–10, pp. 536–545, 2015.
[55] E. L. Read, G. S. Schlau-Cohen, G. S. Engel, J. Wen, R. E. Blankenship, and G. R. Fleming, “Visualization of excitonic structure in the Fenna-Matthews-Olson photosynthetic complex by polarization-dependent two-dimensional electronic spectroscopy.,” *Biophys. J.*, vol. 95, no. July, pp. 847–856, 2008.
[56] N. S. Ginsberg, J. A. Davis, M. Ballottari, Y.-C. Cheng, R. Bassi, and G. R. Fleming, “Solving structure in the CP29 light harvesting complex with polarization-phased 2D electronic spectroscopy,” *Proc. Natl. Acad. Sci.*, vol. 108, no. 10, pp. 3848–3853, 2011.
[57] G. D. Scholes and C. Smyth, “Perspective: Detecting and measuring exciton delocalization in photosynthetic light harvesting,” *J. Chem. Phys.*, vol. 140, no. 11, p. 110901, 2014.
[58] R. Tempelaar, F. C. Spano, J. Knoester, and T. L. C. Jansen, “Mapping the evolution of spatial exciton coherence through time-resolved fluorescence,” *J. Phys. Chem. Lett.*, vol. 5, no. 9, pp. 1505–1510, 2014.
[59] M. Rätsep and A. Freiberg, “Electron–phonon and vibronic couplings in the FMO bacteriochlorophyll a antenna complex studied by difference fluorescence line narrowing,” *J. Lumin.*, vol. 127, no. 1, pp. 251–259, 2007.
[60] M. Rätsep, Z. L. Cai, J. R. Reimers, and A. Freiberg, “Demonstration and interpretation of significant asymmetry in the low-resolution and high-resolution Qy fluorescence and absorption spectra of bacteriochlorophyll a,” *J. Chem. Phys.*, vol. 134, no. 2, p. 24506, 2011.
[61] M. Wendling, T. Pullerits, M. a Przyjalgowski, S. I. E. Vulto, T. J. Aartsma, R. van Grondelle, and H. van Amerongen, “Electron Vibrational Coupling in the Fenna Matthews Olson Complex of Prosthecochloris a estuarii Determined by Temperature Dependent Absorption and Fluorescence Line-Narrowing Measurements,” *J. Phys. Chem. B*, vol. 104, no. 24, pp. 5825–5831, 2000.
[62] V. Zazubovich, I. Tibe, and G. J. Small, “Bacteriochlorophyll a Franck−Condon Factors for the S 0 → S 1 (Q y) Transition,” *J. Phys. Chem. B*, vol. 105, no. 49, pp. 12410–12417,

2001.
[63] J. Gillie, G. Small, and J. Golbeck, “Nonphotochemical hole burning of the native antenna complex of photosystem I (PSI-200),” *J. Phys. Chem.*, no. 93, pp. 1620–1627, 1989.
[64] J. Schulze and O. Kühn, “Explicit Correlated Exciton-Vibrational Dynamics of the FMO Complex,” *J. Phys. Chem. B*, vol. 119, no. 20, pp. 6211–6216, 2015.
[65] Y. Fujihashi, G. R. Fleming, and A. Ishizaki, “Impact of environmentally induced fluctuations on quantum mechanically mixed electronic and vibrational pigment states in photosynthetic energy transfer and 2D electronic spectra,” *J. Chem. Phys.*, vol. 142, no. 21, p. 212403, 2015.
[66] T. Brixner, T. Mančal, I. V. Stiopkin, and G. R. Fleming, “Phase-stabilized two-dimensional electronic spectroscopy,” *J. Chem. Phys.*, vol. 121, no. 9, pp. 4221–4236, 2004.
[67] B. Brüggemann, P. Kjellberg, and T. Pullerits, “Non-perturbative calculation of 2D spectra in heterogeneous systems: Exciton relaxation in the FMO complex,” *Chem. Phys. Lett.*, vol. 444, no. 1–3, pp. 192–196, 2007.
[68] M. Toda, R. Kubo, and N. Saito, *Statistical Physics II: Nonequilibrium Statistical Mechanics*. Springer, 1992.
[69] A. Nitzan and J. Jortner, “Vibrational relaxation of a molecule in a dense medium,” *Mol. Phys.*, vol. 25, no. 3, pp. 713–734, 1973.
[70] S. Mukamel, *Principles of Nonlinear Spectroscopy*. Oxford University Press, 1995.
[71] A. Ishizaki and Y. Tanimura, “Dynamics of a multimode system coupled to multiple heat baths probed by two-dimensional infrared spectroscopy,” *J. Phys. Chem. A*, vol. 111, no. 38, pp. 9269–9276, 2007.
[72] L. E. Fried and S. Mukamel, “A classical theory of pump–probe photodissociation for arbitrary pulse durations,” *J. Chem. Phys.*, vol. 93, no. 5, p. 3063, 1990.
[73] J. Schulze, M. Torbjörnsson, O. Kühn, and T. Pullerits, “Exciton coupling induces vibronic hyperchromism in light-harvesting complexes,” *New J. Phys.*, vol. 16, no. 4, p. 45010, 2014.
[74] W. Mendenhall, R. Beaver, and B. Beaver, *Introduction to Probability and Statistics*. Boston: Brooks/Cole, 2013.
[75] S. Hill and W. K. Wootters, “Entanglement of a Pair of Quantum Bits,” *Phys. Rev. Lett.*, vol. 78, no. 26, pp. 5022–5025, 1997.
[76] W. K. Wootters, “Entanglement of Formation of an Arbitrary State of Two Qubits,” vol. 80, no. 10, pp. 2245–2248, 1998.
[77] T. Yu and J. H. Eberly, “Evolution from Entanglement to Decoherence of Bipartite Mixed ‘X’ States,” *Quantum Inf. Comput.*, vol. 7, no. 5, pp. 459–468, 2007.
[78] A. Ishizaki and G. R. Fleming, “Quantum superpositions in photosynthetic light harvesting: delocalization and entanglement,” *New J. Phys.*, vol. 12, no. 5, p. 55004, 2010.
[79] T. Yu and J. Eberly, “Sudden Death of Entanglement,” *Science*, vol. 323, no. 5914, pp. 598–601, 2009.
[80] Z. Ficek and R. Tanaś, “Dark periods and revivals of entanglement in a two-qubit system,” *Phys. Rev. A - At. Mol. Opt. Phys.*, vol. 74, no. 2, pp. 8–11, 2006.
[81] Z. Y. Xu and M. Feng, “Sudden death and birth of entanglement beyond the Markovian approximation,” *Phys. Lett. Sect. A Gen. At. Solid State Phys.*, vol. 373, no. 22, pp. 1906–1910, 2009.
[82] S. F. Huelga, Á. Rivas, and M. B. Plenio, “Non-Markovianity-assisted steady state

entanglement," *Phys. Rev. Lett.*, vol. 108, no. 16, p. 160402, 2012.
[83] L. Duan, H. Wang, Q. H. Chen, and Y. Zhao, "Entanglement dynamics of two qubits coupled individually to Ohmic baths," *J. Chem. Phys.*, vol. 139, no. 4, p. 44115, 2013.
[84] T. A. A. Oliver, N. H. C. Lewis, and G. R. Fleming, "Correlating the motion of electrons and nuclei with two-dimensional electronic-vibrational spectroscopy," *Proc. Natl. Acad. Sci.*, vol. 111, no. 28, pp. 10061–10066, Jul. 2014.
[85] N. H. C. Lewis, H. Dong, T. A. A. Oliver, and G. R. Fleming, "Measuring correlated electronic and vibrational spectral dynamics using line shapes in two-dimensional electronic-vibrational spectroscopy," *J. Chem. Phys.*, vol. 142, no. 17, 2015.
[86] H. Dong, N. H. C. Lewis, T. A. A. Oliver, and G. R. Fleming, "Determining the static electronic and vibrational energy correlations via two-dimensional electronic-vibrational spectroscopy," *J. Chem. Phys.*, vol. 142, no. 17, 2015.
[87] E. Rivera, D. Montemayor, M. Masia, and D. F. Coker, "Influence of site-dependent pigment-protein interactions on excitation energy transfer in photosynthetic light harvesting," *J. Phys. Chem. B*, vol. 117, no. 18, pp. 5510–5521, 2013.
[88] L. Guo, D. M. Monahan, and G. Fleming, "Rapid and economical data acquisition in ultrafast frequency-resolved spectroscopy using choppers and a microcontroller," *Opt. Epxress*, vol. 106, no. 23, pp. 18126–18132, 2016.
[89] R. J. Stevens, A. N. Smith, and P. M. Norris, "Signal analysis and characterization of experimental setup for the transient thermoreflectance technique," *Rev. Sci. Instrum.*, vol. 77, no. 8, p. 84901, Aug. 2006.
[90] J. Zhu, D. Tang, W. Wang, J. Liu, K. W. Holub, and R. Yang, "Ultrafast thermoreflectance techniques for measuring thermal conductivity and interface thermal conductance of thin films," *J. Appl. Phys.*, vol. 108, no. 9, p. 94315, Nov. 2010.
[91] L. Guo, S. L. Hodson, T. S. Fisher, and X. Xu, "Heat Transfer Across Metal-Dielectric Interfaces During Ultrafast-Laser Heating," *J. Heat Transfer*, vol. 134, no. 4, p. 42402, Apr. 2012.
[92] H. Wang, L. Whittaker-Brooks, and G. R. Fleming, "Exciton and Free Charge Dynamics of Methylammonium Lead Iodide Perovskites Are Different in the Tetragonal and Orthorhombic Phases," *J. Phys. Chem. C*, vol. 119, no. 34, pp. 19590–19595, 2015.
[93] Wei Wang, Xiong Ye, Andrey A. Demidov, Florin Rosca, Theodore Sjodin, WenXiang Cao, A. Mariel Sheeran, and P. M. Champion, "Femtosecond Multicolor Pump−Probe Spectroscopy of Ferrous Cytochrome c," vol. 104, pp. 10789–10801, 2000.
[94] R. R. Augulis and D. Zigmantas, "Two-dimensional electronic spectroscopy with double modulation lock-in detection: enhancement of sensitivity and noise resistance.," *Opt. Express*, vol. 19, no. 14, pp. 13126–13133, Jul. 2011.
[95] I. A. Heisler, R. Moca, F. V. A. Camargo, and S. R. Meech, "Two-dimensional electronic spectroscopy based on conventional optics and fast dual chopper data acquisition," *Rev. Sci. Instrum.*, vol. 85, no. 6, p. 63103, Jun. 2014.
[96] H. L. Fragnito, J. Y. Bigot, P. C. Becker, and C. V. Shank, "Evolution of the vibronic absorption spectrum in a molecule following impulsive excitation with a 6 fs optical pulse," *Chem. Phys. Lett.*, vol. 160, no. 2, pp. 101–104, Aug. 1989.
[97] A. K. De, D. Monahan, J. M. Dawlaty, and G. R. Fleming, "Two-dimensional fluorescence-detected coherent spectroscopy with absolute phasing by confocal imaging of a dynamic grating and 27-step phase-cycling," *J. Chem. Phys.*, vol. 140, no. 19, 2014.
[98] D. M. Jonas, "Two-Dimensional Femtosecond Spectroscopy," *Annu. Rev. Phys. Chem.*,

vol. 54, no. 1, pp. 425–463, 2003.
[99] T. Brixner, I. V Stiopkin, and G. R. Fleming, “Tunable two-dimensional femtosecond spectroscopy,” *Opt. Lett.*, vol. 29, no. 8, pp. 884–886, 2004.
[100] T. Zhang, C. N. Borca, X. Li, and S. T. Cundiff, “Optical two-dimensional Fourier transform spectroscopy with active interferometric stabilization,” *Opt. Express*, vol. 13, no. 19, p. 7432, Sep. 2005.
[101] U. Selig, F. Langhojer, F. Dimler, T. Löhrig, C. Schwarz, B. Gieseking, and T. Brixner, “Inherently phase-stable coherent two-dimensional spectroscopy using only conventional optics,” *Opt. Lett.*, vol. 33, no. 23, p. 2851, Dec. 2008.
[102] K. Gundogdu, K. W. Stone, D. B. Turner, and K. a. Nelson, “Multidimensional coherent spectroscopy made easy,” *Chem. Phys.*, vol. 341, pp. 89–94, Nov. 2007.
[103] A. Ishizaki and G. R. Fleming, “On the interpretation of quantum coherent beats observed in two-dimensional electronic spectra of photosynthetic light harvesting complexes,” *J. Phys. Chem. B*, vol. 115, pp. 6227–6233, 2011.
[104] H. Dong and G. R. Fleming, “Three-pulse photon echo of finite numbers of molecules: single-molecule traces.,” *J. Phys. Chem. B*, vol. 117, no. 38, pp. 11318–11325, 2013.
[105] J. M. Dawlaty, A. Ishizaki, A. K. De, and G. R. Fleming, “Microscopic quantum coherence in a photosynthetic-light-harvesting antenna.,” *Philos. Trans. A. Math. Phys. Eng. Sci.*, vol. 370, no. 1972, pp. 3672–91, Aug. 2012.
[106] D. Brinks, F. D. Stefani, F. Kulzer, R. Hildner, T. H. Taminiau, Y. Avlasevich, K. Müllen, and N. F. van Hulst, “Visualizing and controlling vibrational wave packets of single molecules.,” *Nature*, vol. 465, no. 7300, pp. 905–8, Jun. 2010.
[107] R. Hildner, D. Brinks, and N. F. van Hulst, “Femtosecond coherence and quantum control of single molecules at room temperature,” *Nat. Phys.*, vol. 7, no. 2, pp. 172–177, 2011.
[108] R. Hildner, D. Brinks, J. B. Nieder, R. J. Cogdell, and N. F. van Hulst, “Quantum Coherent Energy Transfer over Varying Pathways in Single Light-Harvesting Complexes,” *Science*, vol. 340, no. 6139, pp. 1448–1451, 2013.
[109] W. E. Moerner and L. Kador, “Optical detection and spectroscopy of single molecules in a solid,” *Phys. Rev. Lett.*, vol. 62, no. 21, pp. 2535–2538, May 1989.
[110] A. Gaiduk, M. Yorulmaz, P. V Ruijgrok, and M. Orrit, “Room-temperature detection of a single molecule’s absorption by photothermal contrast.,” *Science*, vol. 330, no. 6002, pp. 353–6, Oct. 2010.
[111] P. Kukura, M. Celebrano, A. Renn, and V. Sandoghdar, “Single-Molecule Sensitivity in Optical Absorption at Room Temperature,” *J. Phys. Chem. Lett.*, vol. 1, no. 23, pp. 3323–3327, Dec. 2010.
[112] S. Chong, W. Min, and X. S. Xie, “Ground-State Depletion Microscopy: Detection Sensitivity of Single-Molecule Optical Absorption at Room Temperature,” *J. Phys. Chem. Lett.*, vol. 1, no. 23, pp. 3316–3322, Dec. 2010.
[113] M. Orrit and J. Bernard, “Single pentacene molecules detected by fluorescence excitation in a *p* -terphenyl crystal,” *Phys. Rev. Lett.*, vol. 65, no. 21, pp. 2716–2719, Nov. 1990.
[114] C. Gell, D. Brockwell, and A. Smith, *Handbook of Single Molecule Fluorescence Spectroscopy*. Oxford: Oxford University Press, 2013.
[115] P. Tian, D. Keusters, Y. Suzaki, and W. S. Warren, “Femtosecond Phase-Coherent Two-Dimensional Spectroscopy,” *Science*, vol. 300, no. 5625, pp. 1553–1555, Jun. 2003.
[116] W. Wagner, C. Li, J. Semmlow, and W. S. Warren, “Rapid phase-cycled two-dimensional optical spectroscopy in fluorescence and transmission mode,” *Opt. Express*, vol. 13, no.

10, p. 3697, May 2005.
[117] C. Li, W. Wagner, M. Ciocca, and W. S. Warren, “Multiphoton femtosecond phase-coherent two-dimensional electronic spectroscopy,” *J. Chem. Phys.*, vol. 126, no. 16, p. 164307, Apr. 2007.
[118] P. F. Tekavec, G. A. Lott, and A. H. Marcus, “Fluorescence-detected two-dimensional electronic coherence spectroscopy by acousto-optic phase modulation,” *J. Chem. Phys.*, vol. 127, no. 21, p. 214307, Dec. 2007.
[119] G. A. Lott, A. Perdomo-Ortiz, J. K. Utterback, J. R. Widom, A. Aspuru-Guzik, and A. H. Marcus, “Conformation of self-assembled porphyrin dimers in liposome vesicles by phase-modulation 2D fluorescence spectroscopy.,” *Proc. Natl. Acad. Sci. U. S. A.*, vol. 108, no. 40, pp. 16521–6, Oct. 2011.
[120] J. R. Widom, N. P. Johnson, P. H. von Hippel, and A. H. Marcus, “Solution conformation of 2-aminopurine dinucleotide determined by ultraviolet two-dimensional fluorescence spectroscopy,” *New J. Phys.*, vol. 15, no. 2, p. 25028, Feb. 2013.
[121] M. Aeschlimann, T. Brixner, A. Fischer, C. Kramer, P. Mechior, W. Pfeiffer, C. Schneider, C. Struber, P. Tuchscherer, and D. V. Voronine, “Coherent Two-Dimensional Nanoscopy,” *Science*, vol. 333, no. 6050, pp. 1723–1726, 2011.
[122] J. C. Vaughan, T. Hornung, T. Feurer, and K. A. Nelson, “Diffraction-based femtosecond pulse shaping with a two-dimensional spatial light modulator,” *Opt. Lett.*, vol. 30, no. 3, p. 323, Feb. 2005.
[123] J. M. Dawlaty, D. I. G. Bennett, V. M. Huxter, and G. R. Fleming, “Mapping the spatial overlap of excitons in a photosynthetic complex via coherent nonlinear frequency generation,” *J. Chem. Phys.*, vol. 135, no. 4, Jul. 2011.
[124] G. Donnert, C. Eggeling, and S. W. Hell, “Major signal increase in fluorescence microscopy through dark-state relaxation,” *Nat. Methods*, vol. 4, no. 1, pp. 81–86, Jan. 2007.
[125] A. K. De and D. Goswami, “Exploring the Nature of Photo-Damage in Two-photon Excitation by Fluorescence Intensity Modulation,” *J. Fluoresc.*, vol. 19, no. 2, pp. 381–386, Mar. 2009.
[126] R. Bloem, S. Garrett-Roe, H. Strzalka, P. Hamm, and P. Donaldson, “Enhancing signal detection and completely eliminating scattering using quasi-phase-cycling in 2D IR experiments.,” *Opt. Express*, vol. 18, no. 26, pp. 27067–27078, Dec. 2010.
[127] N. F. Scherer, A. J. Ruggiero, M. Du, and G. R. Fleming, “Time resolved dynamics of isolated molecular systems studied with phase- locked femtosecond pulse pairs,” *J. Chem. Phys.*, vol. 93, no. 1, pp. 856–857, Jul. 1990.
[128] N. F. Scherer, R. J. Carlson, A. Matro, M. Du, A. J. Ruggiero, V. Romero- Rochin, J. A. Cina, G. R. Fleming, and S. A. Rice, “Fluorescence- detected wave packet interferometry: Time resolved molecular spectroscopy with sequences of femtosecond phase- locked pulses,” *J. Chem. Phys.*, vol. 95, no. 3, pp. 1487–1511, Aug. 1991.
[129] N. F. Scherer, A. Matro, L. D. Ziegler, M. Du, R. J. Carlson, J. A. Cina, and G. R. Fleming, “Fluorescence- detected wave packet interferometry. II. Role of rotations and determination of the susceptibility,” *J. Chem. Phys.*, vol. 96, no. 6, pp. 4180–4194, Mar. 1992.
[130] J. T. Fourkas, R. Trebino, and M. D. Fayer, “The grating decomposition method: A new approach for understanding polarization-selective transient grating experiments. I. Applications,” *J. Chem. Phys.*, vol. 97, no. 1, p. 69, 1992.

[131] N. Belabas and D. M. Jonas, “Three-dimensional view of signal propagation in femtosecond four-wave mixing with application to the boxcars geometry,” *J. Opt. Soc. Am. B*, vol. 22, no. 3, p. 655, Mar. 2005.
[132] M. K. Yetzbacher, N. Belabas, K. A. Kitney, and D. M. Jonas, “Propagation, beam geometry, and detection distortions of peak shapes in two-dimensional Fourier transform spectra,” *J. Chem. Phys.*, vol. 126, no. 4, p. 44511, Jan. 2007.
[133] S. M. Gallagher Faeder and D. M. Jonas, “Two-Dimensional Electronic Correlation and Relaxation Spectra: Theory and Model Calculations,” *J. Phys. Chem. A*, vol. 103, no. 49, pp. 10489–10505, 1999.
[134] E. H. G. Backus, S. Garrett-Roe, and P. Hamm, “Phasing problem of heterodyne-detected two-dimensional infrared spectroscopy.,” *Opt. Lett.*, vol. 33, no. 22, pp. 2665–2667, Nov. 2008.
[135] A. D. Bristow, D. Karaiskaj, X. Dai, and S. T. Cundiff, “All-optical retrieval of the global phase for two-dimensional Fourier-transform spectroscopy.,” *Opt. Express*, vol. 16, no. 22, pp. 18017–18027, Oct. 2008.
[136] D. M. Monahan, L. Guo, J. Lin, L. Dou, P. Yang, and G. R. Fleming, “Room-Temperature Coherent Optical Phonon in 2D Electronic Spectra of CH3NH3PbI3 Perovskite as a Possible Cooling Bottleneck,” *J. Phys. Chem. Lett.*, vol. 8, no. 14, pp. 3211–3215, 2017.
[137] L. M. Herz, “Charge Carrier Dynamics in Organic-Inorganic Metal Halide Perovskites,” *Annu. Rev. Condens. Matter Phys.*, vol. 67, pp. 65–89, 2015.
[138] Y. Bi, E. M. Hutter, Y. Fang, Q. Dong, J. Huang, and T. J. Savenije, “Charge Carrier Lifetimes Exceeding 15 μs in Methylammonium Lead Iodide Single Crystals,” *J. Phys. Chem. Lett.*, vol. 7, no. 5, pp. 923–928, 2016.
[139] C. S. Ponseca, T. J. Savenije, M. Abdellah, K. Zheng, A. Yartsev, T. Pascher, T. Harlang, P. Chabera, T. Pullerits, A. Stepanov, J. P. Wolf, and V. Sundstrom, “Organometal halide perovskite solar cell materials rationalized: Ultrafast charge generation, high and microsecond-long balanced mobilities, and slow recombination,” *J. Am. Chem. Soc.*, vol. 136, no. 14, pp. 5189–5192, 2014.
[140] Y. Chen, H. T. Yi, X. Wu, R. Haroldson, Y. Gartstein, A. Zakhidov, Z.-Y. Zhu, and V. Podzorov, “Ultra-long carrier lifetimes and diffusion lengths in hybrid perovskites revealed by steady-state Hall effect and photoconductivity measurements,” *Nat. Commun.*, vol. 7, p. 12253, 2016.
[141] S. D. Stranks, S. D. Stranks, G. E. Eperon, G. Grancini, C. Menelaou, M. J. P. Alcocer, T. Leijtens, L. M. Herz, A. Petrozza, and H. J. Snaith, “Electron-Hole Diffusion Lengths Exceeding 1 Micrometer in an Organometal Trihalide Perovskite Absorber,” *Science*, vol. 342, pp. 341–344, 2014.
[142] G. Xing, N. Mathews, S. S. Lim, Y. M. Lam, S. Mhaisalkar, and T. C. Sum, “Long-Range Balanced Electron- and Hole-Transport Lengths in Organic-Inorganic CH3NH3PbI3,” *Science*, vol. 342, pp. 344–347, 2013.
[143] F. Deschler, M. Price, S. Pathak, L. E. Klintberg, D. Jarausch, R. Higler, T. Leijtens, S. D. Stranks, H. J. Snaith, R. T. Phillips, and R. H. Friend, “High Photoluminescence Efficiency and Optically Pumped Lasing in Solution-Processed Mixed Halide Perovskite Semiconductors,” *J. Phys. Chem. Lett.*, vol. 5, pp. 1421–1426, 2014.
[144] H. Zhu, Y. Fu, F. Meng, X. Wu, Z. Gong, Q. Ding, M. V Gustafsson, M. T. Trinh, S. Jin, and X.-Y. Zhu, “Lead halide perovskite nanowire lasers with low lasing thresholds and high quality factors.,” *Nat. Mater.*, vol. 14, pp. 636–642, 2015.

[145] A. Filippetti, C. Caddeo, P. D. Delugas, and A. Mattoni, “On the Appealing Perspectives of Hybrid Lead-Iodide Perovskites as Thermoelectric Materials,” *J. Phys. Chem. C*, vol. 120, pp. 28472–28479, 2016.
[146] G. P. Nagabhushana, R. Shivaramaiah, and A. Navrotsky, “Direct Thermochemical Verification of Thermodynamic Instability of Lead Halide Perovskites,” *PNAS*, vol. 113, no. 28, pp. 7717–7721, 2016.
[147] P. P. Boix, S. Agarwala, T. M. Koh, N. Mathews, and S. G. Mhaisalkar, “Perovskite solar cells: Beyond methylammonium lead iodide,” *J. Phys. Chem. Lett.*, vol. 6, no. 5, pp. 898–907, 2015.
[148] A. Miyata, A. Mitioglu, P. Plochocka, O. Portugall, J. T. Wang, S. D. Stranks, H. J. Snaith, and R. J. Nicholas, “Direct measurement of the exciton binding energy and effective masses for charge carriers in organic-inorganic tri-halide perovskites,” *Nat. Phys.*, vol. 11, no. 7, pp. 582–587, 2015.
[149] V. D’Innocenzo, G. Grancini, M. J. P. Alcocer, A. R. S. Kandada, S. D. Stranks, M. M. Lee, G. Lanzani, H. J. Snaith, and A. Petrozza, “Excitons versus free charges in organo-lead tri-halide perovskites.,” *Nat. Commun.*, vol. 5, p. 3586, 2014.
[150] X. Y. Zhu and V. Podzorov, “Charge Carriers in Hybrid Organic-Inorganic Lead Halide Perovskites Might Be Protected as Large Polarons,” *J. Phys. Chem. Lett.*, vol. 6, no. 23, pp. 4758–4761, 2015.
[151] H. Zhu, K. Miyata, Y. Fu, J. Wang, P. P. Joshi, D. Niesner, K. W. Williams, S. Jin, and X.-Y. Y. Zhu, “Screening in Crystalline Liquids Protects Energetic Carriers in Hybrid Perovskites,” *Science*, vol. 353, no. 6306, pp. 1409–1413, 2016.
[152] A. A. Bakulin, O. Selig, H. J. Bakker, Y. L. A. Rezus, C. Müller, T. Glaser, R. Lovrincic, Z. Sun, Z. Chen, A. Walsh, J. M. Frost, and T. L. C. Jansen, “Real-time observation of organic cation reorientation in methylammonium lead-iodide perovskites,” *J. Phys. Chem. Lett.*, vol. 6, pp. 3663–3669, 2015.
[153] M. B. Price, J. Butkus, T. C. Jellicoe, A. Sadhanala, A. Briane, J. E. Halpert, K. Broch, J. M. Hodgkiss, R. H. Friend, and F. Deschler, “Hot-carrier cooling and photoinduced refractive index changes in organic–inorganic lead halide perovskites,” *Nat. Commun.*, vol. 6, p. 8420, 2015.
[154] Y. Yang, D. P. Ostrowski, R. M. France, K. Zhu, J. van de Lagemaat, J. M. Luther, and M. C. Beard, “Observation of a hot-phonon bottleneck in lead-iodide perovskites,” *Nat. Photonics*, vol. 10, pp. 53–59, 2015.
[155] D. Niesner, H. Zhu, K. Miyata, P. P. Joshi, T. J. S. Evans, B. J. Kudisch, M. T. Trinh, M. Marks, and X. Zhu, “Persistent Energetic Electrons in Methylammonium Lead Iodide Perovskite Thin Films,” *J. Am. Chem. Soc.*, vol. 138, no. 48, pp. 15717–15726, 2016.
[156] J. Yang, X. Wen, H. Xia, R. Sheng, Q. Ma, J. Kim, P. Tapping, T. Harada, T. W. Kee, F. Huang, Y.-B. Cheng, M. Green, A. Ho-Baillie, S. Huang, S. Shrestha, R. Patterson, and G. Conibeer, “Acoustic-optical phonon up-conversion and hot-phonon bottleneck in lead-halide perovskites,” *Nat. Commun.*, vol. 8, p. 14120, 2017.
[157] J. M. Richter, F. Branchi, F. V. de A. Camargo, B. Zhao, R. H. Friend, G. Cerullo, and F. Deschler, “Ultrafast carrier thermalization in lead iodide perovskite probed with two-dimensional electronic spectroscopy,” 2017.
[158] H. Wang, L. Valkunas, T. Cao, L. Whittaker-Brooks, and G. R. Fleming, “Coulomb Screening and Coherent Phonon in Methylammonium Lead Iodide Perovskites,” *J. Phys. Chem. Lett.*, vol. 7, pp. 3284–3289, 2016.

[159] A. M. A. Leguy, A. R. Goñi, J. M. Frost, J. Skelton, F. Brivio, X. Rodríguez-Martínez, O. J. Weber, A. Pallipurath, M. I. Alonso, M. Campoy-Quiles, M. T. Weller, J. Nelson, A. Walsh, and P. R. F. Barnes, "Dynamic disorder, phonon lifetimes, and the assignment of modes to the vibrational spectra of methylammonium lead halide perovskites," *Phys. Chem. Chem. Phys.*, vol. 18, no. 39, pp. 27051–27066, 2016.
[160] F. Brivio, J. M. Frost, J. M. Skelton, J. Adam, O. J. Weber, M. T. Weller, A. R. Go, A. J. Jackson, O. J. Weber, M. T. Weller, A. R. Goni, A. M. A. Leguy, P. R. F. Barnes, A. Walsh, J. Adam, O. J. Weber, M. T. Weller, and A. R. Go, "Lattice dynamics and vibrational spectra of the orthorhombic, tetragonal, and cubic phases of methylammonium lead iodide," *Phys Rev B*, vol. 92, p. 144308, 2015.
[161] C. La-O-Vorakiat, H. Xia, J. Kadro, T. Salim, D. Zhao, T. Ahmed, Y. M. Lam, J. X. Zhu, R. A. Marcus, M. E. Michel-Beyerle, and E. E. M. Chia, "Phonon Mode Transformation Across the Orthohombic-Tetragonal Phase Transition in a Lead Iodide Perovskite CH3NH3PbI3: A Terahertz Time-Domain Spectroscopy Approach," *J. Phys. Chem. Lett.*, vol. 7, no. 1, pp. 1–6, 2016.
[162] M. A. Pérez-Osorio, R. L. Milot, M. R. Filip, J. B. Patel, L. M. Herz, M. B. Johnston, and F. Giustino, "Vibrational Properties of the Organic-Inorganic Halide Perovskite CH3NH3PbI3 from Theory and Experiment: Factor Group Analysis, First-Principles Calculations, and Low-Temperature Infrared Spectra," *J. Phys. Chem. C*, vol. 119, no. 46, pp. 25703–25718, 2015.
[163] N. Onoda-Yamamuro, T. Matsuo, and H. Suga, "Dielectric study of CH3NH3PbX3 (X = Cl, Br, I)," *J. Phys. Chem. Solids*, vol. 53, no. 7, pp. 935–939, 1992.
[164] Y. Yan, W.-J. Yin, T. Shi, W. Meng, and C. Feng, "Defect Physics of CH3NH3PbX3 (X = I, Br, Cl) Perovskites," in *Organic-Inorganic Halide Perovskite Photovoltaics: From Fundamentals to Device Architectures*, N.-G. Park, M. Gratzel, and T. Miyasaka, Eds. Springer International Publishing Switzerland, 2016, pp. 79–105.
[165] H. Kawai, G. Giorgi, A. Marini, and K. Yamashita, "The mechanism of slow hot-hole cooling in lead-iodide perovskite: First-principles calculation on carrier lifetime from electron-phonon interaction," *Nano Lett.*, vol. 15, no. 5, pp. 3103–3108, 2015.
[166] J. Gong, M. Yang, X. Ma, R. D. Schaller, G. Liu, L. Kong, Y. Yang, M. C. Beard, M. Lesslie, Y. Dai, B. Huang, K. Zhu, and T. Xu, "Electron-Rotor Interaction in Organic-Inorganic Lead Iodide Perovskites Discovered by Isotope Effects," *J. Phys. Chem. Lett.*, vol. 7, no. 15, pp. 2879–2887, 2016.
[167] D. Lembke, S. Bertolazzi, and A. Kis, "Single-Layer MoS_2 Electronics," *Acc. Chem. Res.*, vol. 48, no. 1, pp. 100–110, 2015.
[168] S. B. Desai, S. R. Madhvapathy, A. B. Sachid, J. P. Llinas, Q. Wang, G. H. Ahn, G. Pitner, M. J. Kim, J. Bokor, C. Hu, H.-S. P. Wong, and A. Javey, "MoS2 transistors with 1-nanometer gate lengths.," *Science*, vol. 354, no. 6308, pp. 99–102, Oct. 2016.
[169] Y. Lin, X. Ling, L. Yu, S. Huang, A. L. Hsu, Y.-H. Lee, J. Kong, M. S. Dresselhaus, and T. Palacios, "Dielectric Screening of Excitons and Trions in Single-Layer MoS2," *Nano Lett.*, vol. 14, no. 10, pp. 5569–5576, Oct. 2014.
[170] M. M. Ugeda, A. J. Bradley, S.-F. Shi, F. H. da Jornada, Y. Zhang, D. Y. Qiu, W. Ruan, S.-K. Mo, Z. Hussain, Z.-X. Shen, F. Wang, S. G. Louie, and M. F. Crommie, "Giant bandgap renormalization and excitonic effects in a monolayer transition metal dichalcogenide semiconductor," *Nat. Mater.*, vol. 13, no. 12, pp. 1091–1095, Aug. 2014.
[171] S. Sim, J. Park, J.-G. G. Song, C. In, Y.-S. S. Lee, H. Kim, and H. Choi, "Exciton

dynamics in atomically thin MoS2: Interexcitonic interaction and broadening kinetics," *Phys. Rev. B - Condens. Matter Mater. Phys.*, vol. 88, p. 75434, Aug. 2013.
[172] C. Mai, A. Barrette, Y. Yu, Y. G. Semenov, K. W. Kim, L. Cao, and K. Gundogdu, "Many-Body Effects in Valleytronics: Direct Measurement of Valley Lifetimes in Single-Layer MoS2," *Nano Lett.*, vol. 14, no. 1, pp. 202–206, Jan. 2014.
[173] K. F. Mak, C. Lee, J. Hone, J. Shan, and T. F. Heinz, "Atomically Thin MoS 2 : A New Direct-Gap Semiconductor," *Phys. Rev. Let*, vol. 105, 2010.
[174] A. Splendiani, L. Sun, Y. Zhang, T. Li, J. Kim, C. Y. Chim, G. Galli, and F. Wang, "Emerging photoluminescence in monolayer MoS2," *Nano Lett.*, vol. 10, no. 4, pp. 1271–1275, 2010.
[175] K. F. Mak, K. He, J. Shan, and T. F. Heinz, "Control of valley polarization in monolayer MoS2 by optical helicity," *Nat. Nanotechnol.*, vol. 7, no. 8, pp. 494–498, 2012.
[176] K. F. Mak, K. He, C. Lee, G. H. Lee, J. Hone, T. F. Heinz, and J. Shan, "Tightly bound trions in monolayer MoS2," *Nat. Mater.*, vol. 12, no. 3, pp. 207–211, Dec. 2012.
[177] C. H. Lui, A. J. Frenzel, D. V. Pilon, Y.-H. Lee, X. Ling, G. M. Akselrod, J. Kong, and N. Gedik, "Trion-Induced Negative Photoconductivity in Monolayer MoS2," *Phys. Rev. Lett.*, vol. 113, no. 16, p. 166801, Oct. 2014.
[178] M. Amani, R. A. Burke, X. Ji, P. Zhao, D.-H. Lien, P. Taheri, G. H. Ahn, D. Kirya, J. W. Ager, E. Yablonovitch, J. Kong, M. Dubey, and A. Javey, "High Luminescence Efficiency in MoS2 Grown by Chemical Vapor Deposition," *ACS Nano*, vol. 10, no. 7, pp. 6535–6541, Jul. 2016.
[179] R. S. Sundaram, M. Engel, A. Lombardo, R. Krupke, A. C. Ferrari, P. Avouris, and M. Steiner, "Electroluminescence in Single Layer MoS2," *Nano Lett.*, vol. 13, no. 4, pp. 1416–1421, Apr. 2013.
[180] Y. Ye, Z. Ye, M. Gharghi, H. Zhu, M. Zhao, Y. Wang, X. Yin, and X. Zhang, "Exciton-dominant electroluminescence from a diode of monolayer MoS2," *Appl. Phys. Lett.*, vol. 104, no. 19, p. 193508, May 2014.
[181] W. E. Moerner, Ed., *Persistent Spectral Hole Burning*. Springer-Verlag, 1988.
[182] M. E. Siemens, G. Moody, H. Li, A. D. Bristow, and S. T. Cundiff, "Resonance lineshapes in two-dimensional Fourier transform spectroscopy.," *Opt. Express*, vol. 18, no. 17, pp. 17699–17708, 2010.
[183] Y. Cai, J. Lan, G. Zhang, and Y. W. Zhang, "Lattice vibrational modes and phonon thermal conductivity of monolayer MoS 2," *Phys. Rev. B - Condens. Matter Mater. Phys.*, vol. 89, no. 3, p. 35438, 2014.
[184] K. Hao, L. Xu, P. Nagler, A. Singh, K. Tran, C. K. Dass, C. Schüller, T. Korn, X. Li, and G. Moody, "Coherent and Incoherent Coupling Dynamics between Neutral and Charged Excitons in Monolayer MoSe2," *Nano Lett.*, vol. 16, no. 8, pp. 5109–5113, Aug. 2016.
[185] A. Singh, G. Moody, S. Wu, Y. Wu, N. J. Ghimire, J. Yan, D. G. Mandrus, X. Xu, and X. Li, "Coherent Electronic Coupling in Atomically Thin MoSe2," *Phys. Rev. Lett.*, vol. 112, no. 21, p. 216804, May 2014.
[186] D. Lagarde, L. Bouet, X. Marie, C. R. Zhu, B. L. Liu, T. Amand, P. H. Tan, and B. Urbaszek, "Carrier and Polarization Dynamics in Monolayer MoS 2," *Phys. Rev. Lett.*, vol. 112, no. 4, p. 47401, Jan. 2014.
[187] Q. Wang, S. Ge, X. Li, J. Qiu, Y. Ji, J. Feng, and D. Sun, "Valley carrier dynamics in monolayer molybdenum disulfide from helicity-resolved ultrafast pump-probe spectroscopy," *ACS Nano*, vol. 7, no. 12, pp. 11087–11093, Dec. 2013.

[188] C. Mai, Y. G. Semenov, A. Barrette, Y. Yu, Z. Jin, L. Cao, K. W. Kim, and K. Gundogdu, "Exciton valley relaxation in a single layer of WS2 measured by ultrafast spectroscopy," *Phys. Rev. B - Condens. Matter Mater. Phys.*, vol. 90, Jul. 2014.
[189] X. Li, T. Zhang, C. N. Borca, and S. T. Cundiff, "Many-Body Interactions in Semiconductors Probed by Optical Two-Dimensional Fourier Transform Spectroscopy," *Phys. Rev. Lett.*, vol. 96, no. 5, p. 57406, Feb. 2006.
[190] A. M. Jones, H. Yu, J. R. Schaibley, J. Yan, D. G. Mandrus, T. Taniguchi, K. Watanabe, H. Dery, W. Yao, and X. Xu, "Excitonic luminescence upconversion in a two-dimensional semiconductor," *Nat. Phys.*, vol. 12, no. 4, pp. 323–327, Dec. 2015.
[191] E. M. Mannebach, K.-A. N. Duerloo, L. A. Pellouchoud, M.-J. Sher, S. Nah, Y.-H. Kuo, Y. Yu, A. F. Marshall, L. Cao, E. J. Reed, and A. M. Lindenberg, "Ultrafast Electronic and Structural Response of Monolayer MoS2 under Intense Photoexcitation Conditions," *ACS Nano*, vol. 8, no. 10, pp. 10734–10742, Oct. 2014.
[192] K. Miyata, T. L. Atallah, and X.-Y. Zhu, "Lead halide perovskites: Crystal-liquid duality, phonon glass electron crystals, and large polaron formation," *Sci. Adv.*, vol. 3, p. e1701469, Oct. 2017.
[193] J. M. Frost, L. D. Whalley, and A. Walsh, "Slow cooling of hot polarons in halide perovskite solar cells," *ACS Energy Lett.*, vol. 2, pp. 2647–2652, 2017.
[194] H. Kim, J. Hunger, E. Cánovas, M. Karakus, Z. Mics, M. Grechko, D. Turchinovich, S. H. Parekh, and M. Bonn, "Direct observation of mode-specific phonon-band gap coupling in methylammonium lead halide perovskites.," *Nat. Commun.*, vol. 8, no. 1, p. 687, Sep. 2017.
[195] X. Yang, Y. Wang, H. Li, and C. Sheng, "Optical Properties of Heterojunction between Hybrid Halide Perovskite and Charge Transport Materials: Exciplex Emission and Large Polaron," *J. Phys. Chem. C*, vol. 120, no. 40, pp. 23299–23303, 2016.
[196] Z. Guo, Y. Wan, M. Yang, J. Snaider, K. Zhu, and L. Huang, "Long-range hot-carrier transport in hybrid perovskites visualized by ultrafast microscopy," *Science*, vol. 356, no. 6333, pp. 59–62, 2017.
[197] S. Nah, B. Spokoyny, C. Stoumpos, C. M. M. Soe, M. Kanatzidis, and E. Harel, "Spatially segregated free-carrier and exciton populations in individual lead halide perovskite grains," *Nat. Photonics*, vol. 11, no. 5, pp. 285–288, 2017.
[198] C. Y. Wong, B. L. Cotts, H. Wu, and N. S. Ginsberg, "Exciton dynamics reveal aggregates with intermolecular order at hidden interfaces in solution-cast organic semiconducting films," *Nat. Commun.*, vol. 6, p. 5946, 2015.
[199] D. Knig, K. Casalenuovo, Y. Takeda, G. Conibeer, J. F. Guillemoles, R. Patterson, L. M. Huang, and M. A. Green, "Hot carrier solar cells: Principles, materials and design," *Phys. E Low-Dimensional Syst. Nanostructures*, vol. 42, no. 10, pp. 2862–2866, 2010.
[200] S. Park, A. L. Fischer, Z. Li, R. Bassi, K. K. Niyogi, and G. R. Fleming, "Snapshot Transient Absorption Spectroscopy of Carotenoid Radical Cations in High-Light-Acclimating Thylakoid Membranes," *J. Phys. Chem. Lett.*, pp. 5548–5554, 2017.
[201] W. Liu, B. Lee, C. H. Naylor, H. S. Ee, J. Park, A. T. C. Johnson, and R. Agarwal, "Strong Exciton-Plasmon Coupling in MoS2 Coupled with Plasmonic Lattice," *Nano Lett.*, vol. 16, no. 2, pp. 1262–1269, 2016.
[202] T. L. Atallah, J. Wang, M. Bosch, D. Seo, R. A. Burke, O. Moneer, J. Zhu, M. Theibault, L. E. Brus, J. Hone, and X.-Y. Zhu, "Electrostatic Screening of Charged Defects in Monolayer MoS2," *J. Phys. Chem. Lett.*, vol. 8, no. 10, pp. 2148–2152, May 2017.

[203] F. K. Perkins, A. L. Friedman, E. Cobas, P. M. Campbell, G. G. Jernigan, and B. T. Jonker, “Chemical Vapor Sensing with Monolayer MoS2,” *Nano Lett.*, vol. 13, no. 2, pp. 668–673, Feb. 2013.
[204] A. A. Bakulin, C. Silva, and E. Vella, “Ultrafast Spectroscopy with Photocurrent Detection: Watching Excitonic Optoelectronic Systems at Work,” *J. Phys. Chem. Lett.*, vol. 7, no. 2, pp. 250–258, 2016.
[205] E. Dinc, L. Tian, L. M. Roy, R. Roth, U. Goodenough, and R. Croce, “LHCSR1 induces a fast and reversible pH-dependent fluorescence quenching in LHCII in Chlamydomonas reinhardtii cells,” *Proc. Natl. Acad. Sci.*, vol. 113, no. 27, pp. 7673–7678, 2016.
[206] N. Liguori, L. M. Roy, M. Opacic, G. Durand, and R. Croce, “Regulation of Light Harvesting in the Green Alga Chlamydomonas reinhardtii: The C‑Terminus of LHCSR Is the Knob of a Dimmer Switch,” *JACS*, vol. 135, no. 49, pp. 18339–18342, 2013.
[207] G. Bonente, M. Ballottari, T. B. Truong, T. Morosinotto, T. K. Ahn, G. R. Fleming, K. K. Niyogi, and R. Bassi, “Analysis of LHcSR3, a protein essential for feedback de-excitation in the green alga Chlamydomonas reinhardtii,” *PLoS Biol.*, vol. 9, no. 1, p. e1000577, 2011.

Appendix A: MATLAB Code for 2D-ES Signal Processing

```
%This code is used to produce 2D-ES spectra from raw data produced in
% Room 2 in the Fleming Lab at UC Berkeley. It is written in MATLAB.
%Authors: Daniele Monahan and Liang Guo
%Last revised: Fall 2017

%% ------Data input--------
file_path='C:\my_data_folder\'; %path to directory containing data files; remember to
end in '\'
files = dir([file_path 'New Text Document-T=*']); %names of 2D-ES output files

%% ------User Parameters-----
xbd=[1.64,1.98]; ybd=[1.64,1.98]; %bounds for displayed 2D spectrum, eV
tmin=0.94; tmax=1.1; % signal window in t3, picoseconds

%% ---Constants------
h=6.63e-34; %Planck's constant
factor=h*1e15/1.6e-19; %factor for converting frequency 1/fs to photon energy eV
N=2048; %number of points for interpolations
M=N*8;

%% ---Camera/Spectrometer Constants-------
pixel=linspace(0,1339,1340); %CCD pixel index 0-1339
start_pixel=1; end_pixel= 1340;
wavelength=pixel*.2085+553.67; %spectrometer calibration equation for 300 g/mm blaze
750 center 700 nm
f=3e8*1e9/1e15./wavelength(start_pixel:end_pixel); % wavelength to frequency in 1/fs
f=flip(f); %make f increasing
inter_f=linspace(f(1),f(end),N); %evenly interpolated frequency, 1/fs
df=(inter_f(end)-inter_f(1))/(N-1); %frequency step, 1/fs
ts=1/df; %range in the time domain, fs
t=(-ts/2:ts/N:ts/2-ts/N)/1000; %time domain axis, ps
pulse4=dlmread([file_path 'Pulse 4.txt'],'\t')'; %spectrum of pulse 4 taken on CCD
before beginning experiment
pulse4=pulse4(start_pixel:end_pixel);
pulse4=flip(pulse4); %make pulse4 increasing
inter_pulse4=interp1(f,pulse4,inter_f);  %interpolation of pulse 4 spectrum
fringe_phase=exp(1i*inter_f*2*pi*tmin*1000); %phase factor exp(1i*phi43), not needed
if only viewing abs spectra

%% --Main Spectrum Processing Loop-----
file_count=0;
for file_ind=1:length(files)

       file_name = files(file_ind).name
       file_count = file_count+1;
       data=dlmread([file_path file_name ]);

       %% ----Axes------
       if file_count==1 % only need to set axes once, typically
         tau=flip(data(:,1));
         n=length(tau); %number of tau points
         dtau=(tau(end)-tau(1))/(n-1); % tau step size
         fs=1/dtau; %frequency resolution, 1/fs
         M=N*8;
```

```
    fau=-fs/2:fs/M:(fs/2-fs/M); %frequency axis considering zero padding, 1/fs
    n_zero1=round((M-n)/2);
    n_zero2=M-n-n_zero1;
   padding_total1=zeros(n_zero1,N);
   padding_total2=zeros(n_zero2,N);
   probe=factor*inter_f; %probe photon energy
   pump=factor*fau; %pump photon energy
   [head_probe,tail_probe]=index_search(probe,ybd(1),ybd(2)); %define an effective
   range of probe spectrum by two indices. Outside this range, artifact noise
   exists due to dividing by zero in the pulse 4 spectrum.
  [head_pump,tail_pump]=index_search(pump,-xbd(2), -xbd(1));
  v=-flip(pump(head_pump:tail_pump)); %Excitation energy, eV
  u=probe(head_probe:tail_probe); %Emission energy, eV
  end

%% --------2D Spectra--------
spec_het=data(:,1+start_pixel:1+end_pixel);
spec_het=flip(spec_het,2);
spec_het=flip(spec_het,1);
inter_spec_het=inter_by_row(f,spec_het,inter_f); %interpolation of the
heterodyned spectrum at each coherence time

%% --Fourier transform of the interpolated spectrum, windowing and inverse FT--
iFT_spec_het=ifftshift(ifft(inter_spec_het,N,2),2); %inverse FT of the
interpolated spectrum, complex
win_iFT_spec_het=hann_window_by_row(t,iFT_spec_het,tmin,tmax); %windowing in time
domain
E_spec_het=fft(fftshift(win_iFT_spec_het,2),N,2); %windowed interpolated
spectrum, i.e., spectrum of the electric field of the signal
E_spec_fringe=bsxfun(@rdivide,E_spec_het,sqrt(inter_pulse4)); %divide the
heterodyned spectrum at each coherence time by the electric field magnitude of
pulse 4
%  E_spec_fringe=E_spec_het; %uncomment to check effect of LO division
bg=sum(E_spec_fringe(end-10:end,:),1)/10;
E_spec_fringe=bsxfun(@minus,E_spec_fringe,bg); %subtract remaining background

%% --------Phasing-------
E_spec=bsxfun(@times,E_spec_fringe,fringe_phase); %approximate linear phase
% add code here if you have extracted a phase e.g. using the Projection Slice
Theorem
P_spec=bsxfun(@rdivide,E_spec,inter_f*1i); %spectrum of the polarization emitting
the signal, complex

%% -------Separating Rephasing and Nonrephasing--------
% Note: Rephasing is taken by assuming +tau, and should appear at -w1;
Nonrephasing is taken by assuming -tau, is frequency-fliped and should appear at
-.
% Keep commented if you are only viewing the total 2D spectrum
% split=round(n/2); %splitting point for separating rephasing and non-rephasing
% nr_part=P_spec(1:(split+20),:); %rephasing part
% rp_part=P_spec((split-20):end,:); %non-rephasing part
% H=heaviside(tau+200);
% P_spec=bsxfun(@times,P_spec,H);
% win_total=hann(n); % hann window
% P_spec=bsxfun(@times,P_spec,win_total);

%% ------Fourier transform versus tau--------
P_spec=[padding_total1; P_spec; padding_total2];
P_spec=fftshift(P_spec,1);
total_spec=1i*ifftshift(fft(P_spec,M,1),1)/fs; %FT with respect to tau

% Keep commented if you are only viewing the total 2D spectrum
% l_rp=size(rp_part,1); %length for hann window
```

```
        % l_nr=size(nr_part,1); %length for hann window
        % win_rp=hann(l_rp); %hann window
        % win_nr=hann(l_nr); %hann window
        % padding_rp=zeros(n-l_rp,N); %zero padding for rephasing
        % padding_nr=zeros(n-l_nr,N); %zero padding for non-rephasing
        % rp_part=[padding_rp;bsxfun(@times,rp_part,win_rp)]; %apply window and zero
        padding
        % nr_part=[bsxfun(@times,nr_part,win_nr);padding_nr]; %apply window and zero
        padding
        % rp_part=fftshift(rp_part,1);
        % nr_part=fftshift(nr_part,1);
        % rp_spec=1i*ifftshift(fft(rp_part,n,1),1)/fs;
        % nr_spec=1i*ifftshift(fft(nr_part,n,1),1)/fs;

        %% ---Storage------
        total_2D_spec=total_spec(head_pump:tail_pump,head_probe:tail_probe);
        total_amp=flip(abs(total_2D_spec)',2); %amplitude, transposed so that horizontal
        is excitation while vertical is emission

        % rp_2D_spec=rp_spec(head_pump:tail_pump,head_probe:tail_probe);
        % nr_2D_spec=nr_spec(head_pump:tail_pump,head_probe:tail_probe);
        % total_real=real(total_2D_spec)'; %real part
        % total_imag=imag(total_2D_spec)'; %imaginary part
        % % rp_amp=abs(rp_2D_spec)';
        % nr_amp=abs(nr_2D_spec)';
        % rp_real=real(rp_2D_spec)';
        % nr_real=real(nr_2D_spec)';
        % rp_imag=imag(rp_2D_spec)';
        % nr_imag=imag(nr_2D_spec)';

        super_amp(file_ind,:,:)=total_amp; %store in a conveniently saved super array
        wait(file_ind,:)=str2num(file_name(21:end-9))*1000; %waiting time in fs,
        extracted from file names
        [wait,idx]=sort(wait); %sort into increasing waiting time
        super_amp = super_amp(idx,:,:); %corrects for files out of order

end %End of main loop

save('my_save_file', u,v, wait, super_amp) %Always save your work!
```